Investigations of the tunable electronic properties of 2D borocarbonitrides, $(BN)_{1-x}(C)_x$, and of the epitaxial thin films of NiO generated by ALD

A Thesis Submitted for the Degree of

M. S. (Engg.)

By

Rohit Attri

New Chemistry Unit

Jawaharlal Nehru Centre for Advanced Scientific Research

(A Deemed University)

Bangalore-560064 (India)

June 2020

Dedicated to my parents, teachers and for

those who believe nothing is impossible

DECLARATION

I hereby declare that the matter embodied in this M.S. (Engg.) thesis entitled **"Investigations of the tunable electronic properties of 2D borocarbonitrides, $(BN)_{1-x}(C)_x$, and of the epitaxial thin films of NiO generated by ALD"** is the result of investigations carried out by me at the New Chemistry Unit, and the International Centre for Materials Science, Jawaharlal Nehru Centre for Advanced Scientific Research, Bengaluru, India under the supervision of **Prof. C. N. R. Rao, FRS** and that it has not been submitted elsewhere for the award of any degree or diploma.

In keeping with the general practice in reporting scientific investigations, due acknowledgement has been made wherever the work described is based on findings of other investigators. Any omission that might have occurred by oversight or error of judgement is regretted.

Rohit Attri

CERTIFICATE

I hereby declare that the matter embodied in the thesis entitled **"Investigations of the tunable electronic properties of 2D borocarbonitrides, $(BN)_{1-x}(C)_x$, and of the epitaxial thin films of NiO generated by ALD"** has been carried out by Mr. Rohit Attri at the New Chemistry Unit, and the International Centre for Materials Science, Jawaharlal Nehru Centre for Advanced Scientific Research, Bengaluru, India under my guidance and that it has not been submitted elsewhere for the award of any degree or diploma.

Prof. C. N. R. Rao

(Research Supervisor)

ACKNOWLEDGEMENTS

First and foremost, I would like to take this opportunity to express my heartfelt gratitude and profound respect to my research supervisor, ***Prof. C. N. R. Rao, FRS***, for introducing me to thin film deposition techniques and synthesis of two dimensional nanomaterials, and their underlying science. It was his enthusiasm and dedication that instigated in me the desire to pursue science and has continued to inspire me ever since. His innovative ideas and ability to handle any problem in the simplest of the ways has been the strength behind the completion of this work. He has not only been instrumental in shaping up my research, and my career but my entire personality, and my outlook towards life as a whole. With his fathomless patience, unfailing support, critical suggestions, and iron will, nothing has ever a hurdle in this journey. I cannot express words for the respect and care that I have for him.

Special thanks to all my ***scientific collaborators*** because without their help, my work would have been incomplete: Prof. Kanishka Biswas, Dr. Sreedhara M.B., Dr. Subhajit Roychowdhury.

I thank my ***course work instructors***: Prof. Umesh V. Waghmare, Prof. A. Sundaresan, Prof. Bivas Saha, Prof. Sushobhan Avasthi (IISc, Bangalore) for the illuminating courses and discussions.

My sincere thanks to Prof. Subi J. George for his constant support and help in various aspects. Prof. A. Sundaresan for allowing me to do temperature dependent resistance measurements. I would like to thank Mr. Prem Kumar, Mr. Abhijit for helping me in doing various measurements.

Let me take this opportunity to thank my ***beloved labmates***: Dr. S. R. Ligampalli, Dr. K. Gopalakrishnan, Dr. K. Pramoda, Dr. M. B. Sreedhara, Dr. Manjeet Chhetri, Dr. Uttam Gupta, Dr. Anand Roy, Dr. K. Manjunath, Dr. P. Vishnoi, Dr. Manjodh Kaur, Dr. Manoj Jana, Mr. Monis Ayyub, Ms. Manaswee Barua, Mr. Reetendra, Mr. Swaraj, Ms. Aditi Saraswat, Mr. Devesh Binwal, Mr. Rajesh, Mr. Amit, and Mr. Navin. A

special thanks and it has been an enjoyable experience working with all of them.

I thank the timely help of the ***technical staff*** members: Mr. Vasu, Mr. Anil, Mr. V. Srinath, Mr. S. Srinivas (my FESEM guru), Mr. Mahesh, Dr. Jay Ghatak, Mr. Kannan, Mr. Prajwal, Mr. Jagadish and Mr. Shivakumar. I specially thank Mrs. Sudha, Mr. Gowda, Mr. Victor, Mrs. Ramya, and Mrs. Melissa for their help in various aspects. A special thanks to Ms. Meenakshi for helping me with the FESEM instrument.

I extend my sincere thanks to all the staff members associated with ***Administration, Hostel, Academic, Library, Dining hall, Dhanvantari, CPMU***, ***NCU, Security*** and other departments for all their help.

I thank ***JNCASR*** and ***ICMS*** for research fellowship.

I take this opportunity to thank ***Mrs. Indumati Rao and Mr. Sanjay Rao*** for all the affection and love I have received from her. Her notwithstanding age and enthusiasm has been the source of inspiration for me.

A thank all my ***batch mates and friends*** (particularly Mr. Tomar, Mr. Shekhawat, Mr. Kaushik, Mr. Dhar, Mr. Khan, Ms. Bhutani, Ms. Ahuja, Ms. Saini, and Ms. Chanana) with whom I started my life at JNCASR, and whose cheerful company made these three years of life so cherishable.

I would like to thank Dr. Aditya Mahadevan, Mr. Pawan Kumar, Mr. Shashank, Mr. Ashutosh, Mr. Momin, Mr. Vishal Badri, Dr. Shashidhara, Dr. Sanjay, Mr. ShivaRam, Mr. Ravi Shankar, Mr. Aritra Sarkar, Mr. Saptarshi, Mr. Siddharth Singh, Mr. Sinay, Mr. Krishna, Ms. Nikita Gupta, Ms. Ila Joshi, Ms. Suchismita, Ms. Nijita, and Ms. Chaitali for being the part of my academic and non-academic life at JNCASR.

I cannot assemble words to express my gratitude to ***Ms. Surishi Vashishth*** for being there in my happiness and sadness.

Finally, I thank my ***parents***, my younger ***brother Ankush Attri***, ***family members*** and the ***Almighty God*** for everything I have.

PREFACE

Materials exhibit unique properties when one of the dimensions is reduced to atomic scale thickness compared to their bulk counterpart. Deposition of ultrathin films of materials is not only technologically advantageous but also permits exploration of many novel properties. This thesis contains results of investigations carried out on the deposition of thin films (nanosheets) of compositionally tunable 2D borocarbonitrides, $(BN)_{1-x}(C)_x$ and of the nickel oxide thin films (NiO) by atomic layer deposition (ALD). The thesis is divided into two parts, wherein **Part I** deals with tunable electronic properties of 2D borocarbonitrides, $(BN)_{1-x}(C)_x$ and their potential applications. **Part II** deals with atomic layer deposition of ultrathin films of transition metal oxide and its detailed characterization.

Part I is divided into two chapters of which **Chapter I.1** describes the tunable electrical and optical properties of 2D borocarbonitrides, $(BN)_{1-x}(C)_x$ with varying composition, wherein thin films are deposited by pulsed laser deposition (PLD). The study showcases the use of $(BN)_{1-x}(C)_x$ for bandgap tunable opto/nano-electronics and related applications. **Chapter I.2** discusses the low thermal conductivity of 2D borocarbonitride nanosheets of different compositions synthesized by solid state reactions and which can be utilized for thermal management devices in future.

Part II contains one chapter which describes the results of investigations of crystalline epitaxial thin films of NiO deposited by plasma enhanced- atomic layer deposition (PE-ALD). The deposited films have been characterized by various microscopic and spectroscopic tools to provide insight of the growth process.

TABLE OF CONTENTS

Part I

Tunable Electronic Properties of 2D Borocarbonitrides

Chapter I.1

Compositional Tuning of Electrical and Optical Properties of PLD-Generated Thin Films of 2D Borocarbonitrides, $(BN)_{1-x}(C)_x$

Summary*

Borocarbonitrides, $(BN)_{1-x}(C)_x$, provide a means of composition-tuning the bandgaps of BN and graphene. $(BN)_{1-x}(C)_x$ thin films of varied chemical compositions have been deposited on c-sapphire by pulsed laser deposition and characterized by spectroscopic and microscopic techniques. Optical and electrical properties of these films show systematic changes in the band gap and the resistivity with the compositions. Thus, the optical band gap of the films shows a nearly linear dependence on the composition. The study throws light on the semiconducting nature of the $(BN)_{1-x}(C)_x$ thin films with the films exhibiting Efros-Shklovskii (ES) variable range hopping in the low- temperature regime.

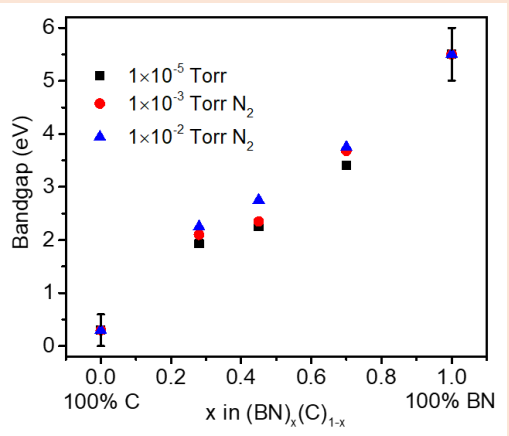

* A paper based on this work is published in ACS Applied Electronic Materials, 2019

1. Introduction

• Borocarbonitrides, $B_xC_yN_z$

Borocarbonitrides with the general formula, $(BN)_{1-x}(C)_x$ (or BCN for simplicity) have emerged as a new class of 2D materials with fascinating properties.[1,2] They can be considered as a network of BN and graphene domains, in addition to having BCN rings in the network.[1,2] *h*-BN is a wide bandgap (~6 eV) insulator whereas graphene is a gapless conductor.[3,4] Borocarbonitrides allow us to vary the bandgap between graphene and BN with the composition or with the carbon content. Since bandgap engineering and tuning of the electronic properties of semiconducting materials has many technological advantages, it appeared desirable to investigate BCN materials for the purpose.[1,2,5,6] Many attempts have been made for bandgap engineering in graphene[7] by induced strain,[8,9] surface bonding, isoelectronic co-doping or chemical doping with nitrogen and other foreign atoms.[10,11] These efforts have led only to a few meV changes in the bandgap.[9] Bridging the optical gap between graphene to BN by chemical means is therefore more appealing. Even though there have been some efforts in this direction, there is a clear need for a systematic study where there is chemical control of the elemental composition.[12]

Samples of BCN synthesized by solid state reaction demonstrate novel properties such as gas adsorption, surface area, and energy storage, among others.[1] Optical properties of BCN have not received much attention due to the carbon present in the samples, making them black in the shade and absorbent of the complete spectrum.[13] What would be ideal is to employ methods to generate large area thin films of BCN with superior optical and electrical properties. Large area films of BCN with homogeneous compositions are still a challenge to obtain.[1] The computational studies

also revealed the composition dependent change in resistivity in BCN.[14] Optical and electrical properties of hybridized boron nitride and graphene domains grown by CVD as a device perspective have been examined by Ci and co-workers.[15] The transport mechanism and the crossover from the insulator to the metal regime in the BCN system in the low-temperature regime has been reported by Ajayan and co-workers.[16,17]

There have been efforts to deposit BCN thin films by sputtering,[18–20] HiPIMS,[20] PECVD,[21,22] LPCVD,[23] APCVD,[24] and pulsed laser deposition (PLD).[25–29] These studies have focused on the film composition or the study of bonding to verify whether the films were products of atomic hybridization.[28,29] The optical properties of BCN with varying composition have not been investigated. Furthermore, wide range tunability of the bandgap and resistivity from graphene to BN of BCN has not been reported. There is no experimental study showing complete tunability of the optical and electrical gap between graphene and BN by varying the composition. In this study, we present the results of a detailed investigation of wide range of compositions of $(BN)_{1-x}(C)_x$ thin films (from graphene end to BN) obtained by PLD, characterized by various spectroscopic and microscopic characterization techniques, along with optical bandgap and electrical resistivity measurements.

- **Pulsed Laser Deposition (PLD)**

Pulsed laser deposition (PLD) is experimentally simple and highly versatile technique to deposit thin films of oxides, sulfides, nitrides and other complex materials as compared to the other deposition techniques.[30] PLD is known for transferring the target stoichiometry into the films. PLD provides excellent control over thickness of the deposited films, sharp interface with the buffer substrate, growth of heterostructures, etc. The deposition rate can be precisely controlled by the number of laser pulses and

can be influenced by other factors such as the target material, laser energy density, repetition rate, substrate temperature, substrate to target distance and background gas. The mechanism of laser – target interaction and the growth of film on substrate involves complex processes but can be understood in simpler manner. A focused laser pulse enters the vacuum chamber to fall on the target. The laser pulse transfers all its energy to the target material via non-thermal processes. The strong absorption of the electromagnetic radiation by the solid surface leads to local heating and rapid ablation/vaporisation of the target material. The ablated material contains ions, energetic electrons, molecules, and neutral atoms which tends to move towards the substrate in the z-direction due to the laws of gas dynamics. The ablated high energy species moves with gradually decreasing velocity, and subsequently impinge on the heated substrate. These active species suffer backscattering from the substrate surface and collide with the incoming flux, and a collision region is established. The film grows immediately after this collision region is formed. The region serves as a source for condensation of particles. When the condensation rate is higher than the rate of particles

Scheme 1: Schematic illustration of thin film deposition using PLD.

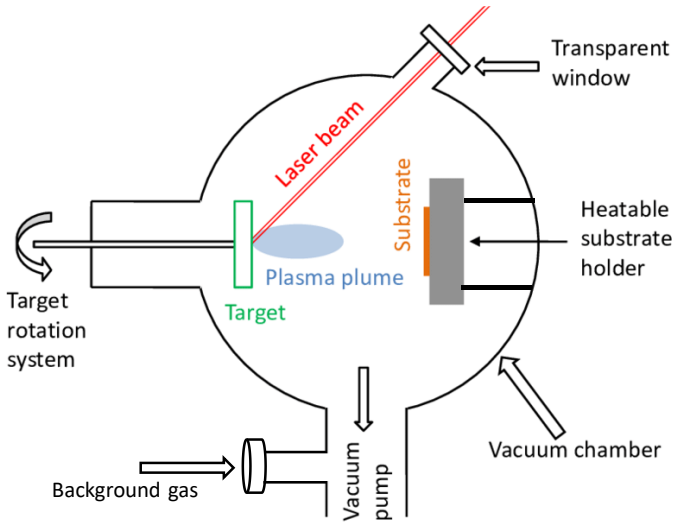

suffering backscattering, the thermal equilibrium condition can be reached quickly. The film grows on the substrate surface at the expense of the direct flow of the ablated species. The final step is the nucleation and the growth of film. There are some growth models discussed in the literature based on the growth kinetics.[31] The nucleation process depends on the interfacial energy between the three phases present – the substrate, the vapor phase, and the condensing material. The deposition rate and the substrate temperature play a critical role in the film formation. Depending upon the nature of the substrate and the provided temperature, the films can be amorphous, polycrystalline or single crystalline. Despite its simplicity, there are some shortcomings in PLD technique. The major problems are the particulates deposition, and the narrow angular distribution of the plume. The particulates formation is generally observed in PLD deposited thin films because of the incomplete conversion of solid target into active plasma species. These particulates can be of micrometer size and can affect the characteristics of the film, however a velocity filter can be used to cut-off heavy and slow moving particulates while transmitting the high energetic plume.[32] Due to the narrow angular distribution large area uniform film growth is a problem, but suitable measures can be taken for large area growth such as rotating both the target and the substrate, and raster scanning of the target will give a uniform film.[33]

2. Scope of the present investigations

Borocarbonitrides are the class of 2D layered materials which possess many novel properties.[1,34] Not only are they semiconducting, but also the band gap can be tuned from gapless graphene to insulating boron nitride. Nanometer thick films of materials are important for various device aspects. The ability to tune the electronic structure of BCN by varying the compositions can be used for various potential applications.[17] It

would be interesting to grown large area thin films of BCN with superior electrical and optical properties. Opting PLD to deposit thin films of BCN ensures the atomic hybridization of B-C-N atoms in the films. Till now researchers have employed BN, graphite, boron carbide (B_4C) targets in the N_2 atmosphere for the deposition of BCN films. We have used spark plasma sintered $B_xC_yN_z$ (or BCN for simplicity) targets synthesized by the solid state reaction of exfoliated graphene (EG) or activated charcoal with boric acid, and urea to deposit the thin films BCN. A detailed study of the film surface morphology and chemical bonding as well as the optical and the electrical properties of PLD deposited BCN films would have potential uses in optoelectronics, FET's, and photoelectrochemistry.

3. Experimental Section

Materials

All the chemicals which were used are of high purity and were used as received without any further purification. Natural graphite powder (Alfa Aesar, 99.99%), sulphuric acid (SDFCL, 98%), potassium permanganate (Merck), sodium nitrate (SDFCL), hydrogen peroxide (Merck), activated charcoal (SDFCL) , boric acid (Merck), urea (SDFCL), deionised water, graphite Dye (Mersen India, 2114-Grade).

Synthesis

Synthesis of graphene oxide (GO) and exfoliated graphene (EG)

Graphene oxide was synthesized by the modified Hummer's method.[35] In a typical synthesis process, 150 mL of concentrated sulphuric acid was added dropwise to a 2 L beaker, containing 3 g of natural graphite powder and sodium nitrate ($NaNO_3$) each, kept in an ice bath. The mixture was allowed to stir for 15 minutes and then 20 g of potassium permanganate ($KMnO_4$) was added to the mixture, while the beaker was still

in an ice bath. The beaker was then transferred to an oil bath maintained at 40 °C and stirred for an hour. To the resulting suspension, 150 mL of water was slowly added and the suspension was further stirred at 75 °C for approx. 15 minutes. Finally, 30 mL of H_2O_2 in 300 mL of deionized water was added to the reaction mixture and allowed to settle down for 24 hours. The brown coloured suspension obtained was washed several times with water until the pH of the solution became neutral. The suspension was then lyophilized to obtain fluffy brown coloured solid GO. Exfoliated graphene (EG) was then obtained by thermal exfoliation of GO at 900 °C under N_2 (UHP, 99.99%) atmosphere.[36]

Preparation of PLD Targets of $(BN)_{1-x}(C)_x$

BCN powder samples of various compositions were prepared using exfoliated graphene (EG) or activated charcoal by the solid state reaction with boric acid and urea in an inert atmosphere at 900 °C.[34] Two sets of three different compositions of $(BN)_{1-x}(C)_x$ were prepared starting from graphene or activated charcoal while keeping boric acid to urea ratio (1:10) constant.[37] In order to obtain sintered dense pellets of these compositions for the PLD targets, the samples were hot pressed in a Spark Plasma Sintering (SPS, Dr. Sinter Lab Jr. Series) instrument with 3.5 kN/cm^2 pressure at 550 °C for 5 min. The targets were then analyzed for their composition by TGA and XPS.

Thin Film Deposition

The prepared targets were mounted on a rotating target holder in the PLD chamber (STD-12 PLD system, Excel Instruments), and a plano-convex lens with focal length of 300 mm was used to focus the laser beam. BCN films from each target were deposited using a KrF (Complex Pro, Lambda Physik) excimer laser with a wavelength of 248 nm maintained at 20 ns pulse width. The laser repetition rate and the energy per

pulse were maintained at 5 Hz and 200 mJ, respectively, for all the deposition. The substrates were cleaned by ultrasonication in acetone and isopropanol for 10 min, then washed several times with DI water, and dried with N_2. The cleaned substrates were placed on a heater with a temperature controller, which is front facing and kept 50 mm away from the target. All the BCN films were deposited on *c*-sapphire at 800 °C at three different working pressures (1×10^{-5} Torr, 1×10^{-3} Torr in N_2 and 1×10^{-2} Torr in N_2) and were subsequently annealed for 2 h. The films with target compositions of $(BN)_{0.45}(C)_{0.55}$ and $(BN)_{0.70}(C)_{0.30}$ were deposited for 5000 laser shots, whereas $(BN)_{0.28}(C)_{0.72}$ was deposited with 1000 laser shots (carbon - rich targets give very higher thickness with 5000 shots). An ultrathin film with $(BN)_{0.45}(C)_{0.55}$ was also deposited on sapphire for 120 laser shots at 1×10^{-5} Torr. Thin films from the targets of BCN synthesized using activated charcoal were also deposited with same deposition parameters.

Characterization

Gravimetric compositions of the BCN targets were determined by thermogravimetric analyses, carried out in an oxygen atmosphere with a Mettler Toledo TGA-850 TG analyzer. X-ray diffraction patterns were collected using a Bruker D8 Discover diffractometer using Cu-Kα radiation with an accelerating voltage of 40 kV and a current of 30 mA. Raman spectra were collected at different spots on uniformly coated $(BN)_{1-x}(C)_x$ films in the backscattering geometry using a 515 nm green laser with a Jobin Yvon LabRam HR 800 spectrometer. Surface morphology and film thickness were determined using a Nova NanoSEM 600 FESEM (FEI). Chemical compositions and the nature of bonding were examined by X-ray photoelectron spectroscopy (XPS) using an Omicron nanotechnology spectrometer with an Al-Kα as a monochromatic X-

ray source (E=1486.7 eV). Before XPS measurement, the film surface is sputtered with Ar^+ ions to remove the surface contaminants. Atomic force microscope (AFM) topographic images were obtained using Bruker Innova instrument in tapping mode. Transmission electron microscopy (TEM) samples were prepared by "lift-off" method using focused ion beam (FIB) in FEI Quanta 3D dual beam SEM/FIB system. TEM images were acquired from a FEI Tecnai G^2 S-Twin operated microscope at an accelerating voltage of 200 kV, fitted with a Gatan CCD camera. High-resolution TEM images and electron energy loss spectra (EELS) were recorded using Titan (cube) FEI aberration-corrected transmission electron microscope with an accelerating voltage of 300 kV. Temperature dependent resistance measurements were carried out in Physical Property Measurement System (PPMS, Quantum Design, USA) in electrical transport option (ETO) mode by four - probe method. The optical properties were studied using Perkin Elmer Lambda 750 UV-Vis spectrometer in transmission mode. Photographs of the films were taken by a DSLR camera under normal daylight.

Calculation of chemical composition from the XPS signal

The signals obtained from the XPS were analysed by Fityk 1.3.1 software. For reference purpose, C 1s peak position was taken at 284.6 eV. The Shirley background was first subtracted from the raw spectra and then the spectra were fitted into multiple peaks using Voigt function (Lorentzian + Gaussian). The relative atomic percentages of elements were calculated from the integrated area under the B (1s), C (1s), and N (1s) signals and the Atomic Sensitivity Factor (A.S.F) of boron (0.088), carbon (0.205) and nitrogen (0.38) by using the following equation:

$$\%\ of\ element = \frac{Area\ under\ curve/A.S.F\ of\ element}{\sum_{all\ elements} Area\ under\ curve/A.S.F\ of\ element}$$

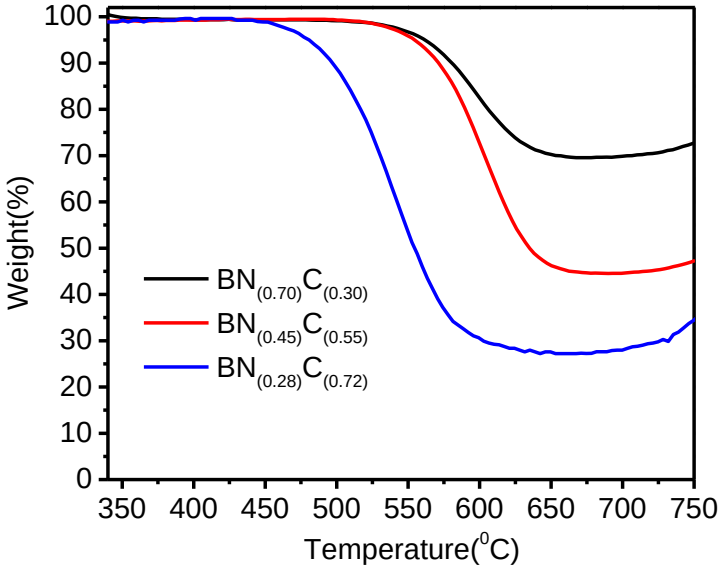

Figure 1. Thermogravimetric analysis of various compositions of BCN prepared from graphene.

4. Results and Discussion

PLD targets of borocarbonitrides, $(BN)_{1-x}(C)_x$, with three different chemical compositions prepared independently by solid state reactions, were pressed into pellets by the SPS method. Thermogravimetric analysis (**Figure 1)** in an oxygen atmosphere of as synthesized samples revealed the compositions of the samples to be $(BN)_{0.70}(C)_{0.30}$, $(BN)_{0.45}(C)_{0.55}$ and $(BN)_{0.28}(C)_{0.72}$, and the BCN starting with activated charcoal also has similar compositions of $(BN)_{0.76}(C)_{0.24}$, $(BN)_{0.55}(C)_{0.45}$, and $(BN)_{0.15}(C)_{0.85}$, respectively. The molar ratio of the precursors along with the thermogravimetric compositions are given in **Table 1**. The thermal stability of the BCN samples improved substantially compared to that of graphene, which is consistent with earlier reports.[34] The BN rich $(BN)_{1-x}(C)_x$ show more stability as compare to the carbon rich. As prepared targets are black in colour because of complete absorption by carbon,

Table 1. Gravimetric Compositions of BCN targets prepared using EG with molar ratios of the precursors used for the synthesis obtained from TGA*

Boric acid (mg)	Urea (g)	EG (mg)	Gravimetric Composition
16.5	0.165	150	$(BN)_{0.28}(C)_{0.72}$
150	1.5	150	$(BN)_{0.45}(C)_{0.55}$
450	4.5	150	$(BN)_{0.70}(C)_{0.30}$

* BCN compositions $(BN)_{0.15}(C)_{0.85}$, $(BN)_{0.55}(C)_{0.45}$, and $(BN)_{0.76}(C)_{0.24}$ were obtained starting with activated charcoal.

irrespective of the compositions. The BCN system has been extensively characterized by various spectroscopic and microscopic characterization techniques in our earlier studies.[12,34,38] These targets were further used to deposit the BCN films to probe their electrical and optical properties. The characteristic properties of the films were studied as a function of change in target composition, and with change in partial pressure during deposition. Various measurements showed that the two sets of BCN obtained from different carbon sources were similar.

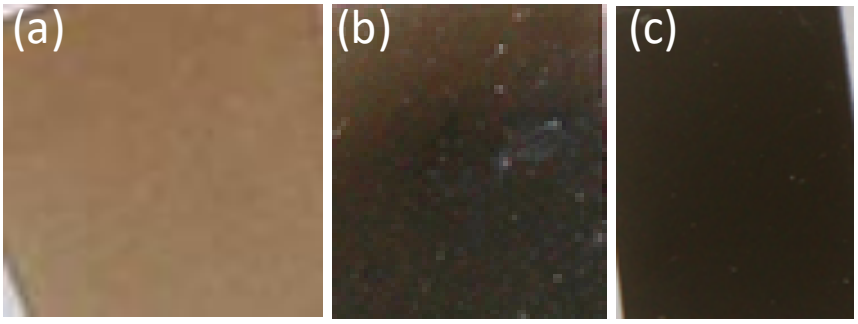

Figure 2. (a-c) Photographs of BCN films obtained from the target composition (a) $(BN)_{0.70}(C)_{0.30}$, (b) $(BN)_{0.45}(C)_{0.55}$, (c) $(BN)_{0.28}(C)_{0.72}$ prepared using EG.

Characteristics of BCN Thin Films

Figure 2 show the photographs of BCN films showing large area uniformity and display varying colour with composition unlike in the powder samples. The BN rich films are light brown in colour, whereas graphene rich films are dark, which indicates the different optical absorption edges. X-ray diffraction patterns of BCN films on c-sapphire showed no significant diffraction peaks indicating the amorphous nature, whereas PLD targets show the (00l) reflection of layered BCN materials.

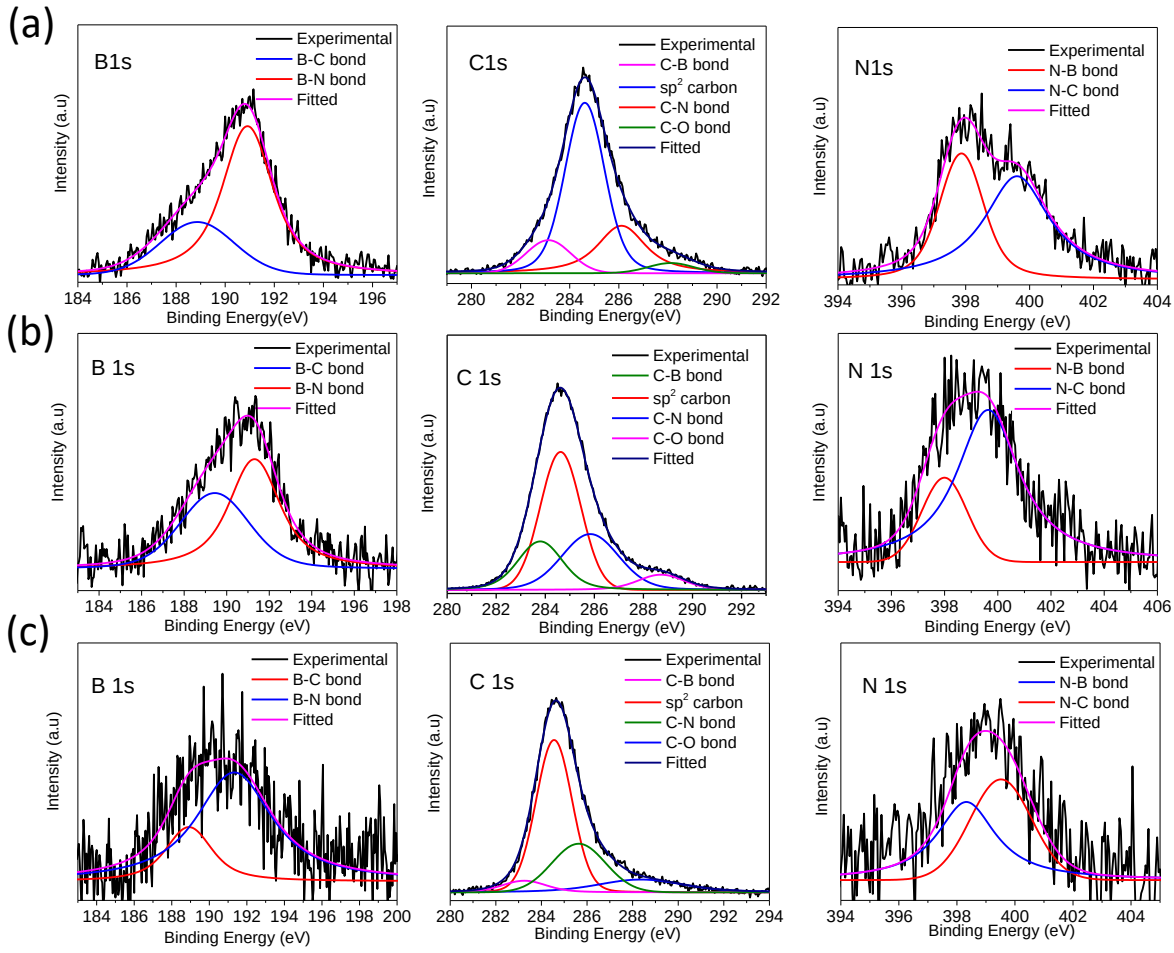

Figure 3. Core level XP Spectra of B 1s, C 1s and N 1s of BCN films obtained at 1×10^{-5} Torr from target composition (a) $(BN)_{0.70}(C)_{0.30}$, (b) $(BN)_{0.45}(C)_{0.55}$ and (c) $(BN)_{0.28}(C)_{0.72}$ prepared from EG.

In order to examine the chemical composition and bonding in the various compositions of BCN, X-ray photoelectron spectroscopy measurements were carried out on the samples deposited on c-sapphire. XP spectra show the presence of boron, carbon, nitrogen, and oxygen in the film. **Figure 3** shows core-level XP spectra of 1s binding energy of each element B, C, and N of the BCN films obtained from three different target compositions at 1×10^{-5} Torr. The high-resolution B 1s spectra of $(BN)_{0.70}(C)_{0.30}$ could be deconvoluted into two peaks: the major peak centered at 190.9 eV corresponds to B-N bonds and the shoulder at 188.85 eV arising from B-C bonds.[1,34] Since there is no evidence for the presence of B-O bonds from other spectroscopic data, so there is no significant feature expected for this in the XP spectrum also.[1] The film deposited from $(BN)_{0.45}(C)_{0.55}$ show B-C and B-N signals occur at 189.45 and 191.3 eV, whereas $(BN)_{0.28}(C)_{0.72}$ exhibit at 188.9 and 191.3 eV, respectively. High-resolution C 1s spectra could be deconvoluted into four peaks: the major peak centered at 284.6 eV corresponding to the planar sp^2 bonded C=C bond, and a long tail towards high B.E. with two peaks at 286.1 and 288.1 eV corresponding to C-N and C-O, respectively. The small shoulder at 283.1 eV is attributed to C-B bonds. The position of major peak due

Table 2: The area of different bonds present in BCN films deposited at 1×10^{-5} Torr from targets prepared using EG is shown by XPS.

	B1s		**C1s**			**N1s**	
Composition	**B-C**	**B-N**	**C-B**	**C-C**	**C-N**	**N-B**	**N-C**
$(BN)_{0.70}(C)_{0.30}$	**290**	**728**	**364**	**1833**	**770**	**460**	**712**
$(BN)_{0.45}(C)_{0.55}$	**358**	**515**	**1698**	**3930**	**2361**	**390**	**1070**
$(BN)_{0.28}(C)_{0.72}$	**230**	**828**	**192**	**1860**	**860**	**436**	**396**

Table 3. BCN films compositions obtained from XPS deposited with targets prepared using EG and charcoal, at 1×10^{-5} Torr.

Composition of BCN films starting with EG	Composition of BCN films starting with activated charcoal
$B_{0.26}C_{0.68}N_{0.06}$	$B_{0.18}C_{0.74}N_{0.08}$
$B_{0.18}C_{0.75}N_{0.07}$	$B_{0.25}C_{0.62}N_{0.13}$
$B_{0.38}C_{0.51}N_{0.11}$	$B_{0.44}C_{0.43}N_{0.12}$

to sp^2 bonded C remains the same at 284.6 eV irrespective of change in carbon content in the films. The area under the C-N signal is higher than that under the C-B signal, showing that C-N bonds are more favoured **(Table 2)**. The C-O bonding arises from the oxygen containing functional groups attached to the graphene surface which was evidently shown in our previous work.[37] The N 1s spectrum of the films obtained from different compositions were fitted into two peaks at 397.8 and 399.6 eV corresponding to N-B and N-C bonds, respectively. There is a slight shift in the peak positions due to change in the chemical compositions. The spectral features exhibited by all the XP spectra suggest the presence of random network of BCN along with the domains of graphene and BN. The elemental composition of BCN films deposited from $(BN)_{0.45}(C)_{0.55}$ at 1×10^{-5} Torr is found to be $B_{0.18}C_{0.75}N_{0.07}$, and the elemental composition of the all BCN films deposited at 1×10^{-5} Torr obtained from XPS data is tabulated in **Table 3**. Carbon concentration in the films increases in comparison to that in the host targets, which might be due to the loss of the energetic species of B and N during the deposition.[39] The films deposited by the targets prepared using activated charcoal exhibit similar XP spectral features.

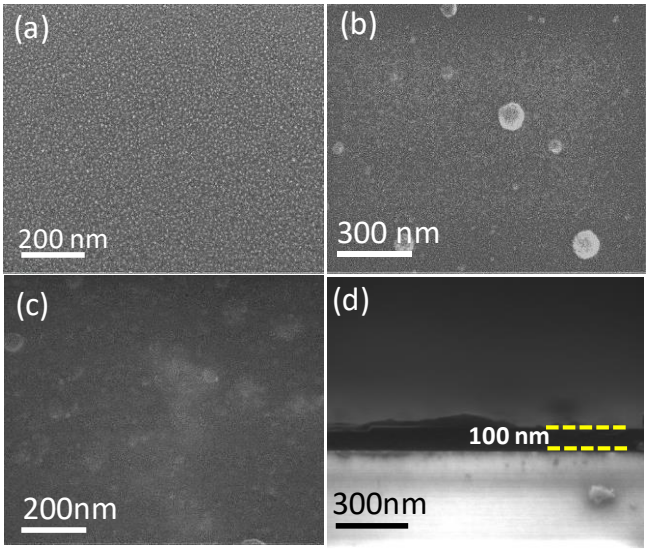

Figure 4. FESEM image of BCN films obtained from target composition (a) $(BN)_{0.28}(C)_{0.72}$, (b) $(BN)_{0.45}(C)_{0.55}$ and (c) $(BN)_{0.70}(C)_{0.30}$ prepared using EG (d) cross-section image of BCN film obtained from target composition $(BN)_{0.45}(C)_{0.55}$.

The Surface topography of the films was studied by FESEM and AFM measurements. **Figure 4(a-c)** shows top-view FESEM images of BCN films obtained from different target compositions at 1×10^{-5} Torr. The films are uniform, and there are significant number of spherical particulates observed on the surface, which are common in the PLD grown films because of the formation of liquid droplets results from the laser ablation.[30] The size of the spherical particulates decreases from BN rich films to carbon rich films; this might be due to the boron and nitrogen species getting converted more into liquid droplets than carbon species. We have not seen any effect on the surface morphology of the films with change in growth pressure except for the size of spherical particulates decreasing due to reduced mean free path with the background pressure (**Figure 5(a-c)**). Cross-sectional FESEM images show the thickness of films to be ~100 nm for the films obtained using $(BN)_{0.45}(C)_{0.55}$ and $(BN)_{0.70}(C)_{0.30}$ targets with 5000 laser shots at 1×10^{-5} Torr (**Figure 4(d)**). The film deposited using the carbon rich target $(BN)_{0.28}(C)_{0.72}$ with 1000 pulsed laser shots at 1×10^{-5} Torr shows the

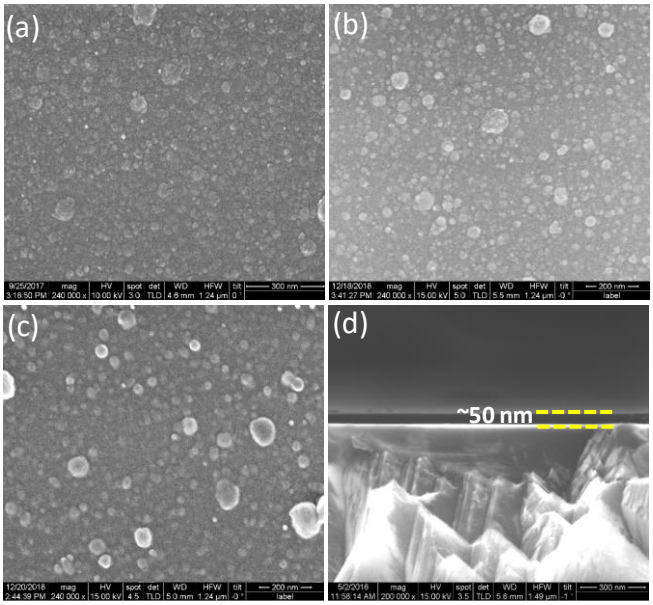

Figure 5. FESEM image of BCN films obtained from $(BN)_{0.55}(C)_{0.45}$ prepared from activated charcoal at (a) 1×10^{-2} Torr in N_2 (b) 1×10^{-3} Torr in N_2 (c) 1×10^{-5} Torr (d) cross-section image of BCN film obtained from $(BN)_{0.28}(C)_{0.72}$ prepared from EG.

thickness to be around ~ 50 nm (**Figure 5(d)**). The thickness of the $(BN)_{1-x}(C)_x$ films varies slightly with change in the background pressure due to reduced mean free path of the particles. The thickness of the film deposited from $(BN)_{0.70}(C)_{0.30}$ was also examined by cross-sectional TEM, which was consistent with the cross-sectional FESEM results. AFM images show the similar surface topographies of the BCN films deposited from target prepared using EG (**Figure 6(a-c)**) and activated charcoal (**Figure 6(d-f)**); the particulates deposited on the films can be clearly seen. The size of the particulates decreases with an increase in carbon concentration, and the RMS roughness of the films varies from 5.58 to 2.27 nm.

HRTEM and Electron Energy Loss Spectroscopy (EELS) were employed to analyse the microstructure and local chemical composition of the film. The HRTEM images show the sharp interface between BCN film and the c-Al_2O_3 substrate. We did

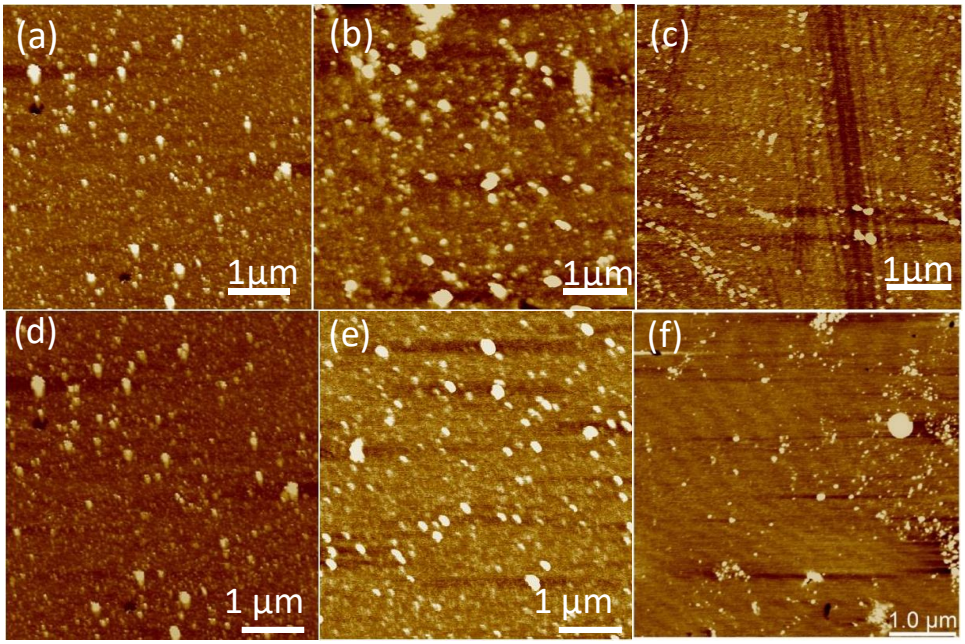

Figure 6. (a-c) Tapping mode AFM images of BCN films obtained at 1×10^{-5} Torr from target composition (a) $(BN)_{0.70}(C)_{0.30}$, (b) $(BN)_{0.45}(C)_{0.55}$, (c) $(BN)_{0.28}(C)_{0.72}$ prepared using EG. (d-f) BCN films obtained at 1×10^{-5} Torr from target composition (d) $(BN)_{0.76}(C)_{0.24}$, (e) $(BN)_{0.55}(C)_{0.45}$, (f) $(BN)_{0.15}(C)_{0.85}$ prepared using charcoal.

not see any crystalline domains of BN and graphene in HRTEM due to the amorphous nature of the film (**Figure 7**). The EEL spectrum of the BCN films in (**Figure 7(e-g)**) shows the K-shell ionization edges of the B, C and N elements, individually. The peaks at 191.6 and 201 eV in the B 1s EEL spectra appears because of the transition of the 1s electron to π* and to σ* antibonding orbitals. The K-shell ionization edges of carbon at 285.6 and 296.8 eV correspond to 1s→ π* and 1s→ σ* transitions.[40] Similarly, peaks at 401.1 and 408 eV correspond to the 1s→ π* and 1s→ σ* transitions of N 1s.[41] The splitting of π* and σ* levels in B 1s, C 1s and N 1s spectra indicates sp^2 hybridization similar to that of graphene and BN.

Raman spectra of the BCN films deposited from various target compositions show the characteristic D and G band at 1590 cm^{-1} and 1360 cm^{-1} (**Figure 8**) corresponding to graphene and BN domains in BCN, respectively.[12] The intensity of

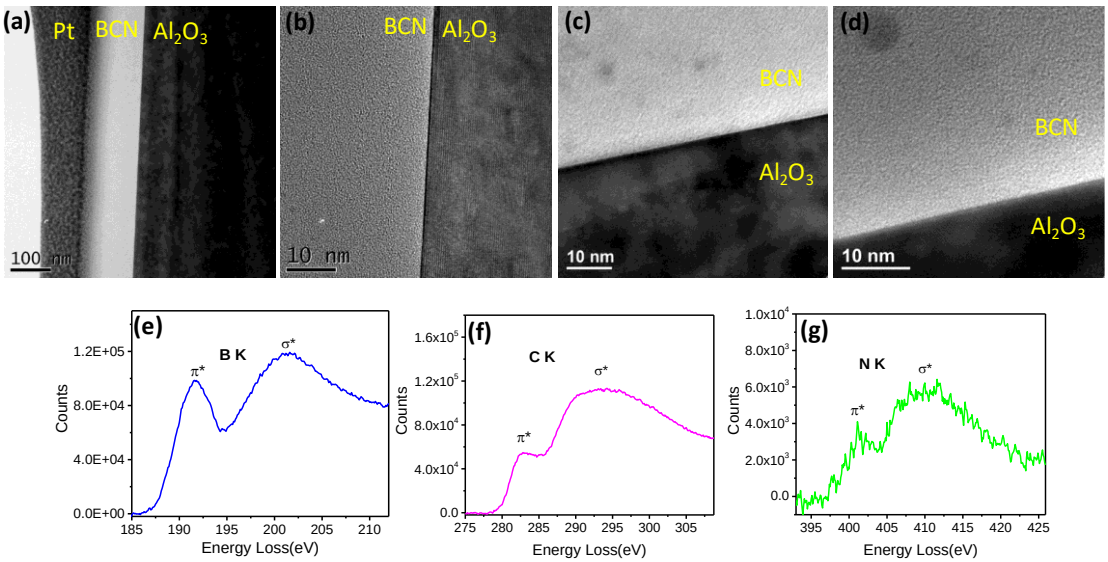

Figure 7. (a) high resolution cross-section image (b-d) HRTEM images and (e-g) corresponding EEL Spectra of each element B, C and N respectively; of BCN film deposited with target composition $(BN)_{0.70}(C)_{0.30}$ prepared using EG, at 1×10^{-5} Torr.

the D band has a contribution from defects and the BN stretching mode. **Figure 8** clearly shows that as the BN content increases, the D band becomes more intense.[42] The change in the relative intensities of the D and G bands (I_D/I_G ratio) is shown in **Table 4**. The D band can be deconvoluted into two peaks with the one at higher energy corresponding to the B-N stretching mode,[43] and the other at lower energy corresponding to the A_{1g} mode resulting from the double resonance phonon scattering.[44]

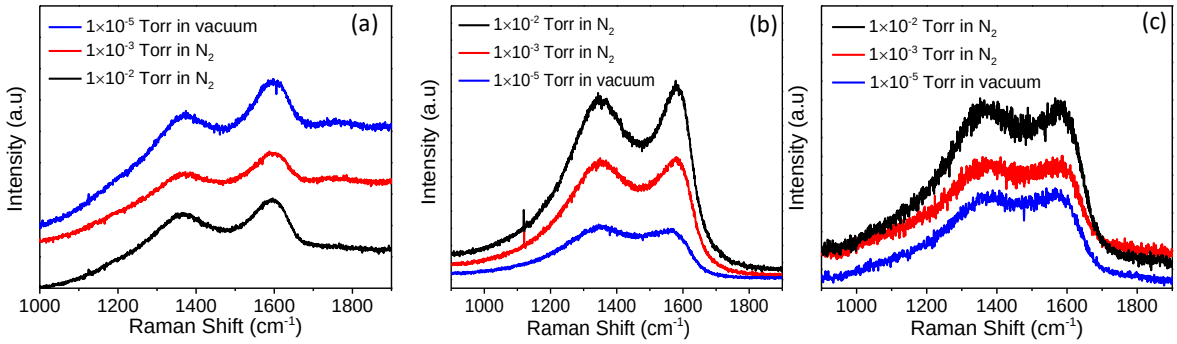

Figure 8. Raman Spectra of BCN films deposited at different partial pressure with target composition (a) $(BN)_{0.70}(C)_{0.30}$ (b) $(BN)_{0.45}(C)_{0.55}$ (c) $(BN)_{0.28}(C)_{0.72}$.

Table 4: I_D/I_G ratio calculated from the Raman Spectra of BCN films deposited with targets prepared using EG

Deposition Pressure (in Torr)	I_D/I_G ratio of BCN films with Target Composition		
	$(BN)_{0.28}(C)_{0.72}$	$(BN)_{0.45}(C)_{0.55}$	$(BN)_{0.70}(C)_{0.30}$
1×10^{-5} in vacuum	0.536	0.522	0.465
1×10^{-3} in N_2	0.565	0.536	0.528
1×10^{-2} in N_2	0.626	0.547	0.639

Optical Properties of BCN Films

Optical properties of BCN thin films are interesting, as one can tune the bandgap by varying the composition. Optical spectra of the films were recorded in transmittance mode in a UV-vis spectrometer, and the absorption coefficient 'α' was calculated using the film thickness 'd' and transmittance 'T' by the following formula:

$$\alpha = \frac{log(^{100}/_{T})}{d} \qquad (1)$$

We have estimated the optical bandgap of the BCN films by the direct bandgap model of J. Tauc,[45] by plotting the square of absorption coefficient as a function of incident photon energy. The optical bandgap was calculated by extrapolating a straight line using the following equation:

$$(\alpha h\nu)^2 = (h\nu - E_g) \qquad (2)$$

Here, 'E_g' is the optical bandgap, and '$h\nu$' is the photon energy in eV. **Figure 9(a-c)** shows Tauc plots of BCN films obtained from the different target compositions

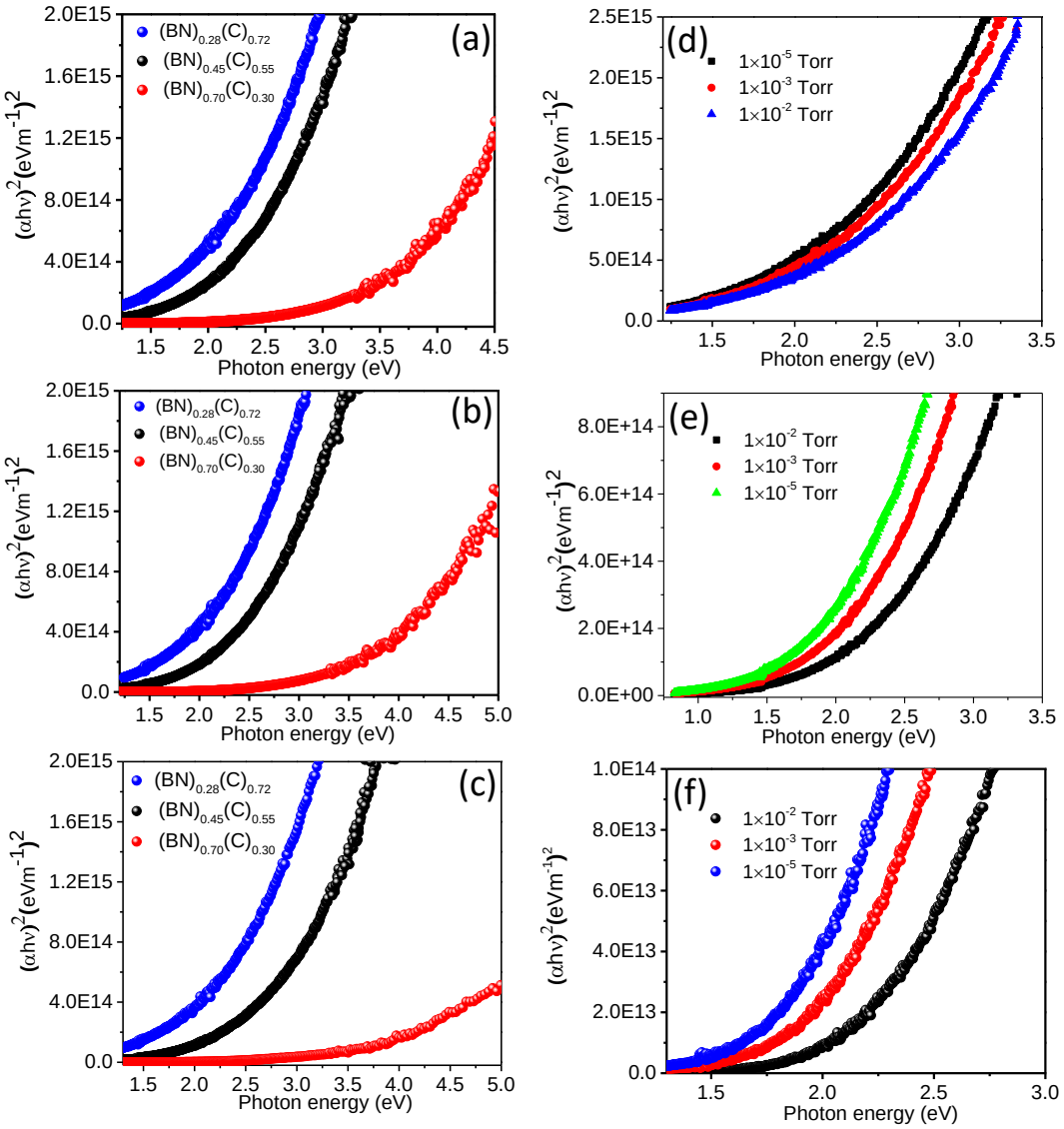

Figure 9. (a-c) Tauc plot of BCN films deposited with targets of three different compositions prepared using EG at (a) 1×10^{-5} Torr, (b) 1×10^{-3} Torr, and (c) 1×10^{-2} Torr in N_2, (d-f) Tauc plot of BCN films deposited at different partial pressure using target composition (d) $(BN)_{0.28}(C)_{0.72}$ (e) $(BN)_{0.45}(C)_{0.55}$ (f) $(BN)_{0.70}(C)_{0.30}$ prepared using EG.

deposited at 1×10^{-5} Torr, 1×10^{-3} Torr, and 1×10^{-2} Torr N_2, as the BN content in the film increases, the band gap also increases and vice versa as expected. Films obtained with same target composition under different partial pressure also show the minor changes (±0.2 eV) in the band gap values (**Figure 9(d-f)**). Thus, the bandgap of the film deposited from $(BN)_{0.45}(C)_{0.55}$ is observed to be 2.25 to 2.75 eV from low to high

pressure. We observed two optical absorption edges in ultrathin films deposited from $(BN)_{0.45}(C)_{0.55}$ at 1.5 and 3.1 eV, in conformity with an earlier report[15] (**Figure 10(a)**). The observation of the two bands in the ultrathin films of BCN indicates the presence of more than one kind of domain, whereas in the case of thicker films, all the domains optically overlap to give the average absorption edge. The π states of sp^2 carbon are more dominant in the optical band; hence, decreases the optical band gap with increases in C content are observed.[46,47] The π states of the sp^2 carbon are more weakly bonded than the σ states and lie closer to the Fermi level.[26] With decreasing carbon concentration in the BCN films, the π states from sp^2 carbon decreased, which resulted in the increase of the optical band gap. **Figure 10(b)** shows optical bandgap of $(BN)_{1-x}(C)_x$ thin films as a function of composition or carbon content at different growth pressures. The plot illustrates the roughly linear relationship with the composition. The calculated optical bandgap of the films deposited at 1×10^{-5} Torr varies from 1.93 to 3.41 eV as the composition goes from $(BN)_{0.28}(C)_{0.72}$ to $(BN)_{0.70}(C)_{0.30}$. The BCN films

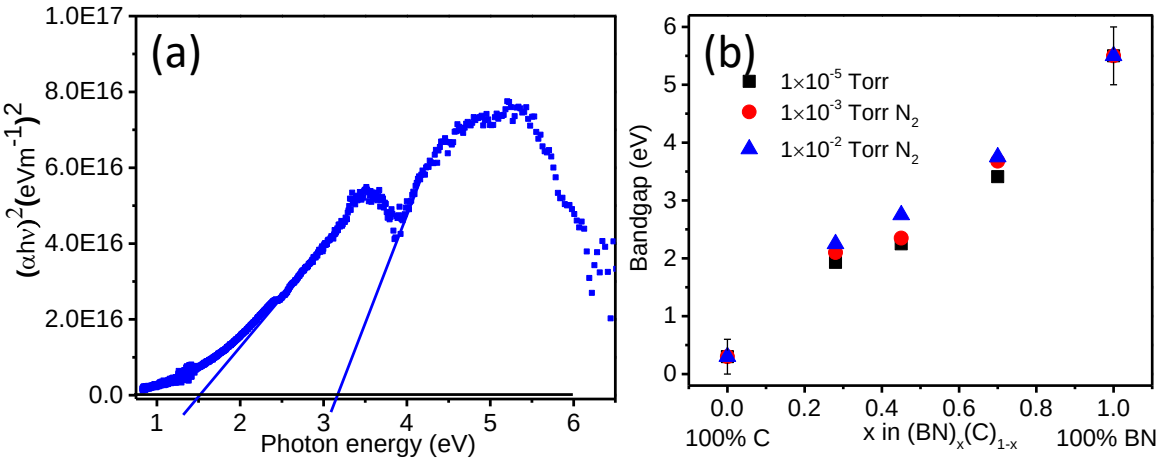

Figure 10. (a) Tauc plot of the ultrathin film of (~5nm) BCN deposited from $(BN)_{0.45}(C)_{0.55}$ prepared using EG at 1×10^{-5} Torr. (b) Optical bandgap versus BCN composition at different background pressure (the error bar for carbon and BN films is considered from the literature reports).

obtained from the targets prepared using activated carbon show similar optical properties.

Electrical Transport Properties of BCN Films

Figure 11 shows the temperature dependence of the electrical resistivity of BCN films obtained from two distinct target compositions $(BN)_{0.45}(C)_{0.55}$ and $(BN)_{0.28}(C)_{0.72}$, as a function of working pressures. The temperature dependent resistivity curve exhibits semiconducting nature of the $(BN)_{1-x}(C)_x$ films and shows that the films are purely originated from hybridized BN and graphene domains. We have observed a considerable increase in resistivity in each BCN film as we change the deposition pressure from low to high. The electrical resistance of the BCN films of $(BN)_{0.70}(C)_{0.30}$ exhibits high electrical resistance (1.6×10^{8} ohms) at room temperature due to high insulating BN content which is beyond the measuring limit of our instrument. We used the following equation for the conversion of sheet resistance to resistivity.[48]

$$\rho = \frac{\pi}{Ln\,(2)} \times t \times Rs \qquad (3)$$

where 'ρ' is the electrical resistivity, 't' is the thickness of the sample and 'Rs' is the sheet resistance. The resistivity curve in **Figure 11** displays a 2 to 3 order change in the resistance of the films with the working pressure. The resistivity of the films obtained from the target composition $(BN)_{0.45}(C)_{0.55}$ increases from 7.4×10^{-4} to 0.10 ohm·m as the base pressure changes from 1×10^{-5} to 1×10^{-2} Torr at room temperature. Similarly, the film obtained from the target composition of $(BN)_{0.28}(C)_{0.72}$ shows a change from 1.4×10^{-4} to 0.001 ohm·m. The change in resistivity with the working pressure is mainly because of the change in the surface chemical composition of the films as seen in the XPS. We have also observed the change in electrical resistivity of the films obtained

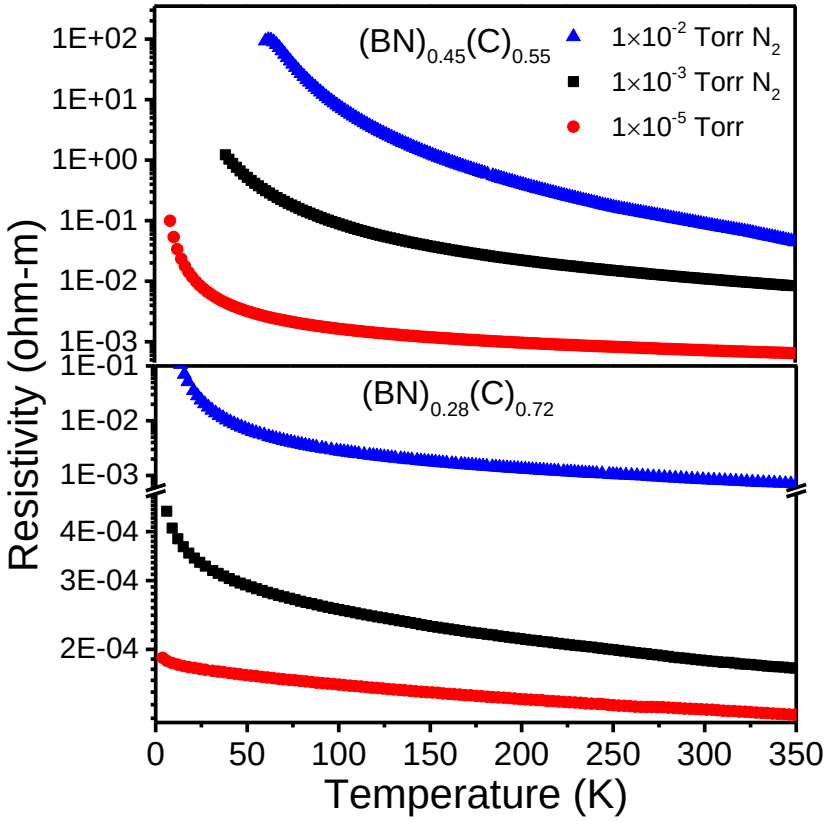

Figure 11. Temperature dependent resistivity results of BCN films deposited at three working pressures with target compositions of $(BN)_{0.45}(C)_{0.55}$ and $(BN)_{0.28}(C)_{0.72}$ prepared using EG.

from $(BN)_{0.28}(C)_{0.72}$ and $(BN)_{0.45}(C)_{0.55}$ target compositions at the same working pressure (**Figure 12**). There is a large change in resistivity with the target composition at the same working pressure, and it is clear that the change in composition plays the expected role. With these results, one can tune the working pressure and composition of targets to get films with the desired electrical properties for specific applications.

Electronic transport properties of BCN are akin to those of disordered semiconductors, where electron localization and hopping conduction near the Fermi level play a significant role. Moreover, a clear understanding of the electrical transport properties in BCN like composites is lacking. For a better understanding of the hopping mechanism in this system, one should know the difference between Mott-VRH and

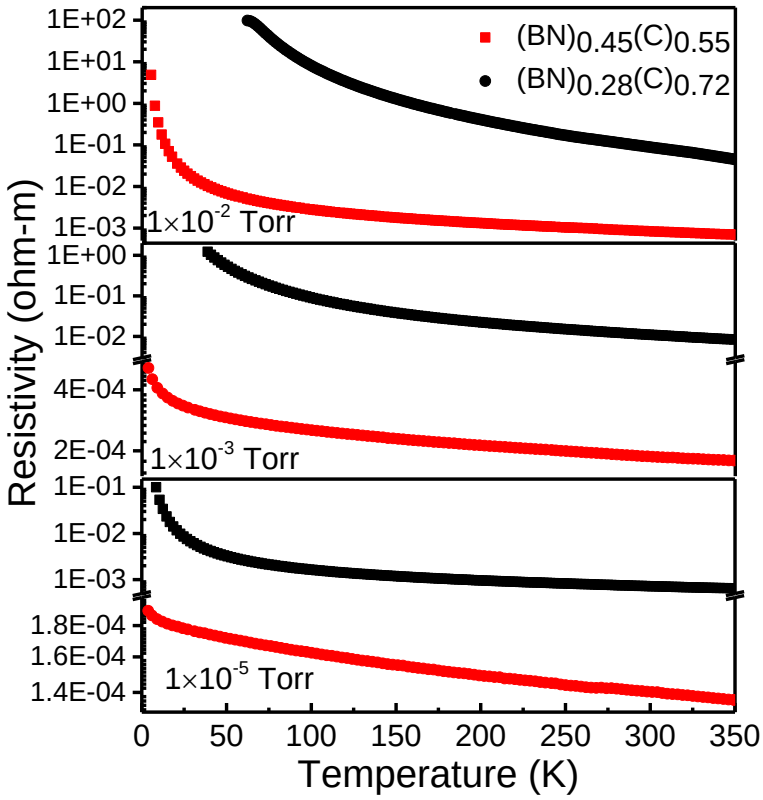

Figure 12. Temperature dependent resistivity plots of BCN films deposited from target composition $(BN)_{0.45}(C)_{0.55}$ and $(BN)_{0.28}(C)_{0.72}$, prepared using EG at (a) 1×10^{-5} Torr (b) 1×10^{-3} Torr N_2 (c) 1×10^{-2} Torr N_2.

Efros-Shklovskii (ES) VRH. The density of the localized electron states (DOS) near the Fermi level (E_F) is constant in Mott-VRH,[49] whereas according to EF-VRH at low temperature, the DOS of localized electrons is variable if the system doesn't have enough energy to make the DOS constant near E_F.[50] So, if the system is highly disordered, then it doesn't have enough energy to make the DOS constant near E_F, and thus, ES-VRH is dominating. But when the system is less disordered, it can manage to have a constant DOS around E_F, so than Mott-VRH is dominating. The temperature dependence of the electrical resistivity of $(BN)_{1-x}(C)_x$ films because of VRH in the ohmic regime is found to vary according to the equation given below[51]

$$\rho(T) = \rho_0 \exp\left(\frac{T_0}{T}\right)^{1/p} \qquad (4)$$

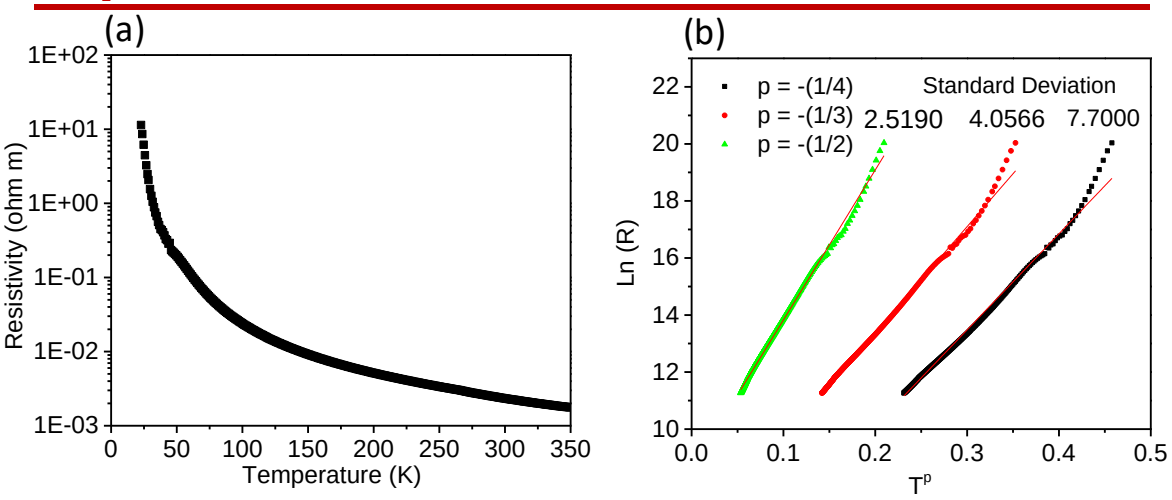

Figure 13: (a) Resistivity versus temperature curve of ultrathin film deposited with target composition of $(BN)_{0.45}(C)_{0.55}$ prepared using EG, at 1×10^{-5} Torr. (b) Linear curve fitting according to Mott-VRH (p= - (1/4), - (1/3)) and ES-VRH (p= - (1/2)).

Here, 'ρ' is the temperature dependent electrical resistivity, 'ρ_0' is the prefactor, 'T_0' is the characteristic temperature and 'p' is the characteristic exponent whose value determines the hopping mechanism. According to Mott, the value of 'p' in eq 4 is given as $p = 1/1+D$, where 'D' is the dimensionality of the system,[52] but in ES-VRH, the value of 'p' is 1/2, independent of the dimensionality of the system.[50] The characteristic temperature 'T_0' in eq 4 for ES-VRH can be derived as:[51]

$$T_0 = T_{ES} = \frac{2.8e^2}{4\pi\varepsilon\varepsilon_o k_B \xi} \qquad (5)$$

Here, 'e' is the charge of an electron, 'ε_0' and 'ε' are the value of permittivity in free space and the dielectric constant of the material respectively, 'k_B' is the Boltzmann constant, and '**ξ**' is the electron localization length in the system. **Figure 13(a)** shows the electrical resistivity as a function of temperature of the ultrathin film deposited from $(BN)_{0.45}(C)_{0.55}$ at 1×10^{-5} Torr. For clear understanding of the hopping mechanism in $(BN)_{1-x}(C)_x$ thin films, we have plotted the natural logarithm of resistance (ultrathin film from $(BN)_{0.45}(C)_{0.55}$) versus temperature according to eq 4 showing Mott-VRH as

well as ES-VRH for 2D and 3D systems. **Figure 13(b)** shows the best straight line fits with least standard deviation in the data form by ES-VRH behavior. We see a large standard deviation for Mott 3D systems occurs. The conduction mechanism in this system seems to follow the Efros-Shklovskii (ES) variable range hopping mechanism. The BCN films obtained from the targets prepared from activated carbon also show the similar electrical properties.

5. Conclusions

Thin films of borocarbonitrides, $(BN)_{1-x}(C)_x$ BCN for simplicity, of various compositions have been successfully deposited by PLD. It has been possible to vary the composition successfully to obtain different bandgaps. BCN films deposited on insulating transparent substrates allow us to probe their optical and electrical properties systematically. Even though there are a few literature reports on BCN films, the wide range of composition from graphene to BN has been achieved for the first time. The optical band gap of the films shows a nearly linear relationship with the composition in the range of 0 to 6 eV. The BCN films show semiconducting properties, and the electrical resistivity of the films varies with the composition, following the ES-VRH behaviour.

6. References

(1) Kumar, N.; Moses, K.; Pramoda, K.; Shirodkar, S. N.; Mishra, A. K.; Waghmare, U. V.; Sundaresan, A.; Rao, C. N. R. Borocarbonitrides, $B_xC_yN_z$. *J. Mater. Chem. A* **2013**, *1* (19), 5806.

(2) Rao, C. N. R.; Gopalakrishnan, K. Borocarbonitrides, $B_xC_yN_Z$: Synthesis, Characterization, and Properties with Potential Applications. *ACS Appl. Mater. Interfaces* **2017**, *9* (23), 19478–19494.

(3) Kubota, Y.; Watanabe, K.; Tsuda, O.; Taniguchi, T. Deep Ultraviolet Light-Emitting Hexagonal Boron Nitride Synthesized at Atmospheric Pressure. *Science (Washington, DC, U.S).* **2007**, *317* (5840), 932–934.

(4) Geim, A. K.; Novoselov, K. S. The Rise of Graphene. *Nat. Mater.* **2007**, *6* (3), 183–191.

(5) Rao, C. N. R.; Gopalakrishnan, K.; Maitra, U. Comparative Study of Potential Applications of Graphene, MoS_2, and Other Two-Dimensional Materials in Energy Devices, Sensors, and Related Areas. *ACS Appl. Mater. Interfaces* **2015**, *7* (15), 7809–7832.

(6) CAPASSO, F. Band-Gap Engineering: From Physics and Materials to New Semiconductor Devices. *Science (Washington, DC, U.S).* **1987**, *235* (4785), 172–176.

(7) Han, M. Y.; Özyilmaz, B.; Zhang, Y.; Kim, P. Energy Band-Gap Engineering of Graphene Nanoribbons. *Phys. Rev. Lett.* **2007**, *98* (20), 206805.

(8) Zhou, S. Y.; Gweon, G.-H.; Fedorov, A. V.; First, P. N.; de Heer, W. A.; Lee, D.-H.; Guinea, F.; Castro Neto, A. H.; Lanzara, A. Substrate-Induced Bandgap Opening in Epitaxial Graphene. *Nat. Mater.* **2007**, *6* (10), 770–775.

(9) Giovannetti, G.; Khomyakov, P. A.; Brocks, G.; Kelly, P. J.; van den Brink, J. Substrate-Induced Band Gap in Graphene on Hexagonal Boron Nitride: Ab Initio Density Functional Calculations. *Phys. Rev. B* **2007**, *76* (7), 073103.

(10) Liu, L.; Shen, Z. Bandgap Engineering of Graphene: A Density Functional Theory Study. *Appl. Phys. Lett.* **2009**, *95* (25), 252104.

(11) Rao, C. N. R.; Gopalakrishnan, K.; Govindaraj, A. Synthesis, Properties and Applications of Graphene Doped with Boron, Nitrogen and Other Elements. *Nano Today* **2014**, *9* (3), 324–343.

(12) Panchakarla, L. S.; Subrahmanyam, K. S.; Saha, S. K.; Govindaraj, A.; Krishnamurthy, H. R.; Waghmare, U. V.; Rao, C. N. R. Synthesis, Structure, and Properties of Boron- and Nitrogen-Doped Graphene. *Adv. Mater.* **2009**, *21* (46), 4726-4730.

(13) Moses, K.; Shirodkar, S. N.; Waghmare, U. V.; Rao, C. N. R. Composition-Dependent Photoluminescence and Electronic Structure of 2-Dimensional Borocarbonitrides, BC_XN (x = 1, 5). *Mater. Res. Express* **2014**, *1* (2), 025603.

(14) D'Souza, R.; Mukherjee, S. Electronic Structure, Phase Stability and Resistivity of Hybrid Hexagonal $C_X(BN)_{1-X}$ two-Dimensional Nanomaterial: A First-Principles Study. *Phys. E Low-Dimensional Syst. Nanostructures* **2015**, 69, 138-144.

(15) Ci, L.; Song, L.; Jin, C.; Jariwala, D.; Wu, D.; Li, Y.; Srivastava, A.; Wang, Z. F.; Storr, K.; Balicas, L.; Atomic Layers of Hybridized Boron Nitride and Graphene Domains. *Nat. Mater.* **2010**, *9* (5), 430–435.

(16) Song, L.; Balicas, L.; Mowbray, D. J.; Capaz, R. B.; Storr, K.; Ci, L.; Jariwala, D.; Kurth, S.; Louie, S. G.; Rubio, A.; Anomalous Insulator Metal Transition in Boron Nitride-Graphene Hybrid Atomic Layers. *Phys. Rev. B* **2012**, *86* (7), (075429)

(17) Muchharla, B.; Pathak, A.; Liu, Z.; Song, L.; Jayasekera, T.; Kar, S.; Vajtai, R.; Balicas, L.; Ajayan, P. M.; Talapatra, S.; et al. Tunable Electronics in Large-Area Atomic Layers of Boron–Nitrogen–Carbon. *Nano Lett.* **2013**, *13* (8), 3476–3481.

(18) Kim, D. H.; Byon, E.; Lee, S.; Kim, J.-K.; Ruh, H. Characterization of Ternary Boron Carbon Nitride Films Synthesized by RF Magnetron Sputtering. *Thin Solid Films* **2004**, *447–448*, 192–196.

(19) Prakash, A.; Sundaram, K. B.; Campiglia, A. D. Photoluminescence Studies on BCN Thin Films Synthesized by RF Magnetron Sputtering. *Mater. Lett.* **2016**, *183*, 355–358.

(20) Hirte, T.; Feuerfeil, R.; Perez-Solorzano, V.; Wagner, T. A.; Scherge, M. Influence of Composition on the Wear Properties of Boron Carbonitride (BCN) Coatings Deposited by High Power Impulse Magnetron Sputtering. *Surf. Coatings Technol.* **2015**, *284*, 94–100.

(21) Sugino, T.; Hieda, H. Field Emission Characteristics of Boron Carbon Nitride Films Synthesized by Plasma-Assisted Chemical Vapor Deposition. *Diam. & Relat. Mater.* **2000**, *9* (3–6), 1233–1237.

(22) Yuki, T.; Umeda, S.; Sugino, T. Electrical and Optical Characteristics of Boron Carbon Nitride Films Synthesized by Plasma-Assisted Chemical Vapor Deposition. *Diam. Relat. Mater.* **2004**, *13* (4–8), 1130–1134.

(23) Puyoo, G.; Teyssandier, F.; Pailler, R.; Labrugère, C.; Chollon, G. Boron Carbonitride Coatings Synthesized by LPCVD, Structure and Properties. *Carbon* **2017**, *122*, 19–46.

(24) Matsoso, B. J.; Ranganathan, K.; Mutuma, B. K.; Lerotholi, T.; Jones, G.; Coville, N. J. Synthesis and Characterization of Boron Carbon Oxynitride Films

with Tunable Composition Using Methane, Boric Acid and Ammonia. *New J. Chem.* **2017**, *41* (17), 9497–9504.

(25) Perrone, A.; Caricato, A. .; Luches, A.; Dinescu, M.; Ghica, C.; Sandu, V.; Andrei, A. Boron Carbonitride Films Deposited by Pulsed Laser Ablation. *Appl. Surf. Sci.* **1998**, *133* (4), 239–242.

(26) Yang, Q.; Wang, C. B.; Zhang, S.; Zhang, D. M.; Shen, Q.; Zhang, L. M. Effect of Nitrogen Pressure on Structure and Optical Properties of Pulsed Laser Deposited BCN Thin Films. *Surf. Coatings Technol.* **2010**, *204* (11), 1863–1867.

(27) Zhang, S.; Wu, J.; Yang, Q.; Tu, R.; Wang, C.; Shen, Q.; Zhang, L. Stoichiometric Controlling of Boroncarbonitride Thin Films with Using BN-C Dual-Targets. *AIP Adv.* **2015**, *5* (4), 047125.

(28) Xiao, J. L.; Wang, C. B.; Shen, Q.; Zhang, L. M. Influence of Nitrogen Pressure on Bonding Structure and Mechanical Properties of Pulsed Laser Deposited BCN Thin Films. *Surf. Coatings Technol.* **2015**, *276*, 141–144.

(29) Wang, C. B.; Xiao, J. L.; Shen, Q.; Zhang, L. M. Bonding Structure and Mechanical Properties of B-C-N Thin Films Synthesized by Pulsed Laser Deposition at Different Laser Fluences. *Thin Solid Films* **2016**, *603*, 323–327.

(30) Lowndes, D. H.; Geohegan, D. B.; Puretzky, A. A.; Norton, D. P.; Rouleau, C. M. Synthesis of Novel Thin-Film Materials by Pulsed Laser Deposition. *Science (Washington, DC, U.S).* **1996**, *273* (5277), 898–903.

(31) Eason, R. *Pulsed Laser Deposition of Thin Films: Applications-Led Growth of Functional Materials*; 2006.

(32) Chen, L.-C.; Hall, E. L. Nature and Application of Particulate Matter Produced by Pulsed Laser Ablation. *MRS Proc.* **1992**, *285*, 519.

(33) Venkatesan, T.; Wu, X. D.; Inam, A.; Wachtman, J. B. Observation of Two Distinct Components during Pulsed Laser Deposition of High Tc Superconducting Films. *Appl. Phys. Lett.* **1988**, 52, 1193-1195

(34) Sreedhara, M. B.; Gopalakrishnan, K.; Bharath, B.; Kumar, R.; Kulkarni, G. U.; Rao, C. N. R. Properties of Nanosheets of 2D-Borocarbonitrides Related to Energy Devices, Transistors and Other Areas. *Chem. Phys. Lett.* **2016**, *657*, 124–130.

(35) Hummers, W. S.; Offeman, R. E. Preparation of Graphitic Oxide. *J. Am. Chem. Soc.* **1958**, 80 (6), 1339.

(36) Subrahmanyam, K. S.; Vivekchand, S. R. C.; Govindaraj, A.; Rao, C. N. R. A Study of Graphenes Prepared by Different Methods: Characterization, Properties and Solubilization. *J. Mater. Chem.* **2008**, *18* (13), 1517-1523.

(37) Barua, M.; Sreedhara, M. B.; Pramoda, K.; Rao, C. N. R. Quantification of Surface Functionalities on Graphene, Boron Nitride and Borocarbonitrides by

Fluorescence Labeling. *Chem. Phys. Lett.* **2017**, *683*, 459–466.

(38) Kumar, N.; Raidongia, K.; Mishra, A. K.; Waghmare, U. V.; Sundaresan, A.; Rao, C. N. R. Synthetic Approaches to Borocarbonitrides, BC_xN (X=1-2). *J. Solid State Chem.* **2011**, *184* (11), 2902–2908.

(39) Wei, Q.; Sankar, J.; Sharma, A. K.; Yamagata, Y.; Narayan, J. Effect of Chamber Pressure and Atmosphere on the Microstructure and Nanomechanical Properties of Amorphous Carbon Films Prepared by Pulsed Laser Deposition. *J. Vac. Sci. Technol. A Vacuum, Surfaces, Film.* **2001**, *19* (1), 311–316.

(40) Leapman, R. D.; Fejes, P. L.; Silcox, J. Orientation Dependence of Core Edges from Anisotropic Materials Determined by Inelastic Scattering of Fast Electrons. *Phys. Rev. B* **1983**, *28* (5), 2361–2373.

(41) Arenal, R.; Kociak, M.; Zaluzec, N. J. High-Angular-Resolution Electron Energy Loss Spectroscopy of Hexagonal Boron Nitride. *Appl. Phys. Lett.* **2007**, *90* (20), 204105.

(42) Kumar, R.; Gopalakrishnan, K.; Ahmad, I.; Rao, C. N. R. BN-Graphene Composites Generated by Covalent Cross-Linking with Organic Linkers. *Adv. Funct. Mater.* **2015**, *25* (37), 5910–5917.

(43) Saha, S.; Muthu, D. V. S.; Golberg, D.; Tang, C.; Zhi, C.; Bando, Y.; Sood, A. K. Comparative High Pressure Raman Study of Boron Nitride Nanotubes and Hexagonal Boron Nitride. *Chem. Phys. Lett.* **2006**, *421* (1–3), 86–90.

(44) Ferrari, A. C. Raman Spectroscopy of Graphene and Graphite: Disorder, Electron-Phonon Coupling, Doping and Nonadiabatic Effects. *Solid State Commun.* **2007**, *143* (1–2), 47–57.

(45) Tauc, J.; Grigorovici, R.; Vancu, A. Optical Properties and Electronic Structure of Amorphous Germanium. *Phys. status solidi* **1966**, *15* (2), 627–637.

(46) Oppedisano, C.; Tagliaferro, A. Relationship between Sp_2 Carbon Content and E04 Optical Gap in Amorphous Carbon-Based Materials. *Appl. Phys. Lett.* **1999**, *75* (23), 3650–3652.

(47) Dasgupta, D.; Demichelis, F.; Pirri, C. F.; Tagliaferro, A. π Bands and Gap States from Optical Absorption and Electron-Spin-Resonance Studies on Amorphous Carbon and Amorphous Hydrogenated Carbon Films. *Phys. Rev. B* **1991**, *43* (3), 2131–2135.

(48) Zrudsky, D. R.; Bush, H. D.; Fassett, J. R. Four Point Sheet Resistivity Techniques. *Rev. Sci. Instrum.* **1966**, *37* (7), 885–890.

(49) Davis, E. A.; Mott, N. F. Conduction in Non-Crystalline Systems V. Conductivity, Optical Absorption and Photoconductivity in Amorphous Semiconductors. *Philos. Mag.* **1970**, *22* (179), 0903–0922.

(50) Efros, A. L.; Shklovskii, B. I. Coulomb Gap and Low Temperature Conductivity of Disordered Systems. *J. Phys. C Solid State Phys.* **1975**, *8* (4), L49–L51.

(51) Joung, D.; Khondaker, S. I. Efros-Shklovskii Variable-Range Hopping in Reduced Graphene Oxide Sheets of Varying Carbon Sp2 Fraction. *Phys. Rev. B - Condens. Matter Mater. Phys.* **2012**, *86* (23), 235423

(52) Mott, N.; Pepper, M.; Pollitt, S.; Wallis, R. H.; Adkins, C. J. The Anderson Transition. *Proc. R. Soc. A Math. Phys. Eng. Sci.* **1975**, *345* (1641), 169–205.

Chapter I.2

Low Thermal Conductivity of 2D Borocarbonitride Nanosheets

Summary*

Two-dimensional borocarbonitrides (BCN for short) are of interest since their electrical and optical properties can be tuned for renewable energy applications. Although there have been theoretical studies, experimental studies of the thermal transport and thermoelectric properties of BCN nanosheets have not yet been explored. We have synthesized few-layer BCN nanosheets of different compositions, and characterized them by Raman spectroscopy, X-ray photoelectron spectroscopy and transmission electron microscopy. They exhibit *p*-type semiconducting thermoelectric transport properties in 300-573 K range. More interestingly, the BCN nanosheets exhibit low thermal conductivity (0.58 to 1.86 W/mK) unlike hexagonal boron nitride and graphene over the temperature range of 300-573 K. The low thermal conductivity of BCN nanosheets arises due to significant phonon scattering by the different length scale hierarchical nano/meso architectures such as bonding heterogeneity (e.g. C–B, C–N and B–N), point defects related C/B/N disorder, nanodomains of BN/carbon and grain boundaries.

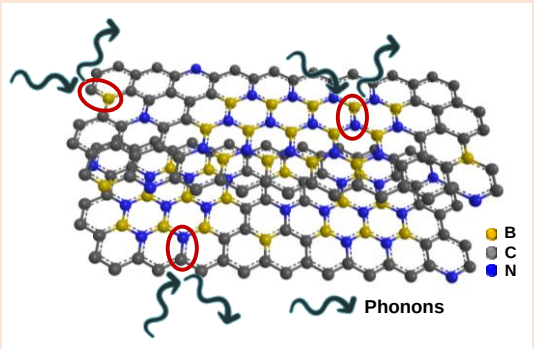

* A paper based on this study is published in Journal of Solid State Chemistry, 2020

1. Introduction

Graphene, a two-dimensional (2D) material, has drawn significant attention from researchers because of its outstanding electrical, thermal and physical properties.[1-3] The discovery of graphene has inspired the development of other 2D nanomaterials with unique properties opening a pathway for the next generation optical, electronic and energy conversion materials.[4-6] Hexagonal boron nitride (h-BN) with a wide band gap is one of the most studied 2D materials and has significant applications.[5] Borocarbonitrides, $B_xC_yN_z$ (BCN for short), with a similar honeycomb lattice, are a new class of 2D layered material that possesses unique electrical and physical properties which are distinct from graphene and h-BN.[7,8] The physical properties of BCN are determined by the composition of hybridized B, N, and C atoms. BCN nanosheets are different from those of graphene/BN hybrids,[9] and B, N co-doped graphene,[10] as they contain h-BCN rings along with graphene and boron nitride domains in the network.[7,11] BCN materials are of interest because experimental and theoretical studies have shown the possibility of band gap tuning between graphene (gapless semiconductor[1]) to BN (large band gap (~6 eV) insulator[12]), thereby enabling possible uses in nanoelectronics,[13-15] as well as energy devices, electrochemical sensors, and non-metal catalysis.[8,11,16,17]

2D materials exhibit low thermal conductivity due to phonon scattering because of the interfaces and short length scale boundaries which impede the transport of heat.[18-20] Low thermal conductive solids are efficient candidates for thermoelectrics which can convert waste heat to electricity without any moving parts and toxic gas emission.[21-23] Sevinçli *et al.* have recently reported the thermoelectric properties of graphene.[24] The

major issue with graphene is its very high thermal conductivity.[2] The open question is whether BCN with similar honeycomb lattice like graphene will show low thermal conductivity or not. Among the various physical properties of BCN nanosheets, less attention has been given to the thermal properties. Recently, Klein and co-workers have reported the theoretical behaviour of phonons and thermal conductivity of BCN using classical molecular dynamics (MD) simulations.[25] They have predicted that the thermal conductivity of BCN monolayer to be lower than that of both the graphene and h-BN monolayers at room temperature because of significant phonon-phonon scattering due to hybridization of B, N, and C atoms.[25] Lin *et al.* have predicted the dependence of length, strain, and temperature on energetically favorable BC_2N monolayer using MD,[26] while Zhang *et al.* have reported temperature independent thermal conductivity of the h-BCN monolayer in the in-plane direction.[27] Detailed experimental studies of the thermoelectric properties of BCN nanosheets are however lacking. We therefore considered it noteworthy to investigate the thermal transport properties of BCN nanosheets for possible use as thermal management devices.

In this study, we present experimentally measured low thermal conductivity data of several compositions of few-layer 2D BCN materials, prepared by the solid-state reactions. Temperature-dependent electrical conductivity and Seebeck coefficient data confirm *p*-type semiconducting behavior of the nanosheets. More importantly, 2D BCN materials show low thermal conductivity throughout the 300-573 K temperature range, possibly arises due to the presence of heteropolar bonding, rich point defects, disordered BN and carbon nanodomains and grain boundaries which favor significant phonon scattering.

2. Scope of the present investigations

Graphene and h-BN are both two-dimensional (2D) materials with interesting electronic studies and properties.[1,2,5] Graphene is a zero bandgap material,[1] while h-BN is a wide bandgap (~6 eV) insulator.[12] Borocarbonitrides ($B_xC_yN_z$) are the 2D materials which have shown the possibility of bandgap tuning between graphene and h-BN.[8,13] 2D materials exhibiting low thermal conductivity are potential candidates for thermoelectric applications.[20,22] It is therefore worthwhile to explore the thermoelectric transport properties of 2D BCN materials. Four different compositions of BCN have been synthesized by solid state reactions. We have measured the thermal conductivity, electrical conductivity, and the Seebeck coefficient of these materials in the temperature range of 300-573 K. The study throws light on the potential use of BCN in thermal management devices.

3. Experimental section

Reagents

Boric acid (H_3BO_3, Merck), urea (analytical reagent, CH_4N_2O, SDFC), activated charcoal (analytical reagent, SDFC) were bought from commercial sources and were used without any further processing.

Synthesis

In a typical synthesis of BCN by urea method, boric acid (as boron source) was added to 20 ml deionized water taken in 100 ml beaker followed by sonication. After complete dissolution, urea (as nitrogen source) was added to the solution and allowed to dissolve completely with continuous sonication. Then activated charcoal (as carbon source) was

added pinch by pinch to the solution to avoid agglomeration and the solution was sonicated for 25 min to make a homogenous mixture. The solution was then transferred to a petri-dish kept at 80 ^{O}C to allow the water to evaporate slowly. After some time when very little water was left, the resultant slurry was transferred to a alumina boat, the boat was kept inside a quartz tube and heated to 900 ^{O}C with the controlled rate of 5 ^{O}C/min for 10 hours under inert atmosphere followed by the cooling rate of 5 ^{O}C/min. Four different compositions of BCN were synthesized by varying the precursor ratio employed for synthesis.

The as-synthesized powders were pressed into cylindrical-shaped pellets having 10 mm diameter by using spark plasma sintering system (SPS211-LX, Dr. Sinter Lab) where 35 MPa of axial pressure was applied for 5 min at 550 °C in vacuum. The SPS'ed sample was further cut and polished for electrical and thermal transport measurement.

Characterization

Thermogravimetric analysis

The thermo-gravimetric compositions of layered BCN were determined by thermogravimetric analyses with a Metler Toledo TGA-850 TG analyzer at the ramping rate of 5 °C/min, carried out in an oxygen atmosphere.

Powder X-ray diffraction

Powder X-ray diffraction patterns were collected using a Rigaku Smart Lab diffractometer using Cu-Kα radiation with accelerating voltage 40 kV and current 30 mA.

Raman Spectroscopy

The acquisitions of Raman Spectra were collected by Jobin Yvon LabRAM HR 800 Raman spectrometer in the backscattering geometry using the excitation source of 514.5 nm (green laser).

X-Ray Photoelectron Spectroscopy

The bonding nature and the elemental composition of BCN were determined by X-ray photoelectron spectroscopy (XPS) in an Omicron nanotechnology spectrometer with Al-K_α as a monochromatic X-ray source ($h\upsilon$=1486.7 eV) at the power of 300 W. The step size of 0.05 eV and constant pass energy (PE) mode set to 25 eV for high resolution narrow spectra. All measurements were done with 54.7^o take-off angle with respect to the sample surface and in the base pressure of 1×10^{-9} Torr.

Field Emission Scanning Electron Microscopy

The surface morphology and elemental mapping of the BCN nanosheets were observed in Nova NanoSEM 600 FESEM at different magnification with accelerating voltage of 15 kV (for imaging) and 20 kV (for Energy Dispersive X-Ray Spectroscopy and Elemental mapping).

Transmission Electron Microscopy

TEM images of BCN nanosheets were acquired from FEI TECNAI $G^2$20 S-Twin TEM operating at 200 kV, fitted with a Gatan CCD camera. Elemental color mapping using EDS was performed during STEM imaging in FEI TECNAI $G^2$20 S-Twin TEM. Background was subtracted (using multi-polynomial model) during the data processing for EDS elemental mapping (with 500 eV minimum region of interest width).

Electrical transport

Electrical transport measurements were performed along the pressing direction of SPS'ed pellet. Electrical conductivity and Seebeck coefficients were measured simultaneously under helium (He) atmosphere from 300-573 K on a ULVAC-RIKO

ZEM-3 instrument. The typical sample with the dimensions of ~ 2×2×8 mm^3 (parallelepiped shape) was used for the measurement. The longer direction coincides with the direction in which the thermal conductivity was measured.

Hall measurement

To determine carrier concentration, Hall measurements have been carried out using four-contact Hall-bar geometry, in a magnetic field of 0.57 T at room temperature in equipment developed by Excel Instruments.

Thermal transport

Thermal conductivity was measured along the pressing direction of SPS'ed pellet. Thermal diffusivity, D, was measured in the range of 300–573 K by using a laser flash diffusivity method in a Netzsch LFA-457 instrument. Coins with ~ 8 mm diameter and ~ 2 mm thickness were used in all the measurements. The total thermal conductivity, κ_{total}, was calculated using the formula, $\kappa_{tot} = DC_p\rho$, where ρ is the density of the sample and Cp is the heat capacity using the Dulong–Petit limit. Electrical thermal

Table 1: Gravimetric composition of the as-synthesized BCN sheets along with the precursor ratio employed for synthesis.

Sample	Gravimetric composition	Activated charcoal (mg)	Boric acid (mg)	Urea (g)
BCN-1	$(BN)_{0.15}(C)_{0.85}$	500	60	2.4
BCN-2	$(BN)_{0.27}(C)_{0.73}$	275	60	2.4
BCN-3	$(BN)_{0.45}(C)_{0.55}$	150	60	2.4
BCN-4	$(BN)_{0.70}(C)_{0.30}$	30	60	2.4

conductivity, κ_{el} for all the samples was estimated by using Wiedemann-Franz's law, $\kappa_{el} = L\sigma T$. Temperature-dependent Lorenz number, L for all the samples were obtained based on fitting the respective temperature-dependent Seebeck value.

4. Results and discussion

The BCN materials were synthesized by solid state reaction employing urea, activated charcoal and boric acid as precursor,[7] (see details in experimental section). The layered BCN materials were characterized by various spectroscopic and microscopic techniques. **Figure 1a** represents a schematic of BCN layers incorporating BN and carbon domains along with B and N atoms in the layers. We have obtained four different compositions of BCN [$(BN)_{0.15}(C)_{0.85}$, $(BN)_{0.27}(C)_{0.73}$, $(BN)_{0.45}(C)_{0.55}$ and $(BN)_{0.70}(C)_{0.30}$, for simplicity labelled as BCN-1 to BCN-4] by varying the proportion of precursors i.e. boric acid, urea, and activated charcoal as shown in **Table 1**. The BCN so prepared were spark plasma sintered (SPS) to obtain dense pellets for thermal conductivity measurements. The density of BCN pellets (**Table 2**) was found

Table 2. Carrier concentration of the layered BCN samples along with the gravimetric compositions, and density of SPS'ed BCN samples measured by Archimedes method.

Sample	Gravimetric composition	Carrier concentration (cm^{-3})	Density (g/cm^3)
BCN-1	$(BN)_{0.15}(C)_{0.85}$	8.54×10^{17}	1.06
BCN-2	$(BN)_{0.27}(C)_{0.73}$	8.26×10^{17}	1.30
BCN-3	$(BN)_{0.45}(C)_{0.55}$	7.40×10^{17}	1.62
BCN-4	$(BN)_{0.70}(C)_{0.30}$	2.43×10^{17}	2.0

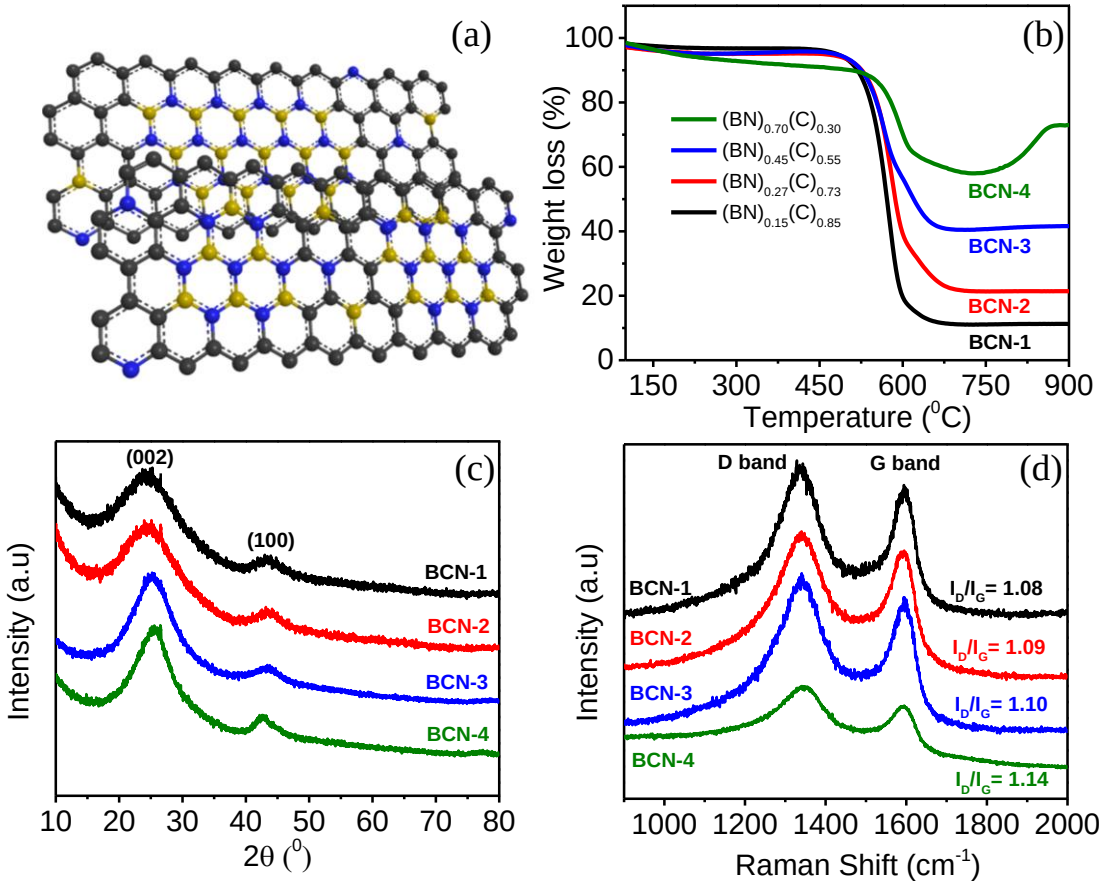

Figure 1. (a) Schematic of the layered $B_xC_yN_z$ sheets [carbon (black), boron (yellow) and nitrogen (blue)], (b) TGA curve of the as synthesized BCN samples, (c) PXRD pattern of various compositions of BCN nanosheets, (d) Raman spectra with the corresponding I_D/I_G ratio of different compositions of BCN.

to be dependent on the composition (increasing with BN content) because of variation in density of h-BN and graphene nanosheets.[28]

The chemical composition of $(BN)_{1-x}(C)_x$ samples was determined by thermogravimetric analysis (TGA) performed in an oxygen atmosphere. **Figure 1b** shows thermogravimetric curves of the BCN nanosheets. BCN-1 shows the highest carbon content with the composition $(BN)_{0.15}(C)_{0.85}$ and BCN-4 with the least carbon content with the composition $(BN)_{0.70}(C)_{0.30}$. BCN-4 shows the high thermal stability compare to BCN-1 because of high BN content.[16] The chemical compositions of the BCN samples were further verified by X-ray photoelectron spectroscopy (XPS) and

Table 3. Crystallite size calculated from I_D/I_G ratio (Raman spectroscopy) of different compositions of BCN samples.

Sample	Chemical composition	I_D/I_G ratio	Crystallite size (nm)
BCN-1	$(BN)_{0.15}(C)_{0.85}$	1.08	15.6
BCN-2	$(BN)_{0.27}(C)_{0.73}$	1.09	15.4
BCN-3	$(BN)_{0.45}(C)_{0.55}$	1.10	15.3
BCN-4	$(BN)_{0.70}(C)_{0.30}$	1.14	14.8

elemental quantification from EDS measurements.

Figure 1c shows the powder X-Ray diffraction (PXRD) patterns of BCN nanosheets. The broad reflection peak at ~25.1^{O} (2θ) corresponds to the (002) plane which indicates disordered nanosized domains. The peak shifts to lower angles compared to the graphitic (002) plane confirming exfoliation of the BCN sheets with increased interlayer spacing. A weak reflection peak around 42.7^{O} (2θ) corresponds to (100) plane of BCN.[29] BCN-1 sheets after the sintering process were again examined by PXRD. The full width of the half maximum (FWHM) of the (002) and (100) reflections were reduced after hot pressing compared to the as synthesized materials, showing increase in crystallite/grain size.[30] However, hot pressing also bought out a graphitic peak at 26.6 ^{O} (2θ) due to increased interlayer stacking of carbon domains. Interestingly, the FWHM remains similar after SPS processing compared to as the synthesized samples indicating that the nanodomains are intact.

Raman spectroscopy is widely used for the characterization of graphene like 2D materials which provides information about structural defects and dopant effects.[31,32] The spectra in **Figure 1d** of the as-synthesized BCN materials show the position of

characteristic D and G bands at 1338 cm^{-1} and 1597 cm^{-1} respectively, independent of the chemical composition. The characteristic G band arises from the in-plane vibration of sp^2 hybridized carbon atoms while the D band is due to defects/disorder.[8] The spectra show peak broadening with blue-shift in G band and red-shift in D band compared to graphene which is due to the increased defects or lattice distortion caused by BN nanodomains.[10] The intensity of the D band is higher than that of the G band because it also has contribution from the E_{2g} stretching mode of the BN domains besides D mode of the carbon domains.[33,34] Raman spectroscopy can be used to calculate the crystallite size of the sample which was profoundly used to investigate the phonon – phonon scattering length. The average crystallite size (L_a) was estimated from the peak intensity

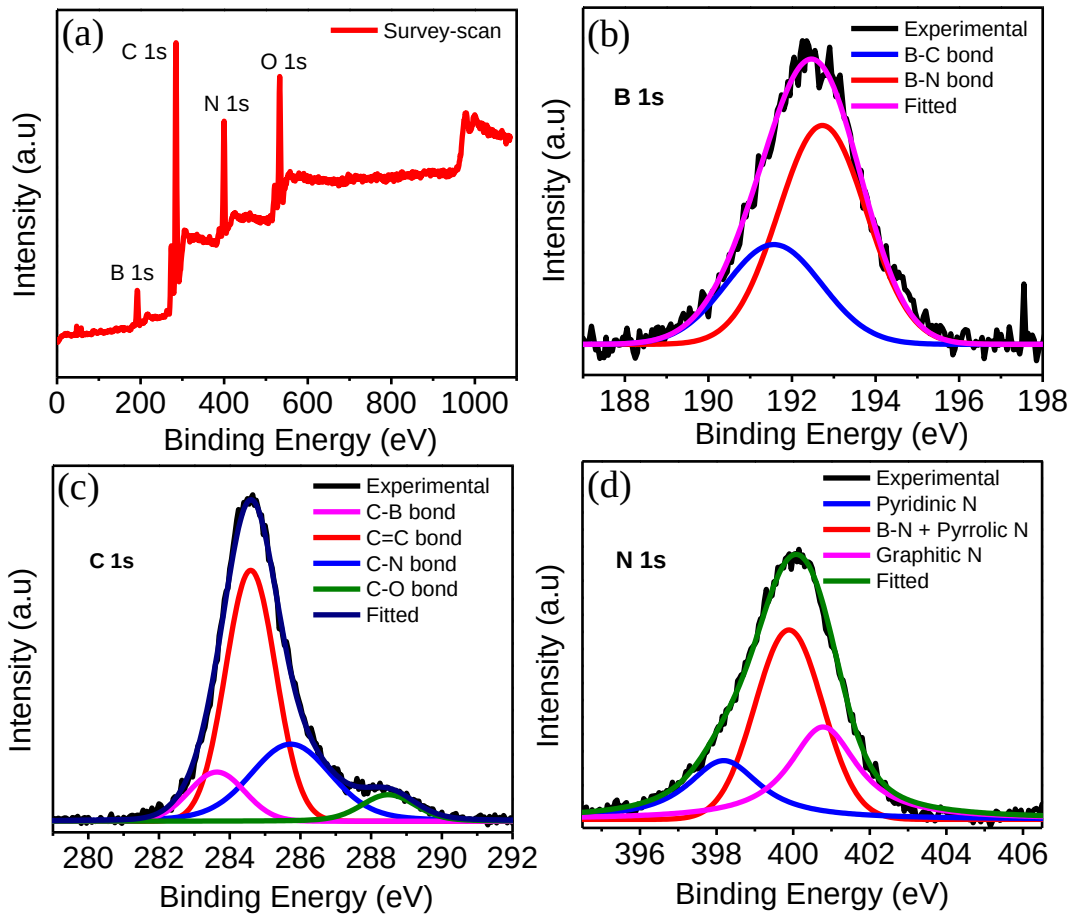

Figure 2. (a) XPS survey scan showing all elements of BCN-4, (b-d) Core level XPS spectrum of B 1s, C 1s, and N 1s signals of BCN-4, respectively.

of the D band (I_D) and G band (I_G) by using wavelength of incident light λ (514.5 nm) in an equation as mentioned below:[10]

$$L_a = (2.4 \times 10^{-10})\lambda^4 (I_D/I_G)^{-1}$$

The average crystallite size so obtained are tabulated in **Table 3**. BCN-1 shows a crystallite size of 15.6 nm and BCN-4 a size of 14.8 nm. It should be noted that there is no significant change in the average crystallite size with the compositions which indeed confirms the presence of BN/graphene nanodomains in the BCN.

X-ray photoelectron spectroscopy (XPS) was employed to understand the chemical bonding and composition of the BCN nanosheets. The XPS survey spectrum of BCN-4 shown in **Figure 2a** was carried out in the range of 0 to 1100 eV show peaks corresponds to boron, carbon, nitrogen and oxygen elements. The presence of oxygen is due to the surface functional groups on the carbon surface as shown by earlier work.[35] **Figure 2(b-d)** represent the 1s core level spectra due to boron, carbon and nitrogen. The high resolution B 1s XP spectrum (see **Figure 2b**) could be deconvoluted into two peaks corresponding to B-C and B-N bonds centered at 191.5 eV and 192.7 eV respectively.[17] The B-N bonds are more favorable than B-C bonds (analyzed from peak area) because of higher electronegativity of N. We did not observe any peak corresponding to B-O bonds in B 1s spectrum which confirms that oxygen can only be present on the carbon surface.[13] The high resolution C 1s spectrum (see **Figure 2c**) was deconvoluted into four peaks at 283.65 eV (C-B bonds), 284.6 eV (sp^2 carbon), 285.75 eV (C-N bonds) and at 288.5 eV (C-O bonds arising from surface functional groups).[7,8] BCN-4 contains more C-N bonds than C-B bonds because bond length of C-B is little bit higher than C-N bonds (C-N have almost same as C=C bonds) which make C-N bonds to be energetically more stable than C-B bonds.[10] The N 1s spectrum (see **Figure**

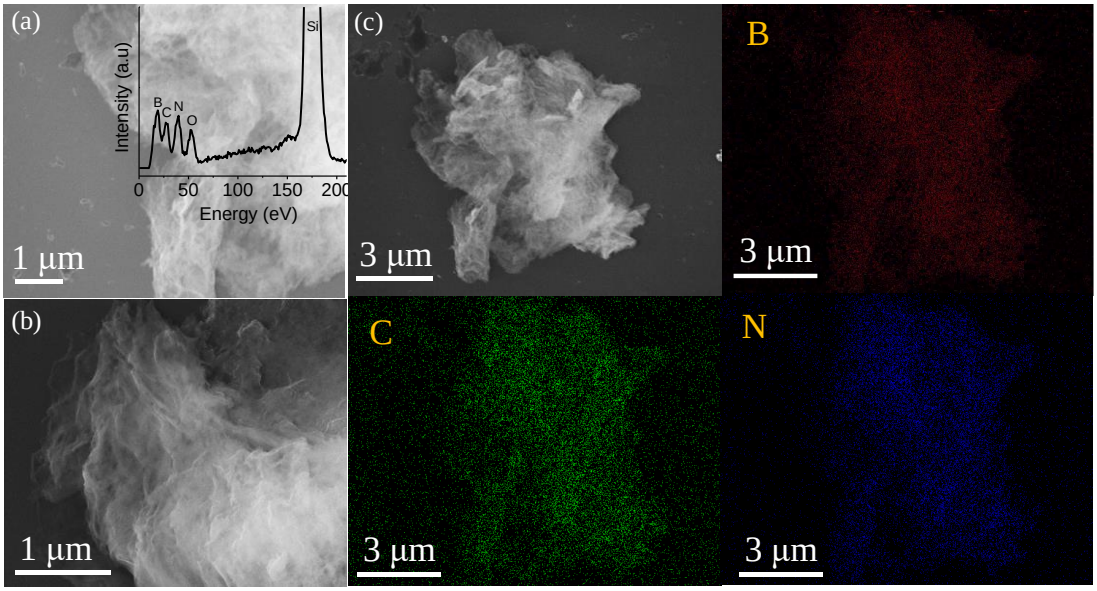

Figure 3. (a) FESEM image of BCN-4 (inset shows the corresponding EDS spectrum), (b) FESEM image of BCN-3, (c) FESEM image along with the EDS elemental mapping of BCN-4 nanosheets showing boron (red), carbon (green), and nitrogen (blue).

2d) was fitted into three major peaks assigned at 398.2 eV, 399.2 eV and 400.8 eV correspond to pyridinic nitrogen, N-B bonds sum up with pyrrolic nitrogen and graphitic nitrogen respectively. The XPS of BCN-3 was also deconvoluted and exhibits same features. Chemical compositions of BCN-4 ($B_{0.40}C_{0.33}N_{0.27}$) and BCN-3 ($B_{0.22}C_{0.61}N_{0.17}$) were calculated by taking the average of B, C and N, core level intensities and the Atomic Sensitivity Factor (ASF) of each element, and are in good agreement with the TGA results.

The surface morphology of the as-synthesized BCN was examined by field emission scanning electron microscopy (FESEM) and transmission electron microscopy (TEM). The FESEM images and the EDS data of BCN-4 (**Figure 3(a-b)**) show corrugated and entangled nanosheets. The EDS elemental color mapping of layered BCN sheets (**Figure 3c**) showing homogeneous distribution of B, N and C atoms up to a wide range. The entangled nature of BCN sheets is possibly due to the local strain to reduce the

surface energy as explained by *Jin et. al* for the boron and nitrogen co-doped graphite sheets.[36]

In **Figure 4(a,d)** we present typical TEM images of BCN-1 and BCN-3 showing uniform layers of BCN which are entangled with each other (inset of **Figure 4a**). The bright field scanning transmission electron microscopy (STEM) image of BCN-1 is shown in **Figure 4b**. The EDS elemental color mapping shows homogeneous distribution of boron (yellow), carbon (green) and nitrogen (dark cyan) atoms in the BCN nanosheets at sub-nanometer scale. Selected area electron diffraction patterns (SAED) (**Figure 4c**) show weak diffraction rings due to the highly disordered sheets (B/N disorder) and nanosized domains. The BCN nanosheets comprise of 6-8 layers

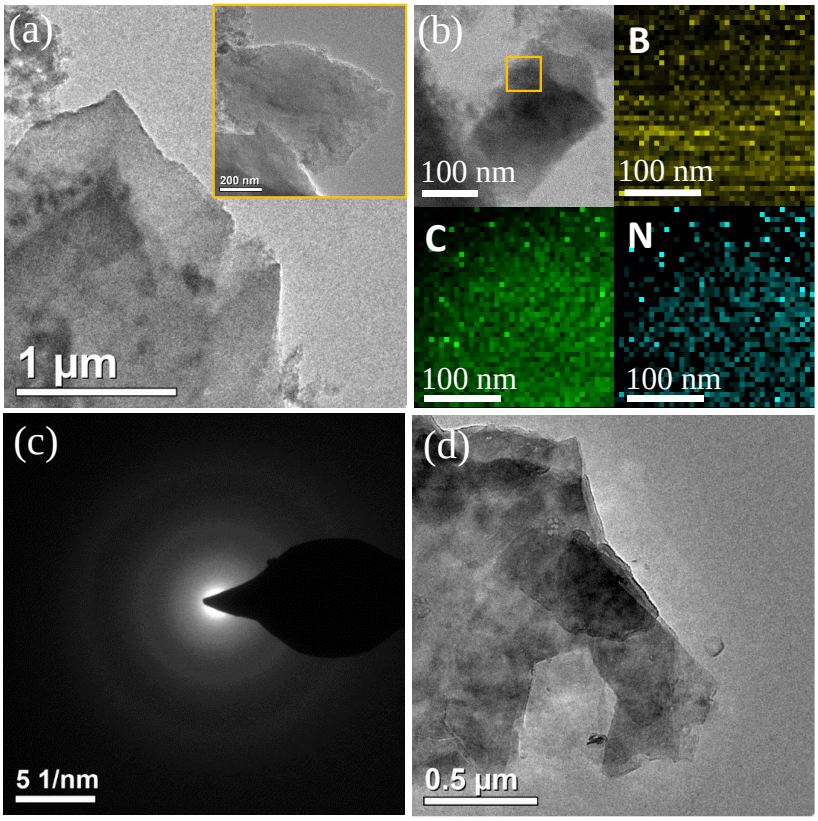

Figure 4. (a) TEM image of BCN-1 showing the 2D layered morphology of the nanosheets (inset shows the magnified image of nanosheets), (b) STEM image of BCN-1 nanosheets and the EDS color mapping of B,C, and N elements, (c) SAED of BCN-1 nanosheets, (d) TEM image of BCN-3.

(2.4-2.8 nm thick) with lateral dimension of a few microns (μm).[16]

Figure 5 presents the thermoelectric properties of $(BN)_{1-x}(C)_x$ (x = 0.30, 0.55, 0.73 and 0.85) nanosheets in the temperature range of 300−573 K. The thermoelectric properties were measured along the pressing direction of the SPS'ed samples. The electrical conductivity, σ, of the $(BN)_{1-x}(C)_x$ samples increases with increasing temperature, indicating typical semiconductor behaviour (**Figure 5a**). The σ of boron nitride rich composition *i.e.* $(BN)_{0.70}(C)_{0.30}$ is to be 19 S/m at 300 K, which linearly increases to 39 S/m at 573 K. The relatively low σ can be attributed to low carrier concentration (2.43 x 10^{17} cm^{-3}) of $(BN)_{0.70}(C)_{0.30}$ sample (**Table 2**) which is measured by Hall measurement. BN and graphene are the well-known insulator and semimetal, respectively.[1,12] Thus, with increasing carbon concentration in BCN, both the carrier concentration (**Table 2**) and electrical conductivity increases (**Figure 5a**), respectively. Typically, carbon rich composition *i.e.* $(BN)_{0.15}(C)_{0.85}$ exhibits electrical conductivity of ~ 1442 S/m at 295 K, which increases further to ~2141 S/m at 573 K. The electrical conductivity of various BCN compositions show tunable electronic structure between graphene and h-BN.

In **Figure 5b**, we show the temperature variations of the Seebeck coefficient, *S*, of the $(BN)_{1-x}(C)_x$ samples. In all of the compositions, Seebeck coefficient value is positive, indicating holes as the major carriers. This is consistent with the positive Hall coefficient data. The low value of the Seebeck coefficient could be attributed to several factors like comparatively low carrier concentration, the presence of nanodomains of BN/graphene, heteropolar bonds (C-B, C-N, B-N), and rich point defects related to C/B/N disorder. However, detailed study needs to be conducted for in-depth knowledge of the phenomena happening at atomically thick BCN materials.

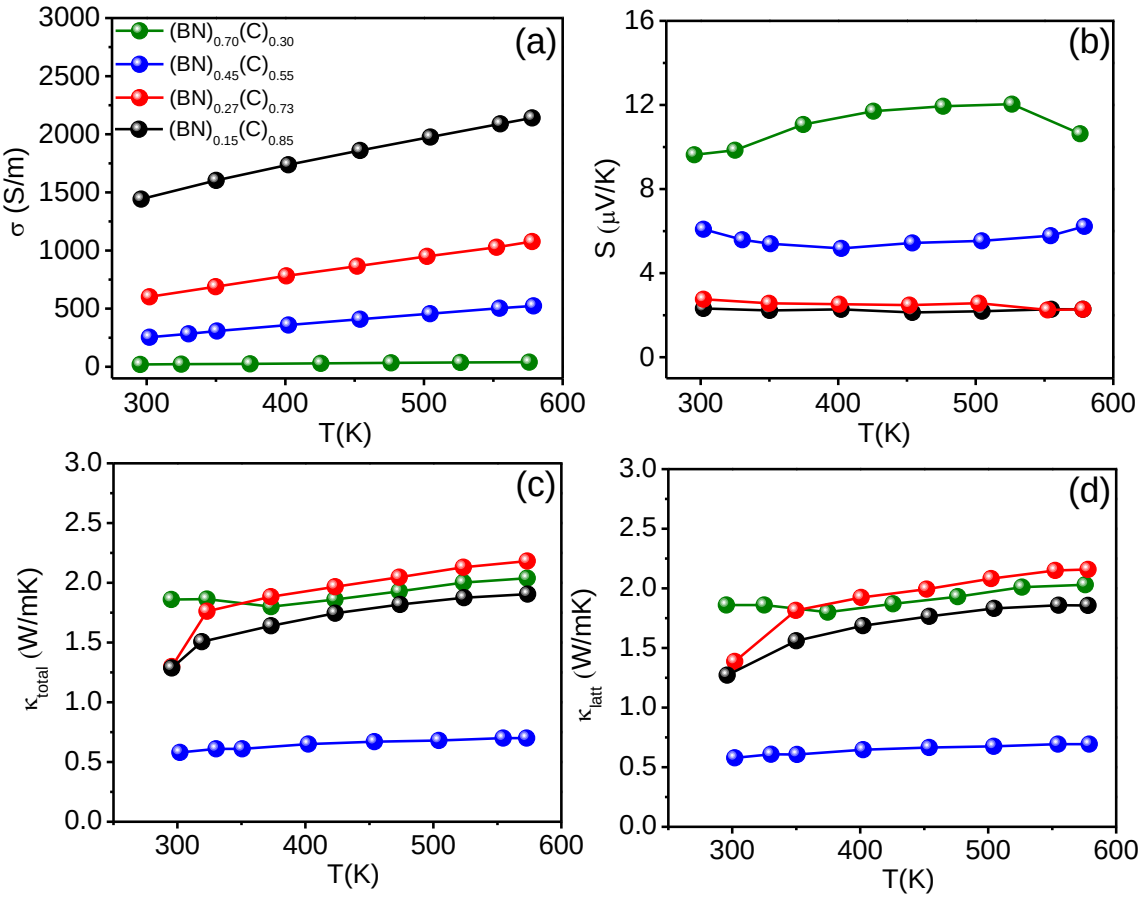

Figure 5. Temperature variation of (a) electrical conductivity (σ), (b) Seebeck coefficient (S), (c) total thermal conductivity (κ_{total}) and (d) lattice thermal conductivity (κ_{latt}) of $(BN)_{1-x}(C)_x$ (x = 0.30, 0.55,0.73,0.85) samples.

Figure 5c presents the temperature variation of total thermal conductivity, κ_{total}, of $(BN)_{1-x}(C)_x$ (x = 0.30, 0.55, 0.73 and 0.85) samples. Both graphene and boron nitride have ultrahigh thermal conductivity near room temperature. Interestingly, the boron nitride-rich composition *i.e.* $(BN)_{0.70}(C)_{0.30}$ and the carbon-rich composition *i.e.* $(BN)_{0.15}(C)_{0.85}$ exhibit κ_{total} of ~ 1.86 W/mK and ~ 1.30 W/mK, respectively near room temperature. The total thermal conductivity remains almost temperature independent throughout the 300−573 K range. **Figure 5d** shows the temperature variation of lattice thermal conductivity, κ_{latt}. Thermal diffusivity, D, BCN nanosheets was measured in the range of 300–573 K are presented in **Figure 6a**, and the lattice thermal conductivity,

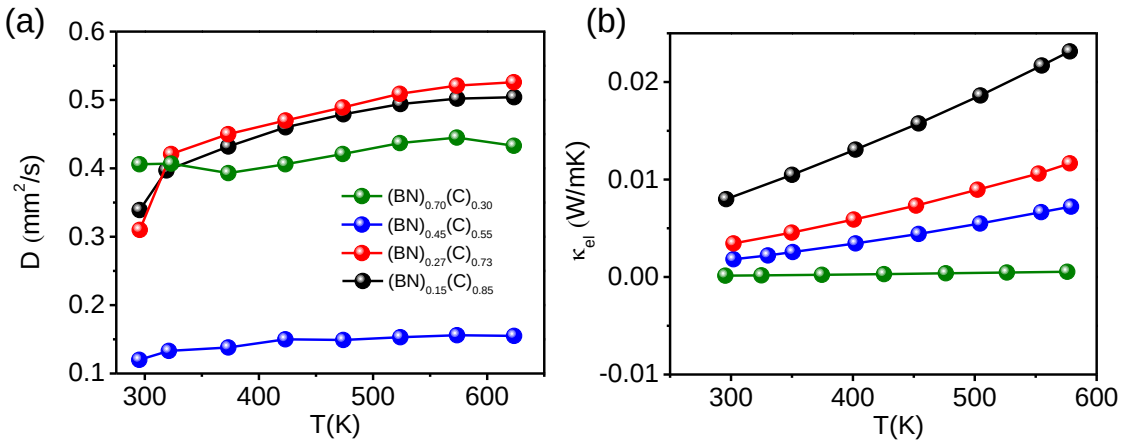

Figure 6. Temperature variation of (a) thermal diffusivity (D) and (b) electrical thermal conductivity (κ_{el}) of $(BN)_{1-x}(C)_x$ (x = 0.30, 0.55,0.73,0.85) samples.

κ_{latt}, was estimated by subtracting the electrical thermal conductivity (**Figure 6b**) from κ_{total}. At room temperature, $(BN)_{0.45}(C)_{0.55}$ and $(BN)_{0.70}(C)_{0.30}$ nanosheets exhibit κ_{latt} of 0.57 W m^{-1} K^{-1} and 1.85 W m^{-1} K^{-1} respectively. Nanostructuring, which increases the scattering of short and medium wavelength phonons, is a well-known strategy of reducing materials thermal conductivity.[37] In the present BCN samples, the presence of nanodomains is evident from the TEM images and is one of the dominant factors for the experimentally observed low thermal conductivity. Additionally, SPS processing, in general, increases the grain size and these meso-scale grain boundaries, which in turn increases the scattering of long wavelength phonons (mean free paths ~ 0.1–1 mm).[38] Such grain-boundary scattering played an important role in enhancing the thermoelectric performance of PbTe and Bi_2Te_3 based alloys.[38,39] Moreover, points defects in the lattice due to disordered B, C, and N atoms and the presence of heteropolar bonds (e.g. C–B, C–N and B–N) also increases phonon scattering in this system. Therefore, in this work, we go beyond the nanostructuring strategy, and show the reduction of lattice thermal conductivity by multiple length-scale phonon scattering through hierarchical architecturing from atomic-scale point defects and disordered

nanodomains to mesoscale grain boundaries.[38,40] The lowest κ_{latt} is measured in the $(BN)_{0.45}(C)_{0.55}$ nanosheets, which is due to the high disorder present in $(BN)_{0.45}(C)_{0.55}$ among the various synthesized $(BN)_{1-x}(C)_x$ compositions.

5. Conclusions

In conclusion, few-layer BCN materials have been synthesized via solid state reaction employing urea, activated charcoal and boric acid as precursors. Temperature variation of electrical conductivity and Seebeck coefficient confirm *p*-type semiconducting behaviour of the materials. A detailed experimental investigation of the thermal conductivity of BCN with the variation of B, C, and N content has been carried out. The presence of different length-scale nano/meso hierarchical architectures like bonding heterogeneity (e.g. C–B, C–N and B–N), disordered BN/carbon nanodomains, grain boundaries and rich point defects related C/B/N disorder collectively scatter the heat carrying acoustic phonons, resulting in low thermal conductivity of the BCN nanosheets compared to that of h-BN or graphene. The low thermal conducting BCN nanosheets could be of value in thermal energy management.

6. References

(1) A. K. Geim, K. S. Novoselov, The rise of graphene, *Nat. Mater.*, (**2007**), *6* (3), 183–191.

(2) A. A. Balandin, S. Ghosh, W. Bao, I. Calizo, D. Teweldebrhan, F. Miao, C. N. Lau, Superior Thermal Conductivity of Single-Layer Graphene, *Nano Lett.*, **2008**, *8* (3), 902–907.

(3) K. S. Novoselov, Electric Field Effect in Atomically Thin Carbon Films, *Science (Washington, DC, U.S)*, **2004**, *306* (5696), 666–669.

(4) C. N. R. Rao, U. V Waghmare, 2D Inorganic Materials beyond Graphene,World Scientific, Singapore, 2016.

(5) L. Song, L. Ci, H. Lu, P. B. Sorokin, C. Jin, J. Ni, A. G. Kvashnin, D. G. Kvashnin, J. Lou, B. I. Yakobson, P. M. Ajayan, Large Scale Growth and Characterization of Atomic Hexagonal Boron Nitride Layers, *Nano Lett.*, **2010**, *10* (8), 3209–3215.

(6) M. Chhowalla, H. S. Shin, G. Eda, L. -J. Li, K. P. Loh, H. Zhang, The chemistry of two-dimensional layered transition metal dichalcogenide nanosheets, *Nat. Chem.*, **2013**, *5* (4), 263–275.

(7) N. kumar, K. Moses, K. Pramoda, S. N. Shirodkar, A. K. Mishra, U. V. Waghmare, A. Sundaresan, C. N. R. Rao, Borocarbonitrides, $B_xC_yN_z$, *J. Mater. Chem. A.*, **2013**, *1* (19), 5806-5821.

(8) C. N. R. Rao, K. Pramoda, Borocarbonitrides, $B_xC_yN_z$, 2D Nanocomposites with Novel Properties, *Bull. Chem. Soc. Jpn.*, **2019**, *92* (2), 441–468.

(9) L. Ci, L. Song, C. Jin, D. Jariwala, D. Wu, Y. Li, A. Srivastava, Z. F. Wang, K. Storr, L. Balicas, F. Liu, P. M. Ajayan, Atomic layers of hybridized boron nitride and graphene domains, *Nat. Mater.*, **2010**, *9* (5), 430–435.

(10) L. S. Panchakarla, K. S. Subrahmanyam, S. K. Saha, A. Govindaraj, H. R. Krishnamurthy, U. V. Waghmare, C. N. R. Rao, Synthesis, Structure, and Properties of Boron- and Nitrogen-Doped Graphene, *Adv. Mater.*, **2009**, *21* (46), 4726-4730.

(11) C. N. R. Rao, K. Gopalakrishnan, Borocarbonitrides, $B_xC_yN_z$: Synthesis, Characterization, and Properties with Potential Applications, *ACS Appl. Mater. Interfaces.*, **2017**, *9* (23), 19478–19494.

(12) Y. Kubota, K. Watanabe, O. Tsuda, T. Taniguchi, Deep Ultraviolet Light-Emitting Hexagonal Boron Nitride Synthesized at Atmospheric Pressure, *Science (Washington, DC, U.S)*, **2007**, *317* (5840), 932–934.

(13) R. Attri, M. B. Sreedhara, C. N. R. Rao, Compositional Tuning of Electrical and

Optical Properties of PLD-Generated Thin Films of 2D Borocarbonitrides $(BN)_{1-x}(C)_x$, *ACS Appl. Electron. Mater.*, **2019**, *1* (4), 569–576.

(14) B. Muchharla, A. Pathak, Z. Liu, L. Song, T. Jayasekera, S. Kar, R. Vajtai, L. Balicas, P. M. Ajayan, S. Talapatra, N. Ali, Tunable Electronics in Large-Area Atomic Layers of Boron–Nitrogen–Carbon, *Nano Lett.*, **2013**, *13* (8), 3476–3481.

(15) A. K. Manna, S. K. Pati, Tunable electronic and magnetic properties in $B_xN_yC_z$ nanohybrids: Effect of domain segregation, *J. Phys. Chem. C.*, **2011**, *115* (21), 10842–10850.

(16) M. B. Sreedhara, K. Gopalakrishnan, B. Bharath, R. Kumar, G. U. Kulkarni, C. N. R. Rao, Properties of nanosheets of 2D-borocarbonitrides related to energy devices, transistors and other areas, *Chem. Phys. Lett.*, **2016**, *657*, 124–130.

(17) M. Chhetri, S. Maitra, H. Chakraborty, U. V. Waghmare, C. N. R. Rao, Superior performance of borocarbonitrides, $B_xC_yN_z$, as stable, low-cost metal-free electrocatalysts for the hydrogen evolution reaction, *Energy Environ. Sci.*, **2016**, *9* (1), 95–101.

(18) J. N. Coleman, M. Lotya, A. O'Neill, S. D. Bergin, P. J. King, U. Khan, K. Young, A. Gaucher, S. De, R. J. Smith, I. V. Shvets, S. K. Arora, G. Stanton, H. -Y. Kim, K. Lee, G. T. Kim, G. S. Duesberg, T. Hallam, J. J. Boland, J. J. Wang, J. F. Donegan, J. C. Grunlan, G. Moriarty, A. Shmeliov, R. J. Nicholls, J. M. Perkins, E. M. Grieveson, K. Theuwissen, D. W. McComb, P. D. Nellist, V. Nicolosi, Two-Dimensional Nanosheets Produced by Liquid Exfoliation of Layered Materials, *Science (Washington, DC, U.S)*, **2011**, *331* (6017), 568–571.

(19) A. Banik, K. Biswas, Synthetic Nanosheets of Natural van der Waals Heterostructures, *Angew. Chemie Int. Ed.*, **2017**, *56* (46), 14561–14566.

(20) M. S. Dresselhaus, G. Chen, M. Y. Tang, R. G. Yang, H. Lee, D. Z. Wang, Z. F. Ren, J. -P. Fleurial, P. Gogna, New Directions for Low-Dimensional Thermoelectric Materials, *Adv. Mater.*, **2007**, *19* (8), 1043–1053.

(21) G. Tan, L. -D. Zhao, M. G. Kanatzidis, Rationally Designing High-Performance Bulk Thermoelectric Materials, *Chem. Rev.*, **2016**, *116* (19), 12123–12149.

(22) M. K. Jana, K. Biswas, Crystalline Solids with Intrinsically Low Lattice Thermal Conductivity for Thermoelectric Energy Conversion, *ACS Energy Lett.*, **2018**, *3* (6), 1315–1324.

(23) L. -D. Zhao, S. -H. Lo, Y. Zhang, H. Sun, G. Tan, C. Uher, C. Wolverton, V. P. Dravid, M. G. Kanatzidis, Ultralow thermal conductivity and high thermoelectric figure of merit in SnSe crystals, *Nature.*, **2014**, *508* (7496), 373–377.

(24) H. Sevinçli, G. Cuniberti, Enhanced thermoelectric figure of merit in edge-disordered zigzag graphene nanoribbons, *Phys. Rev. B.*, **2010**, *81* (11), 113401.

(25) H. Chakraborty, S. Mogurampelly, V. K. Yadav, U. V. Waghmare, M. L. Klein, Phonons and thermal conducting properties of borocarbonitride (BCN) nanosheets, *Nanoscale.*, **2018**, *10* (47), 22148–22154.

(26) C. Lin, X. Zhang, Z. Rao, Theoretical prediction of thermal transport in BC_2N monolayer, *Nano Energy.*, **2017**, *38*, 249–256.

(27) Y. -Y. Zhang, Q. -X. Pei, H. -Y. Liu, N. Wei, Thermal conductivity of a h-BCN monolayer, *Phys. Chem. Chem. Phys.*, **2017**, *19* (40), 27326–27331.

(28) C. Gautam, C. S. Tiwary, S. Jose, G. Brunetto, S. Ozden, S. Vinod, P. Raghavan, S. Biradar, D. S. Galvao, P. M. Ajayan, Synthesis of Low-Density, Carbon-Doped, Porous Hexagonal Boron Nitride Solids, *ACS Nano.*, **2015**, *9* (12), 12088–12095.

(29) K. Raidongia, A. Nag, K. P. S. S. Hembram, U. V. Waghmare, R. Datta, C. N. R. Rao, BCN: A Graphene Analogue with Remarkable Adsorptive Properties, *Chem. - A Eur. J.*, **2010**, 16 (1), 149–157.

(30) J. -X. Xue, J. -X. Liu, B. -H. Xie, G. -J. Zhang, Pressure-induced preferential grain growth, texture development and anisotropic properties of hot pressed hexagonal boron nitride ceramics, *Scr. Mater.*, **2011**, *65* (11), 966–969.

(31) A. C. Ferrari, D. M. Basko, Raman spectroscopy as a versatile tool for studying the properties of graphene, *Nat. Nanotechnol.*, **2013**, *8* (4), 235–246.

(32) J. -B. Wu, M. -L. Lin, X. Cong, H. -N. Liu, P. -H. Tan, Raman spectroscopy of graphene-based materials and its applications in related devices, *Chem. Soc. Rev.*, **2018**, *47* (5), 1822–1873.

(33) R. Kumar, K. Gopalakrishnan, I. Ahmad, C. N. R. Rao, BN-Graphene Composites Generated by Covalent Cross-Linking with Organic Linkers, *Adv. Funct. Mater.*, **2015**, *25* (37), 5910–5917.

(34) Y. Gong, G. Shi, Z. Zhang, W. Zhou, J. Jung, W. Gao, L. Ma, Y. Yang, S. Yang, G. You, R. Vajtai, Q. Xu, A. H. MacDonald, B. I. Yakobson, J. Lou, Z. Liu, P. M. Ajayan, Direct chemical conversion of graphene to boron- and nitrogen- and carbon-containing atomic layers, *Nat. Commun.*, **2014**, *5* (1), 3193.

(35) M. Barua, M. B. Sreedhara, K. Pramoda, C. N. R. Rao, Quantification of surface functionalities on graphene, boron nitride and borocarbonitrides by fluorescence labeling, *Chem. Phys. Lett.*, **2017**, *683*, 459–466.

(36) J. Jin, F. Pan, L. Jiang, X. Fu, A. Liang, Z. Wei, J. Zhang, G. Sun, Catalyst-Free Synthesis of Crumpled Boron and Nitrogen Co-Doped Graphite Layers with Tunable Bond Structure for Oxygen Reduction Reaction, *ACS Nano*., **2014**, *8* (4), 3313–3321.

(37) K. Biswas, J. He, Q. Zhang, G. Wang, C. Uher, V. P. Dravid, M. G. Kanatzidis, Strained endotaxial nanostructures with high thermoelectric figure of merit, *Nat. Chem.*, **2011**, *3* (), 160-166.

(38) K. Biswas, J. He, I. D. Blum, C. I. Wu, T. P. Hogan, D. N. Seidman, V. P. Dravid, M. G. Kanatzidis, High-performance bulk thermoelectrics with all-scale hierarchical architectures, *Nature*, **2012**, *489* (), 414-418.

(39) B. Poudel, Q. Hao, Y. Ma, Y. Lan, A. Minnich, B. Yu, X. Yan, D. Wang, A. Muto, D. Vashaee, X. Chen, J. Liu, M. S. Dresselhaus, G. Chen, Z. Ren, High-thermoelectric performance of nanostructured bismuth antimony telluride bulk alloys, *Science (Washington, DC, U.S)*, **2008**, *320* (), 634-638.

[40] L. D. Zhao, V. P. Dravid, M. G. Kanatzidis, The panoscopic approach to high performance thermoelectrics, *Energy Environ. Sci.*, **2014**, *7* (), 251-268.

Part II

Atomic Layer Deposition (ALD) of Ultrathin Films of NiO

Chapter II.1

Crystalline Epitaxial Ultrathin Films of NiO Generated by Plasma Enhanced- Atomic Layer Deposition (PE-ALD)

Summary*

Plasma enhanced - atomic layer deposition (PE-ALD) technique is widely employed due to the high crystallinity at low temperatures and conformal coating of thin films of materials obtained by this method. Nickel oxide is one of the most studied transition metal oxides. Epitaxial thin films of NiO with preferred growth direction and less defects are of interest because of their integration in complex devices. We have deposited crystalline epitaxial thin films of NiO by PEALD and characterized them by X-Ray diffraction as well as various microscopic and spectroscopic techniques. Interestingly, the deposited NiO thin films show epitaxial growth of (111) plane along the (0006) plane of c-sapphire at all growth temperatures (200 – 260 ^{O}C). The deposited NiO films have smooth surface with R.M.S. roughness of 0.18 nm. The spectroscopic analysis confirms nearly stoichiometric NiO with 3.8 eV bandgap and the presence hydroxyl bonds at the surface. The study of growth behaviour of epitaxial NiO thin films by PEALD is of fundamental interest for the development of the field.

***** Manuscript under Preparation

1. Introduction

Atomic layer deposition (ALD) has emerged as a highly useful and powerful technique for conformal coating of high-quality materials with atomic level precision. ALD offers advantages over other deposition techniques such as, high crystallinity at low temperatures, monolayer thickness control due to self-limiting reactions, chemical selectivity, highly conformal and uniform films on complex substrates.[1–4] Plasma-enhanced atomic layer deposition (PEALD) is an improvement over the thermal process, as it supplies high energetic free radicals species of non-metal co-reactant. In PEALD, surface reactions are not limited by the activation energy provided by the substrate temperature and is useful to explore new materials.[5] In ALD as well as PEALD, reactants are supplied alternatively into the reactor to avoid homogeneous gas phase nucleation. We have investigated ALD of films of nickel oxide (NiO), which has interesting properties of use in catalysis,[6] energy storage and conversion,[7,8] opto- and nano-electronics.[9,10] NiO is an antiferromagnetic insulator which crystallizes in the rock salt structure ($Fm\bar{3}m$) and well-known for its optical,[11] electrical,[12] and magnetic properties.[13] NiO is a p-type wide bandgap semiconductor with high chemical stability and optical transparency. There have been attempts to prepare ultrathin films of NiO by ALD by using metal organic nickel precursors such as $Ni(MeCp)_2$, $Ni(dmamp)_2$, $Ni(dmamb)_2$, $Ni(thd)_2$, $Ni(Cp)_2$ and $Ni(acac)_2$. Cyclopentadienyl type precursors have generally yielded amorphous[14] or polycrystalline NiO films.[10,15,16] Some of the preparations have also resulted in sub-stoichiometric NiO films.[17] 1-Dimethylamino-2-methyl-2-butanolate (dmamb) and related precursors generally yield amorphous films[9,18] or cubic polycrystalline films with randomly oriented crystallites.[19] Local

epitaxy has been found in the case of methylcyclopentadienyl (MeCp) precursor (on platinum (Pt) substrate).[20]

High crystalline epitaxial films on heterogeneous (or complex) substrates are preferred for many application due to the presence of less defects, sharp interfaces and preferred growth orientation.[21] Therefore, it is necessary to grow highly crystalline epitaxial conformal thin films with selective phase without post-deposition annealing. Stoichiometry, crystallinity, and phase selectivity of the NiO films grown by thermal ALD/PEALD pose problems. The choice of the precursor is also an important aspect in ALD because the film morphology, structure, and quality are determined by the precursor.[22] Considering these problems, we have carried out thin film deposition of NiO using a cost-effective and readily available nickel acetylacetonate [$Ni(acac)_2$] as the nickel precursor and studied the film growth behavior and characteristics.

We present results of our investigations of the epitaxial films of NiO deposited on (0001) oriented c-sapphire using sequential exposures of [$Ni(acac)_2$] and O_2 plasma. The NiO films were grown over the temperature range of 200 ^{O}C - 260 ^{O}C with a fairly slow growth rate of ~0.05 nm/ cycles. The growth characteristics of high quality epitaxial NiO films by plasma enhanced ALD have been examined in some detail. The films have been characterized by X-Ray diffraction as well as microscopic and spectroscopic techniques.

2. Scope of the present investigations

ALD technique has been widely used for depositing high crystalline materials with atomic layer precision, and high conformality on complex substrates. ALD offers different modes for conformal coating of materials i.e. thermal and plasma enhanced ALD, out of which PEALD yields high crystalline thin films. We have chosen to study ultrathin films of NiO which occupies a unique place in the physics of transition metal oxides. We felt that, it was desirable to deposit crystalline epitaxial thin films of NiO on different substrates, since nanometer thick films of NiO by ALD could be of use to study the atomic scale growth behaviour and for integration of NiO in complex devices architectures. The present study sheds light on the use of a simple Ni compound, nickel acetylacetonate [$Ni(acac)_2$] for deposition of epitaxial NiO films. The films deposited by 1000 PEALD cycles have been characterized by XRD, microscopic and spectroscopic techniques.

3. Experimental Section

Atomic Layer deposition of thin films

The epitaxial thin films of nickel oxide (NiO) were grown on single crystalline α-Al_2O_3 (0001) substrates using a flow type ALD reactor equipped with shower head plasma setup (Beneq, TFS 200 Finland Oy). Polycrystalline films of NiO were obtained on commercially purchased p-type Si(100), SiO_2/Si(100) and soda lime glass substrates, respectively. High purity nickel acetylacetonate ($Ni(acac)_2$, Sigma Adrich, 95%) was used as the nickel source, while oxygen (O_2) (Chemix, 99.9995%) was used for the O_2 plasma, respectively. Before the deposition, the sapphire substrates were cleaned using

piranha cleaning process and washed several times by de-ionised water to remove contaminants. Si(100) substrates were cleaned by HF to remove the native oxide layer prior to deposition. All the substrates were also cleaned by ultrasonication in acetone and isopropanol and dried under N_2. High purity nitrogen (Chemix, 99.9995%) was used as a carrier as well as purging gas throughout the deposition. Before starting the deposition, the reactor and the chamber pressure was maintained at 1 mbar and 10 mbar, respectively. The reactor pressure varied between 1-3 mbar during the pulsing of precursors while the chamber pressure remains unchanged.

Ultrathin NiO films were prepared by plasma enhanced atomic layer deposition (PEALD) over the temperature range of 200 - 260 ^{O}C (**Scheme 1**). The PEALD process consists of sequential pulsing of $Ni(acac)_2$ and O_2 plasma as nickel and oxygen source, respectively. The O_2 plasma was generated from Advanced Energy Cesar RF power generator equipped with automatic matching unit, controlled at 100 W forward plasma power. Oxygen to the plasma shower head was controlled by a mass flow controller (MKS Instruments) allowing 100 sccm of gas during the deposition. $Ni(acac)_2$ was kept in the hot source HS-300 bubbler (Beneq, Oy) which was slowly heated to 180 ^{O}C. The optimised pulsing and purging times for a typical PEALD cycle were $Ni(acac)_2$ (4s)/ N_2 purge (4s)/ O_2 plasma (10s)/ N_2 purge (4s). The pulsing time for $Ni(acac)_2$ and O_2 plasma was adequate to saturate the growth per cycle, enough purging time being given to remove the excess precursor after each half reaction. The deposited films were allowed to cool down to room temperature under ambient conditions and characterized without any post annealing. The growth characteristics of NiO films were studied by depositing films at different growth temperatures by 1000 PEALD cycles.

Characterization of thin films

The thermal stability of $Ni(acac)_2$ precursor for ALD was investigated in the range of 30-700 ^{O}C under inert atmosphere using Mettler Toledo TGA-850 TG analyser. The growth per cycle (GPC) was calculated by dividing the measured thickness with the number of cycles. Thin film thickness (in cross-section) and surface morphology were determined using Nova NanoSEM 600 FESEM (FEI) operated at 15 kV accelerating voltage. Grazing incidence X-Ray diffraction (GIXRD) patterns of the as-deposited films were recorded with a Panalytical diffractometer (Empyrean) having monochromatic Cu $K\alpha_1$ radiation (λ = 1.5404Å). High-resolution XRD patterns (θ-2θ and omega scans) were recorded with a Bruker D8 Discover instrument.

X-ray photoelectron spectroscopy (XPS) measurements were made with an Omicron nanotechnology spectrometer with Al-Kα as a monochromatic X-ray source ($h\upsilon$ = 1486.7 eV) operated at 300 W. All the spectra were acquired with a take-off angle of 54.7^{O} with respect to the sample surface. The peak fitting (Voigt function) along with Shirley background subtraction was performed using Fityk 1.3.1. We avoided sputter cleaning in order not to affect the oxidation state of elements.[23] Chemical compositions of the films were estimated from the high-resolution XP spectra, and with energy dispersive X-Ray spectroscopy (EDX). Chemical compositions from XPS were calculated by dividing the integrated peak intensities of Ni 2p and O 1s of NiO, respectively by atomic sensitivity factor (ASF) of the respective element.

Raman spectra was recorded with a Jobin Yvon LabRam HR 800 spectrometer in the backscattering geometry using a 514.5 nm laser. The surface topography and the root mean square roughness (R_{RMS}) of the films (1 μm × 1 μm area) were determined using atomic force microscopy (AFM) from a Bruker Innova instrument in tapping mode using high-resolution RTESPA-300 Bruker AFM probe having tip radius of 10 nm. Optical bandgaps of NiO films were calculated using the spectra obtained with a Perkin−Elmer Lambda 750 UV−vis spectrometer in the transmission mode.

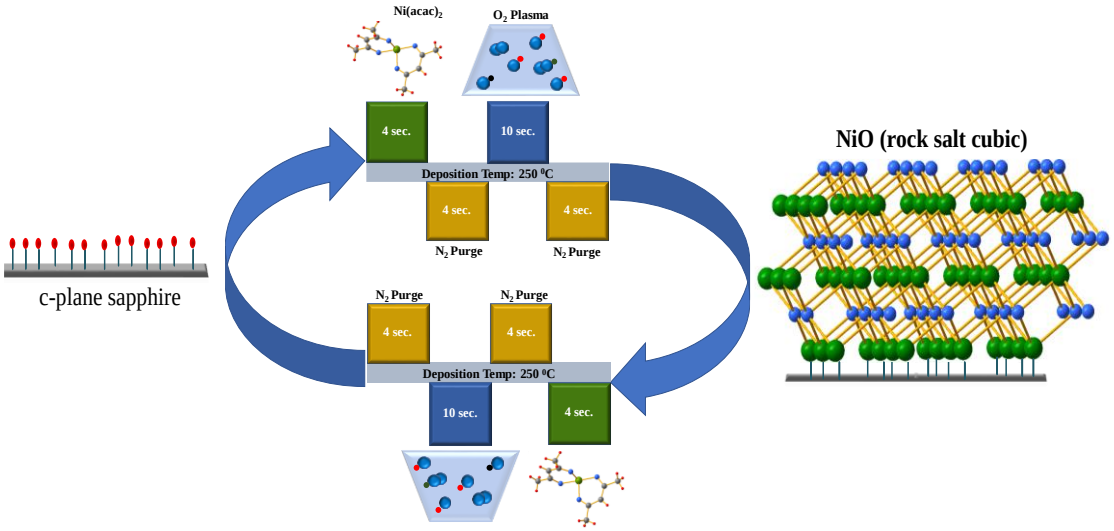

Scheme 1: Schematic representation of PEALD process representing two PEALD cycles showing pulsing of $Ni(acac)_2$ and O_2 plasma followed by purging of N_2 leading to the growth of rock salt cubic NiO films on c-plane sapphire.

4. Results and discussion

High crystalline epitaxial thin films of NiO could be deposited on c-plane sapphire by sequential exposure of [$Ni(acac)_2$] as the nickel precursor and O_2 plasma as the oxygen source. Homogeneous and uniform films of NiO were obtained by alternate

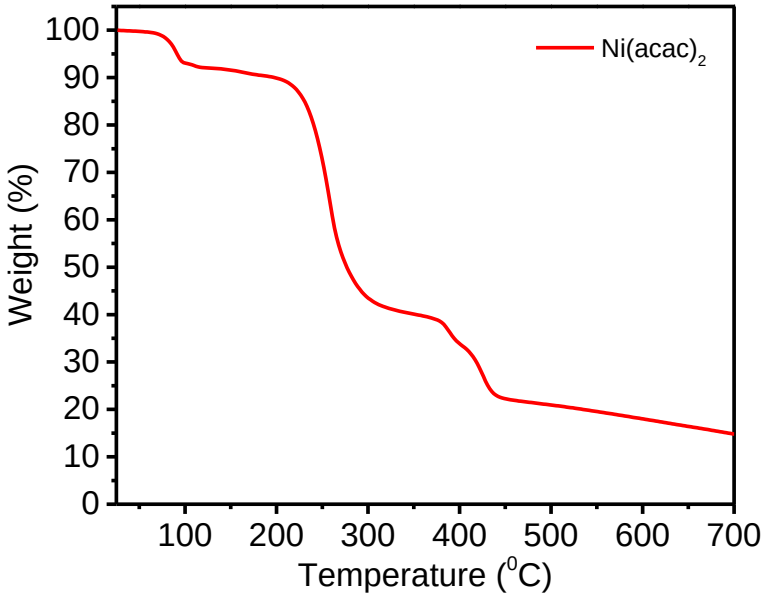

Figure 1: Thermogravimetric curve showing weight loss of $Ni(acac)_2$ in inert atmosphere.

self-terminating surface reactions between precursors. The films deposited by 1000 PEALD cycles have been characterized by microscopic and spectroscopic techniques. The process (**Scheme 1**) shows the reaction of free radicals of oxygen in the plasma with the $Ni(acac)_2$ molecules chemisorbed on the surface of substrate. The excess precursors were taken out by purging high flow of nitrogen. For a typical ALD process, the thermal property of precursor plays vital role as it should not decompose at the ALD process temperature. **Figure 1** shows the thermogravimetric (TG) curve of $Ni(acac)_2$ from 30 ^{O}C to 700 ^{O}C performed in inert atmosphere. Initial weight loss below 110 ^{O}C is due to removal of adsorbed moisture because of the hygroscopic nature of $Ni(acac)_2$. The TG curve shows the three-step weight loss by leaving 15% residual weight at 700 ^{O}C. In ALD, the deposition temperature is preferable less than the temperature of 50% precursor's weight loss (T_{50}) in TG curve in order to avoid decomposition.[24] It should be noted $Ni(acac)_2$ is stable at the temperature at which ALD was carried out (< 275 ^{O}C).

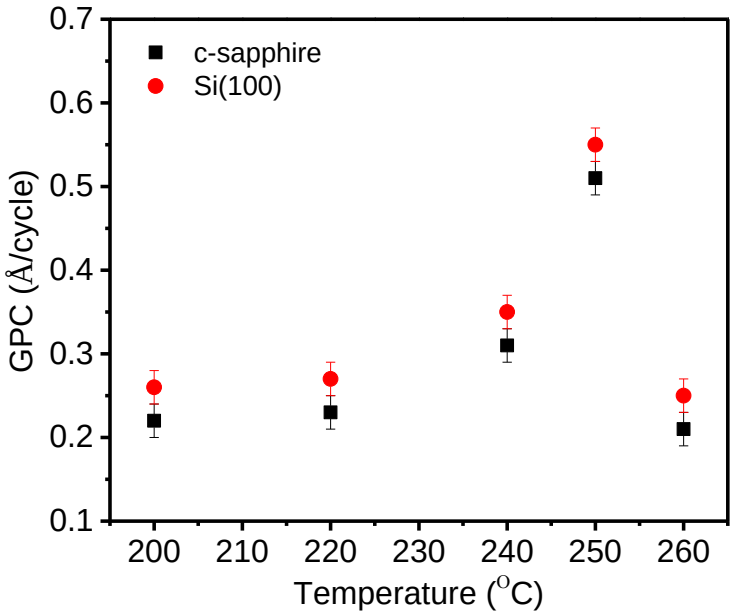

Figure 2: Cross-section FESEM established results of PEALD process window of NiO on c-sapphire and Si(100) showing growth rate per cycle (GPC) as a function of substrate temperature. (Error bars indicate the standard deviation of measured thickness within the detection limit of FESEM)

The typical self-limiting and saturating nature of the ALD process is defined in specific temperature range which is obtained by plotting growth per cycle (GPC in Å/cycle) against the deposition temperature. In **Figure 2** we show the GPC as a function of deposition temperature on Si(100) and c-plane sapphire. The GPC is calculated using the thickness of the deposited films by 1000 PEALD cycles. The cross-section images of NiO films deposited at different substrate temperatures are shown in **Figure 3 and Figure 4.** The growth rate on c-Al_2O_3 increased slowly from ~ 0.22 Å/cycle to ~ 0.31 Å/cycle in the temperature range of 200 ^{O}C to 240 ^{O}C and then rapidly reached to ~ 0.51 Å/cycle at 250 ^{O}C. Above 250 ^{O}C, the decrease in GPC could be caused by the precursor desorption at the surface. Non ideal ALD growth rate per cycle was also observed by Lindahl et. al in the case of NiO films observed by $Ni(thd)_2$ and water (H_2O).[25] The growth rate of ~0.51 Å/cycle at 250 ^{O}C is comparable to that by

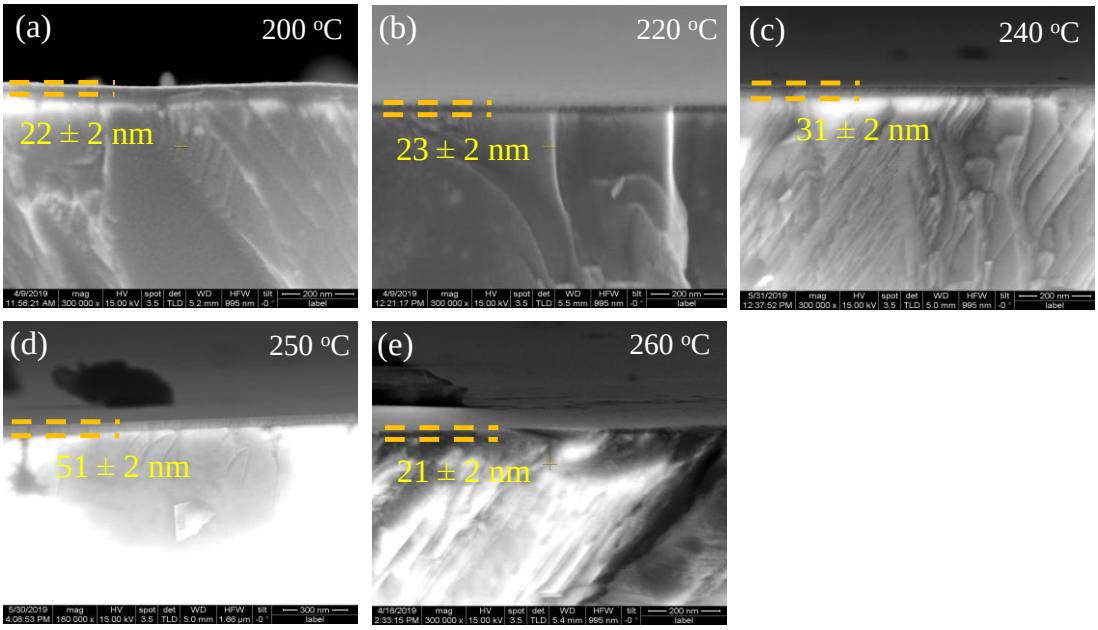

Figure 3: Cross-section FESEM images of NiO film deposited on c-plane sapphire substrate by 1000 PEALD cycles at (a) 200 ^{O}C, (b) 220 ^{O}C, (c) 240 ^{O}C, (d) 250 ^{O}C, and (e) 260 ^{O}C, respectively.

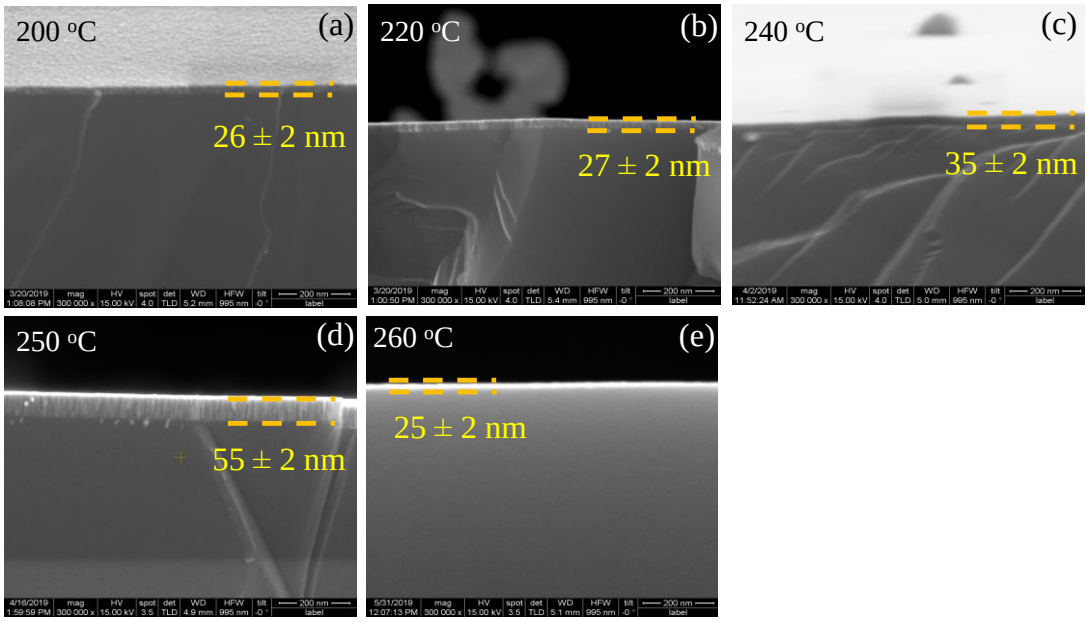

Figure 4: Cross-section FESEM images of NiO film deposited on Si(100) substrate by 1000 PEALD cycles at (a) 200 ^{O}C, (b) 220 ^{O}C, (c) 240 ^{O}C, (d) 250 ^{O}C, and (e) 260 ^{O}C, respectively.

Song et. al on platinum (Pt) substrate using PEALD.[20] High growth rate on Si(100) substrate as compared to c-sapphire is considered to be related to the adsorption sites available on the growing crystallographic planes of NiO. Among (100), (110), and (111) type of planes of NiO, (111) planes possess highest chemical adsorption sites for the precursor molecule.[20] For polycrystalline growth on silicon, crystallographic planes like (111), (200), (220), (311) of NiO will all be available for chemisorption, resulting in high GPC. The reaction mechanism for the growth of NiO would be similar to that proposed by Kessels and co-workers for the growth of metal oxides using plasma as a co-reactant.[26]

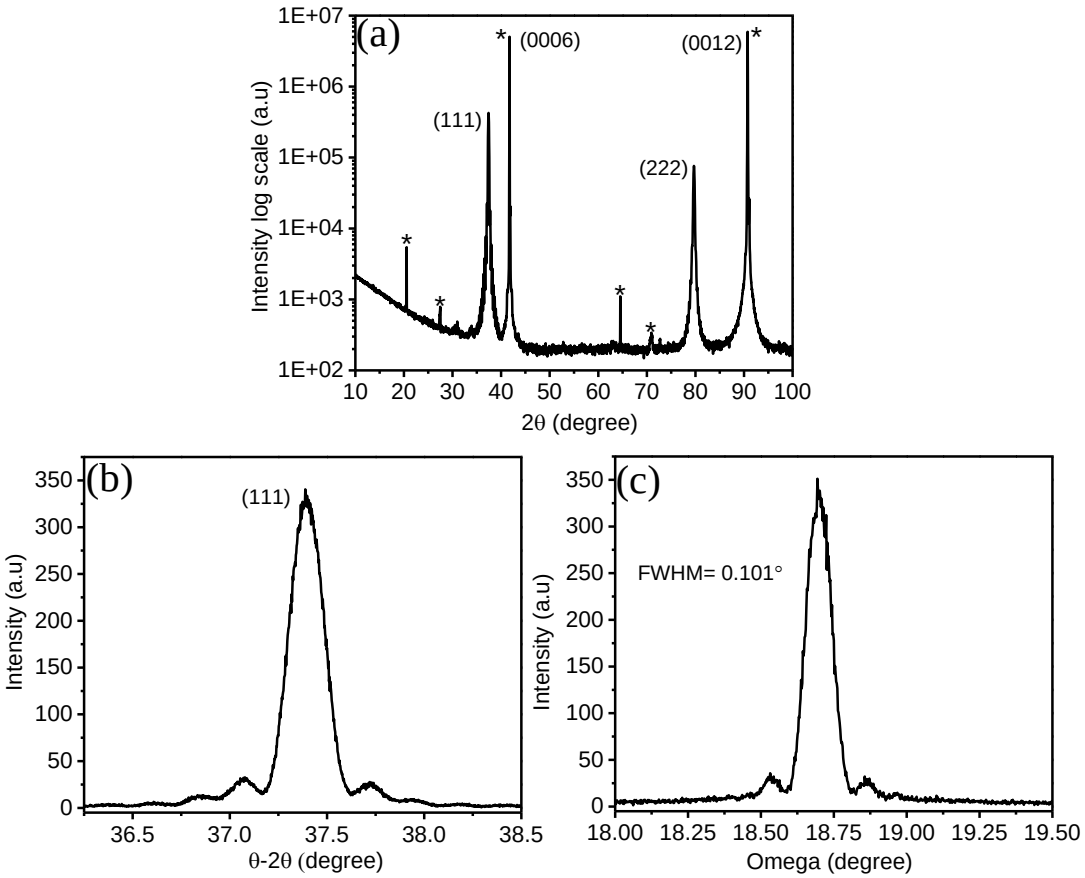

Figure 5: (a) GIXRD pattern, (b) long scan HRXRD pattern of (111) plane, and (c) rocking curve scan, of NiO thin film grown on c-plane sapphire at 250 ^{O}C reactor temperature by 1000 PEALD cycles. (* denotes the substrate/holder peaks)

The crystalline nature of epitaxial NiO films was examined by XRD patterns. High quality crystalline films of NiO were obtained without post deposition annealing as compare to other ALD grown films reported in the literature.[18,19,22] The long duration θ-2θ scan (**Figure 5(a)**) of as deposited NiO film by 1000 PEALD cycles at 250 ^{O}C shows (111) plane of NiO preferentially oriented along (0006) plane of c-sapphire. The occurrence of the second order diffraction peak in the XRD pattern also confirms the epitaxial nature of NiO thin films. **Figure 5(b)** shows the long duration high resolution θ-2θ scan of (111) plane of NiO deposited at 250 ^{O}C by 1000 PEALD cycles showing the diffraction peak at 2θ ~ 37.3781^{O} corresponding to the rock salt structure of NiO.

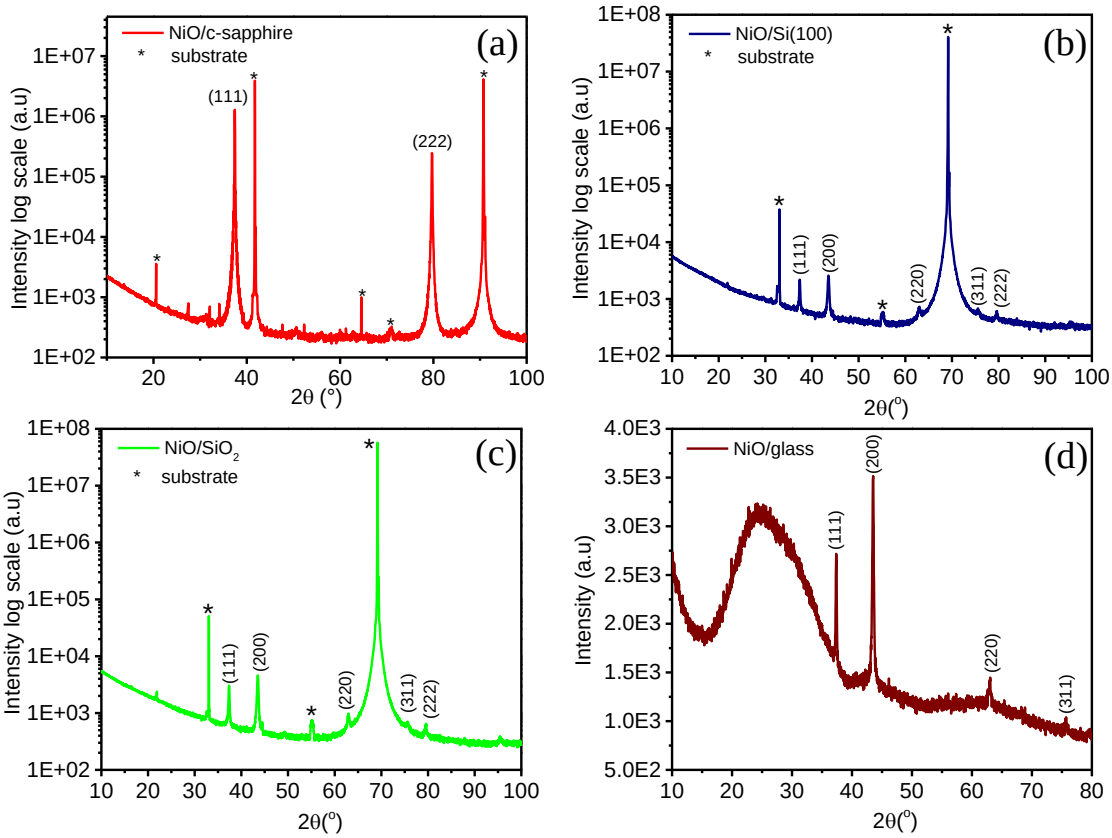

Figure 6: GIXRD pattern of NiO film deposited at 250 ^{O}C by 2000 PEALD cycles on (a) c-plane sapphire, (b) Si (100), (c) SiO_2/Si(100), and (d) soda lime glass substrate, respectively.

The lattice constant calculated using 2θ value of (111) plane of NiO comes out to be ~ 4.1637 Å which shows the effect of compressive strain on the NiO unit cell as compared to the bulk (4.176 Å). The full width half maxima (FWHM) calculated from rocking curve scan (or ω scan) in **Figure 5(c)** is 0.101^{O} which confirms the excellent crystallinity of NiO films on c-sapphire. In order to compensate the large lattice mismatch between NiO and sapphire, the NiO film grows along the (111) plane because it possesses lowest strain energy. As explained by Kang et. al, if the preferred orientation is (111) of NiO, the transport of the precursors to the substrate surface from the gas/plasma phase controls the deposition rate.[27] **Figure 6(a)** shows the increase in intensity and decrease in FWHM of the (111) reflection of NiO film deposited at 250 ^{O}C on c-sapphire by 2000 PEALD cycles indicates long range grain ordering in the

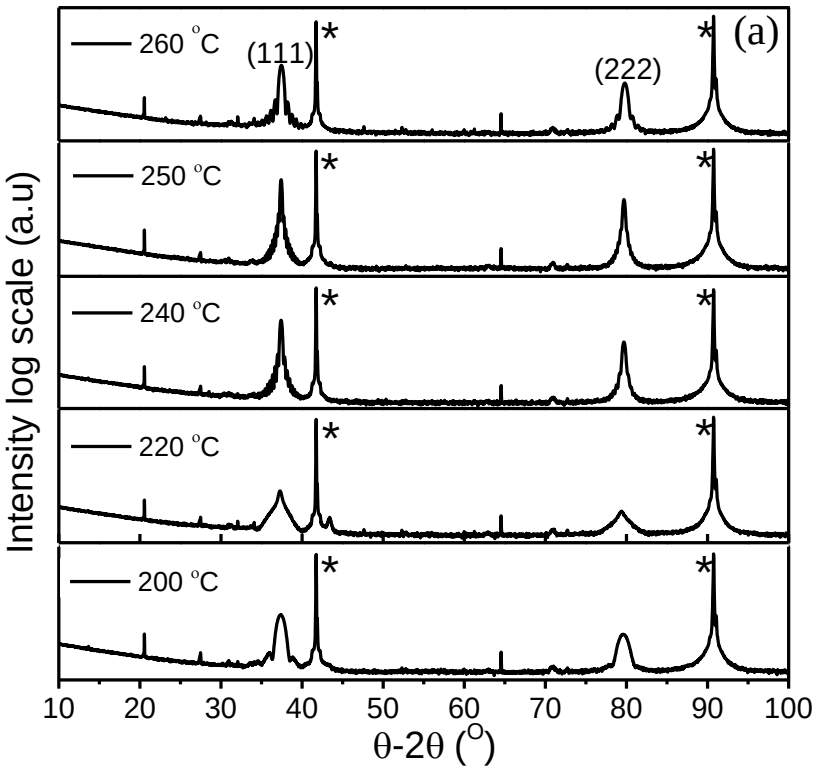

Figure 7: GIXRD pattern of NiO thin films deposited on c-plane sapphire by 1000 PEALD cycles as a function of deposition temperature. (* denotes the substrate peaks)

preferred direction. However, polycrystalline growth of NiO thin films (see **Figure 6(b-d)**) was observed on Si(100), SiO_2/Si(100), and soda lime substrates, respectively. The GIXRD pattern of NiO deposited on Si(100) also show peaks corresponding to SiO_2 which is caused by slight oxidation of the silicon surface by high energetic oxygen plasma flux. The epitaxial relationship derived from the GIXRD patterns is <111> NiO // <0001> Al_2O_3.

Figure 7 show the XRD patterns of NiO thin films as a function of substrate temperature. From the GIXRD profile, it is clearly visible that the cubic NiO (111) and (222) peaks are present irrespective of the deposition temperature (200 – 260 ^{O}C) which indicates the epitaxial growth of NiO on c-sapphire at all substrate temperatures. We observed a decrease in FWHM value of the (111) peak with increase in growth

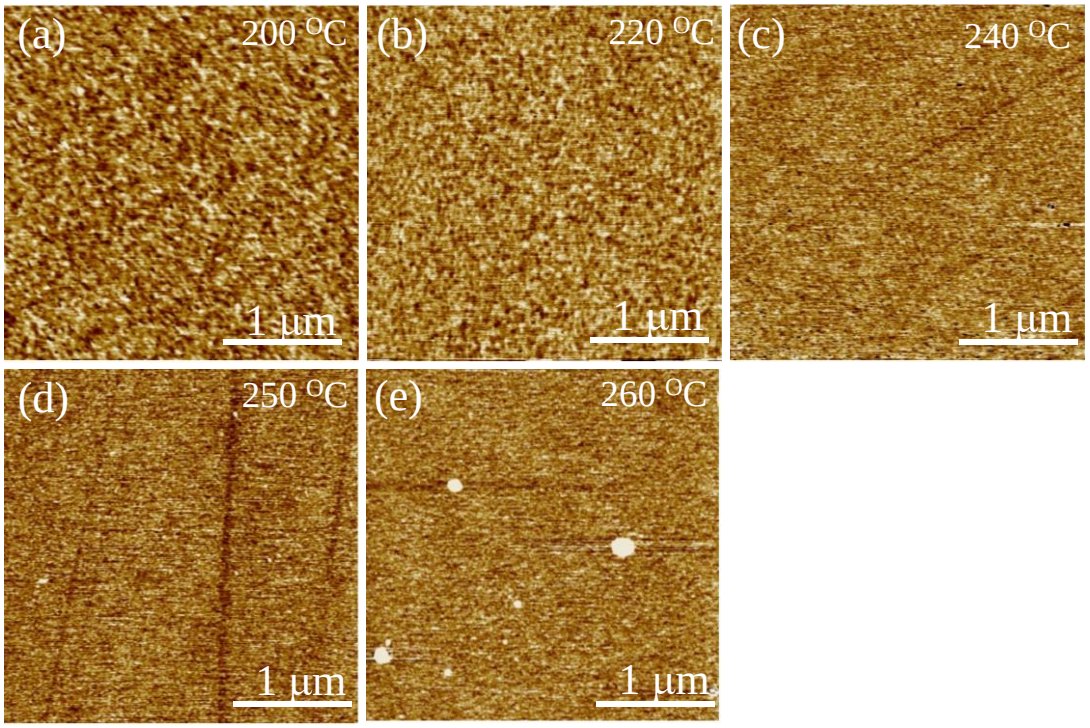

Figure 8: Topographic AFM images (3×3 um^2 area) of NiO films on c-plane sapphire deposited by 1000 PEALD cycles with respect to substrate temperature at (a) 200 ^{O}C, (b) 220 ^{O}C, (c) 240 ^{O}C, (d) 250 ^{O}C, and (e) 260 ^{O}C, respectively.

temperature showing improvement in crystallinity, and also long range ordering in preferred direction. These results are in consistent with the results from FESEM and AFM studies. Beyond 250 ^{O}C, increase in FWHM can be due to several factors like residual stress-strain, defect density and the reduction of film thickness/growth rate because of partial decomposition of precursor.[28,29]

Surface morphology and grain density of the films were studied by FESEM and AFM images. **Figure 8** (lower magnification AFM images) & **Figure 9** (higher magnification FESEM and AFM images) shows the in-plane FESEM and AFM images of NiO thin films grown on c-sapphire by 1000 PEALD cycles at different substrate temperature. Lower magnification topographic AFM images (**Figure 8**) show uniform films with flat and planar surface at all depositing temperatures. At higher magnification, FESEM images (**Figure 9(a-e)**) as well as AFM images (**Figure 9(f-j)**) show the evolution of small grains forming big grains. At 220 ^{O}C the size and the density of grains increases significantly. As the growth temperature is increased to 240 ^{O}C or 250 ^{O}C, the small grains coalesce and form large grains with columnar morphology of the thin films. **Figure 10** shows the variation of root mean square roughness (R_{RMS}) of NiO films with the substrate temperature. The R_{RMS} decreases from 0.268 nm at 200 ^{O}C to 0.180 nm at 250 ^{O}C. We also see some holes in the films which possibly due to pin-hole defects generally present in strained epitaxial films on heterogeneous substrates.[17] Surface FESEM images (**Figure 11**) show the number density of the pin hole defects to decrease when the substrate temperature is increased from 200 ^{O}C to 250 ^{O}C. The results signify a relationship between the increase in grain density and size along with the reduction of pin hole defects with the increase in crystallinity of the NiO films. At 260 ^{O}C, we observe a large number of holes as well as agglomerates in the film.

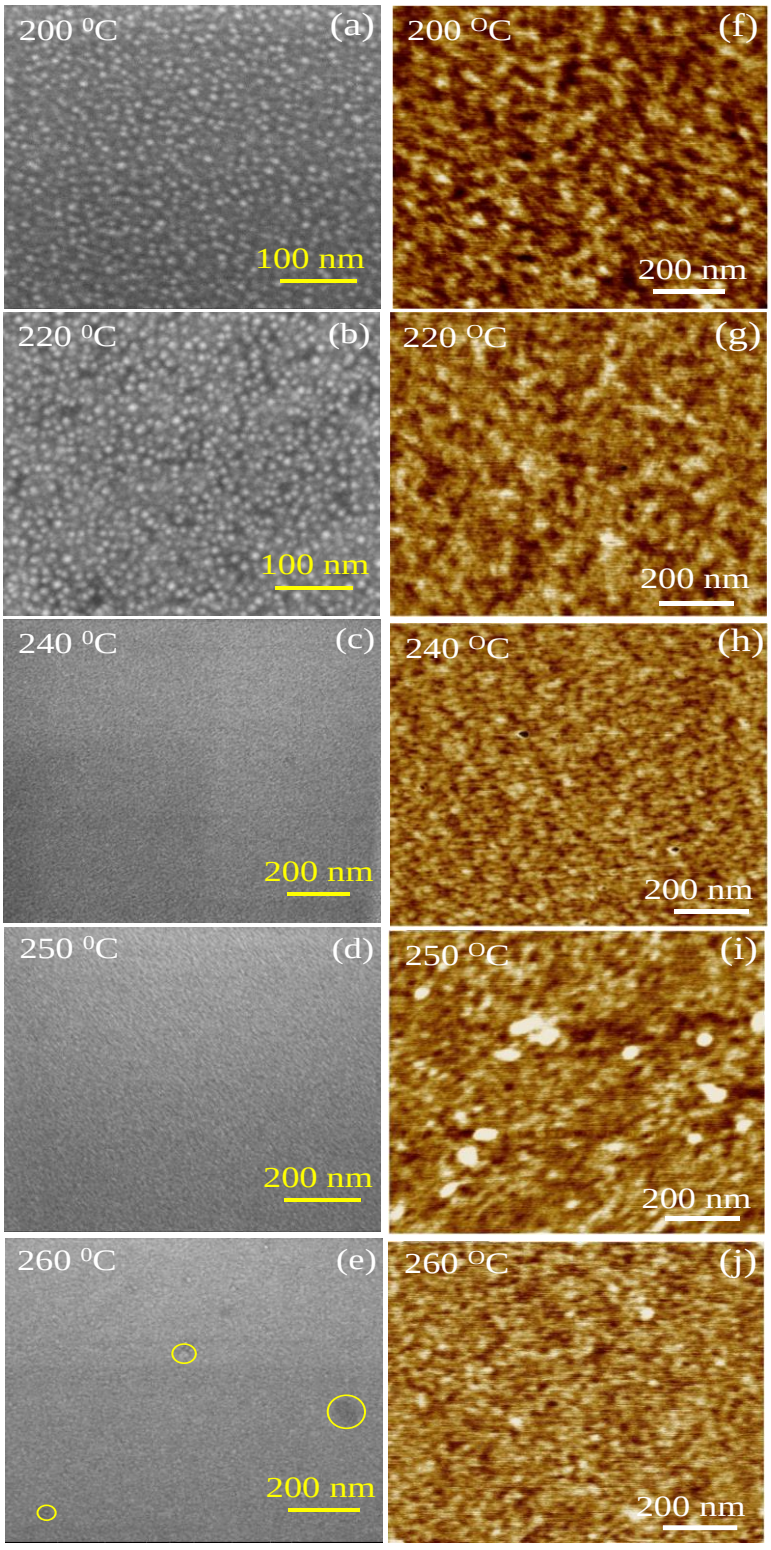

Figure 9: Microscopic based results: (a-e) FESEM images, (f-j) AFM images of epitaxial NiO films grown on c-plane sapphire by 1000 PEALD cycles showing variation in density of grains with respect to substrate temperature at (a,f) 200 ^{O}C, (b,g) 220 ^{O}C, (c,h) 240 ^{O}C, (d,i) 250 ^{O}C, and (e,j) 260 ^{O}C (circle denotes the agglomerates), respectively.

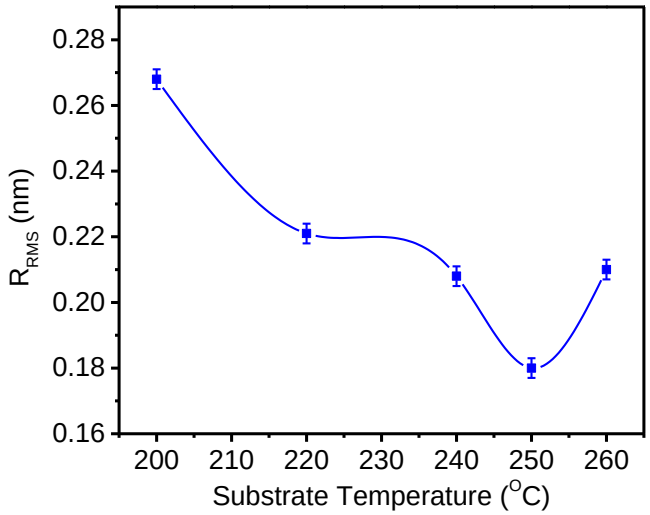

Figure 10: R_{RMS} calculated from 3×3 um^2 area as a function of substrate temperature of NiO films deposited on c-plane sapphire by 1000 PEALD cycles.

Figure 12 shows the room temperature Raman spectrum of the NiO films deposited on c-plane of sapphire by 1000 PEALD cycles at 250 ^{O}C growth temperature. The band due to one phonon transverse optical mode and longitudinal optical mode [1P

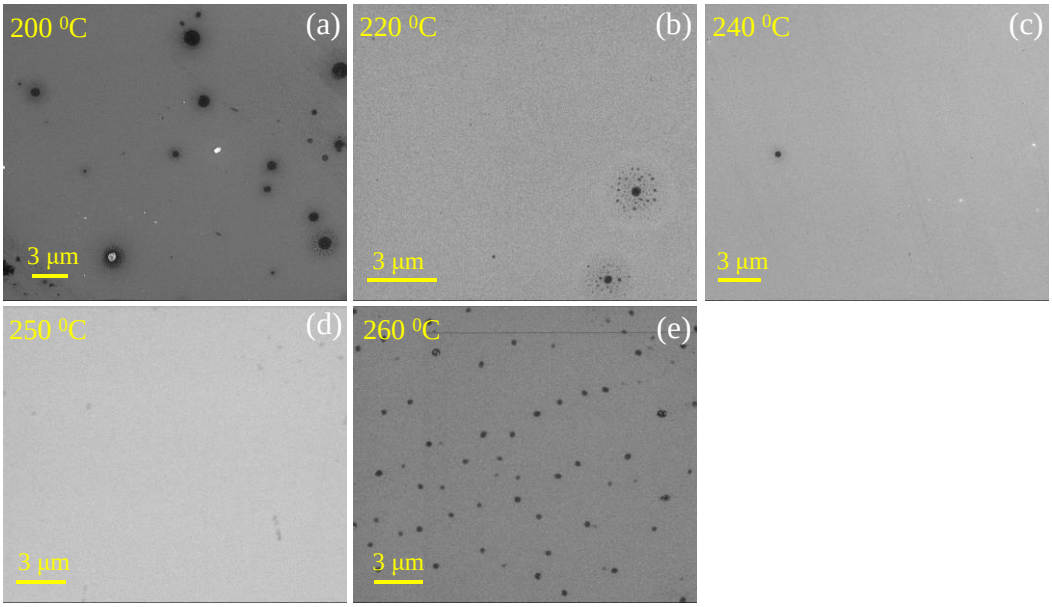

Figure 11: FESEM images showing variation in density of pin-hole defects in NiO films on c-plane sapphire deposited by 1000 PEALD cycles with respect to substrate temperature at (a) 200 ^{O}C, (b) 220 ^{O}C, (c) 240 ^{O}C, (d) 250 ^{O}C, and (e) 260 ^{O}C, respectively.

(TO + LO)] occurs at 512 cm^{-1} which corresponds to the Ni-O bond stretching mode.[30,31] The LO mode generally comes due to disorder induced defects or Ni-OH bonds at the film surface (see XPS studies). The observation of only the (LO + TO) phonon mode is probably because of small film thickness (~ 50 nm) as mentioned in other reports.[32] This could also be due to crystallographic orientation.[30]

X-ray photoelectron (XP) spectroscopy was employed to probe the chemical bonding, oxidation state of element, and chemical composition of epitaxial NiO thin films deposited by 1000 PEALD cycles on c-Al_2O_3 at 250 ^{O}C. The XP survey-scan spectrum (1100 - 0 eV) in **Figure 13(a)** shows the presence of nickel, oxygen and carbon elements in atomic layer deposited NiO thin films. The signal at 284.6 eV is due to carbon (1s) arising from surface adsorbed atmospheric contamination. The interpretation of electronic structure of transition metal, their oxides or hydroxides by XPS analysis is usually complicated owing to their 2p spectra because of complex

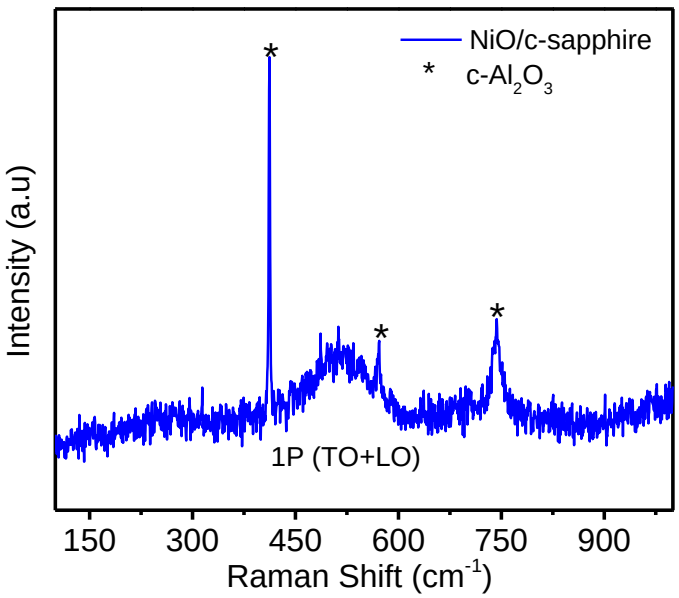

Figure 12: Room-temperature Raman spectra of NiO film grown at 250 ^{O}C on c-plane sapphire by 1000 PEALD cycles, respectively (* denotes the sapphire substrate peaks).

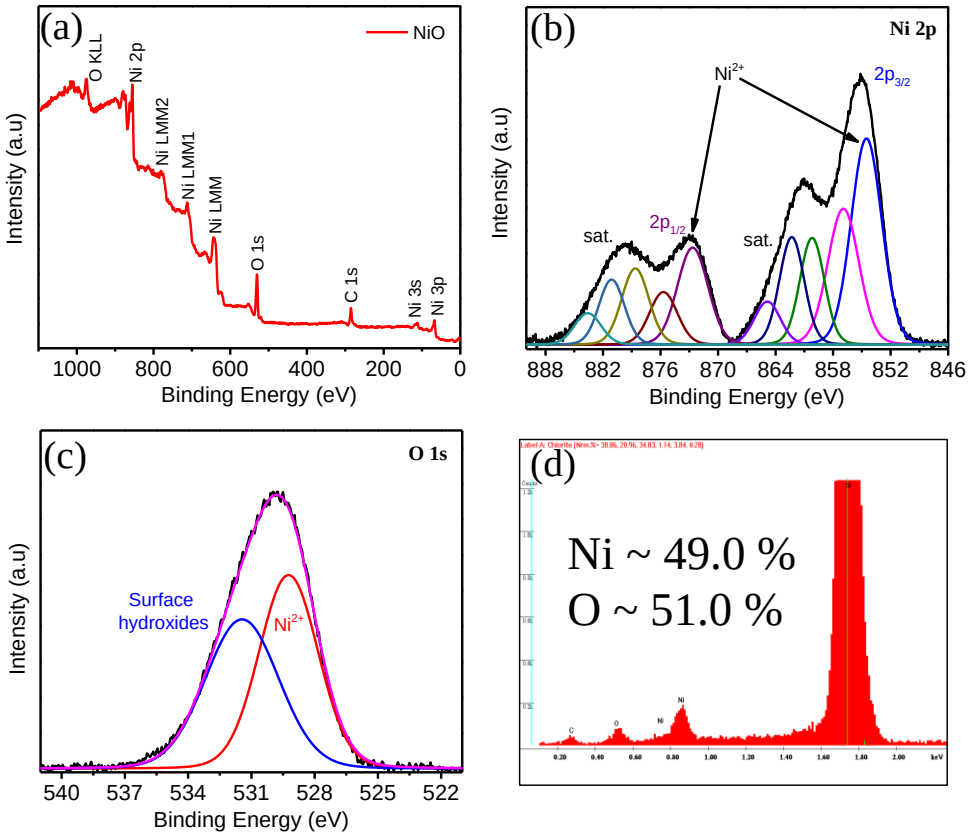

Figure 13: XP spectroscopy based results showing (a) long range survey scan, high resolution core level XP spectrum of (b) Ni 2p (c) O1s, (d) EDX spectrum, of epitaxial NiO film deposited at 250 ^{O}C by 1000 PEALD cycles on c-sapphire.

multiplet splitting, peak asymmetries, final state effects, overlapping binding energies, and shake up or satellite process.[33–36] However, we have investigated the core level Ni 2p spectra carefully. **Figure 13(b)** show the multiplet splitting of core level XP spectra of Ni 2p into Ni $2p_{3/2}$ and Ni $2p_{1/2}$ along with their shake up satellite (sat.) peaks. The Ni $2p_{3/2}$ and Ni $2p_{1/2}$ were further fitted with suitable peaks to match the experimental spectra. The deconvoluted Ni $2p_{3/2}$ spectrum shows the main peak at 854.4 eV corresponds to Ni^{2+} oxidation state of nickel atoms in NiO, a shoulder peak at 856.7 eV, and the satellite peaks from ~860.2 – 864.8 eV.[33,37] The peak shouldered at 856.7 eV arises due to the contribution from the surface hydroxylation.[34,36] Consequently, deconvoluted core level XP spectrum of Ni $2p^{1/2}$ signal at 872.6 eV due to Ni^{2+} along

with a shoulder at 875.7 eV, and the satellite peaks at 878.6 – 883.6 eV. **Figure 13(c)** shows the core level XP spectrum of O (1s) which could be deconvoluted into two peaks. The peak at 529.25 eV corresponds to the binding energy of Ni^{2+}-O-Ni^{2+} bonds. While the peak at 531.45 eV can be attributed to surface adsorbed oxygen, surface hydroxyl groups or defective sites in nickel oxide.[6] The existence of hydroxyl groups have high probability because of combustion like process during plasma or could be resulted from the prolonged exposure of ambient environment.[26,37] We could not observe the presence of metallic nickel in our NiO films as mentioned in the literature but there might be a possibility of Ni^{3+} bonds caused by surface hydroxyl groups (NiOOH).[38,39] The elemental ratio of Ni/O calculated from the XP spectrum is Ni (0.48)/O (0.52) which can be considered to be close to stoichiometric NiO. The EDX spectroscopy also shows the film to be nearly stoichiometric (see **Figure 13(d)**).

The optical bandgap of NiO film grown at 250 ^{O}C by 1000 PEALD cycles on c-sapphire was determined by acquiring the percentage transmission (%T) spectrum as a function of photon energy (hν). The optical absorption coefficient (α) for thin film was calculated using the below mentioned equation:

$$\alpha = \frac{log(100/T)}{d} \qquad (1)$$

Where 'T' is the transmittance and 'd' is the film thickness. The optical bandgap (E_g) could be calculated by direct inter-band transition proposed by J.Tauc in following equation:[40]

$$(\alpha h\nu)^2 = (h\nu - E_g) \qquad (2)$$

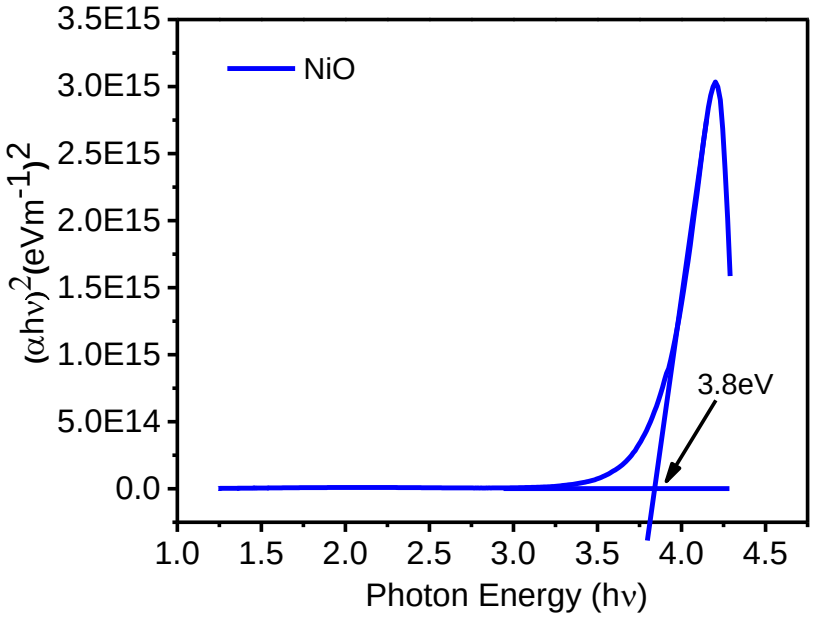

Figure 14: Tauc plot showing the optical bandgap of epitaxial NiO film deposited at 250 ^{O}C by 1000 PEALD cycles on c-sapphire.

Figure 14 shows the plot of $(\alpha h\nu)^2$ versus hν and the value of E_g was determined from the photon energy intercept by extrapolating a straight line to α = 0 value of the plot. NiO films show the direct bandgap of 3.8 eV which is consistent with the literature reports.[41] The sharp absorption tail/edge can be inferred as highly crystalline nature of NiO thin films in contrast to the weak absorption tail in amorphous materials.[42]

5. Conclusions

In conclusion, crystalline epitaxial thin films of NiO have been deposited on c-plane sapphire using sequential exposures of $[Ni(acac)_2]$ as nickel precursor and O_2 plasma as oxygen source by plasma enhanced atomic layer deposition technique. The NiO thin films show fairly slow growth rate of 0.51 Å/cycle at 250 ^{O}C. X-Ray diffraction pattern shows the growth of highly crystalline cubic rock salt type NiO thin films with epitaxial relationship of <111> NiO // <0001> Al_2O_3 with the substrate. FESEM and AFM studies confirm the evolution of small grains to form big grains with columnar morphology with reduced surface defects and roughness as the deposition temperature increases. XPS and other spectroscopic techniques show the material to be nearly stoichiometric and crystalline. The success in growing crystalline epitaxial thin films of NiO on c-sapphire by PEALD by using the nickel acetylacetonate precursor suggests that the methodology employed here may be useful to generate ultrathin films of other transition metal oxides.

6. References

(1) George, S. M. Atomic Layer Deposition: An Overview. *Chem. Rev.* **2010**, *110* (1), 111–131.

(2) Miikkulainen, V.; Leskelä, M.; Ritala, M.; Puurunen, R. L. Crystallinity of Inorganic Films Grown by Atomic Layer Deposition: Overview and General Trends. *J. Appl. Phys.* **2013**, *113* (2), 021301.

(3) Cremers, V.; Puurunen, R. L.; Dendooven, J. Conformality in Atomic Layer Deposition: Current Status Overview of Analysis and Modelling. *Appl. Phys. Rev.* **2019**, *6* (2), 021302.

(4) Marichy, C.; Bechelany, M.; Pinna, N. Atomic Layer Deposition of Nanostructured Materials for Energy and Environmental Applications. *Adv. Mater.* **2012**, *24* (8), 1017–1032.

(5) Kim, H.; Oh, I.-K. Review of Plasma-Enhanced Atomic Layer Deposition: Technical Enabler of Nanoscale Device Fabrication. *Jpn. J. Appl. Phys.* **2014**, *53* (3S2), 03DA01.

(6) Hufnagel, A. G.; Henß, A.-K.; Hoffmann, R.; Zeman, O. E. O.; Häringer, S.; Fattakhova-Rohlfing, D.; Bein, T. Electron-Blocking and Oxygen Evolution Catalyst Layers by Plasma-Enhanced Atomic Layer Deposition of Nickel Oxide. *Adv. Mater. Interfaces* **2018**, *5* (16), 1701531.

(7) Nam, W. J.; Gray, Z.; Stayancho, J.; Plotnikov, V.; Kwon, D.; Waggoner, S.; Shenai-Khatkhate, D. V.; Pickering, M.; Okano, T.; Compaan, A.; Fonash, Stephen J. ALD NiO Thin Films as a Hole Transport-Electron Blocking Layer Material for Photo-Detector and Solar Cell Devices. *ECS Trans.* **2015**, *66* (1), 275–279.

(8) Wang, H.; Wang, Y.; Wang, X. Pulsed Laser Deposition of the Porous Nickel Oxide Thin Film at Room Temperature for High-Rate Pseudocapacitive Energy Storage. *Electrochem. commun.* **2012**, *18* (1), 92–95.

(9) You, Y. H.; So, B. S.; Hwang, J. H.; Cho, W.; Lee, S. S.; Chung, T. M.; Kim, C. G.; An, K. S. Impedance Spectroscopy Characterization of Resistance Switching NiO Thin Films Prepared through Atomic Layer Deposition. *Appl. Phys. Lett.* **2006**, *89* (22), 2004–2007.

(10) Koushik, D.; Jošt, M.; Dučinskas, A.; Burgess, C.; Zardetto, V.; Weijtens, C.; Verheijen, M. A.; Kessels, W. M. M.; Albrecht, S.; Creatore, M. Plasma-Assisted Atomic Layer Deposition of Nickel Oxide as Hole Transport Layer for Hybrid Perovskite Solar Cells. *J. Mater. Chem. C* **2019**, *7* (40), 12532–12543.

(11) Newman, R.; Chrenko, R. M. Optical Properties of Nickel Oxide. *Phys. Rev.* **1959**, *114* (6), 1507–1513.

(12) Morin, F. J. Electrical Properties of NiO. *Phys. Rev.* **1954**, *93* (6), 1199–1204.

(13) Spanke, D.; Solinus, V.; Knabben, D.; Hillebrecht, F.; Ciccacci, F. Evidence for

In-Plane Antiferromagnetic Domains in Ultrathin NiO Films. *Phys. Rev. B - Condens. Matter Mater. Phys.* **1998**, *58* (9), 5201–5204.

(14) Kumagai, H.; Matsumoto, M.; Toyoda, K.; Obara, M. Preparation and Characteristics of Nickel Oxide Thin Film by Controlled Growth with Sequential Surface Chemical Reactions. *J. Mater. Sci. Lett.* **1996**, *15* (12), 1081–1083.

(15) Nardi, K. L.; Yang, N.; Dickens, C. F.; Strickler, A. L.; Bent, S. F. Creating Highly Active Atomic Layer Deposited NiO Electrocatalysts for the Oxygen Evolution Reaction. *Adv. Energy Mater.* **2015**, *5* (17), 1500412.

(16) Lu, H. L.; Scarel, G.; Wiemer, C.; Perego, M.; Spiga, S.; Fanciulli, M.; Pavia, G. Atomic Layer Deposition of NiO Films on Si(100) Using Cyclopentadienyl-Type Compounds and Ozone as Precursors. *J. Electrochem. Soc.* **2008**, *155* (10), H807-H811.

(17) Bachmann, J.; Zolotaryov, A.; Albrecht, O.; Goetze, S.; Berger, A.; Hesse, D.; Novikov, D.; Nielsch, K. Stoichiometry of Nickel Oxide Films Prepared by ALD. *Chem. Vap. Depos.* **2011**, *17* (7–9), 177–180.

(18) Yang, T. S.; Cho, W.; Kim, M.; An, K.S.; Chung, T.-M.; Kim, C. G.; Kim, Y. Atomic Layer Deposition of Nickel Oxide Films Using $Ni(dmamp)_2$ and Water. *J. Vac. Sci. Technol. A Vacuum, Surfaces, Film.* **2005**, *23* (4), 1238–1243.

(19) Antony Premkumar, P.; Toeller, M.; Adelmann, C.; Meersschaut, J.; Franquet, A.; Richard, O.; Tielens, H.; Brijs, B.; Moussa, A.; Conard, T.; et al. NiO Thin Films Synthesized by Atomic Layer Deposition Using $Ni(dmamb)_2$ and Ozone as Precursors. *Chem. Vap. Depos.* **2012**, *18* (1–3), 61–69.

(20) Song, S. J.; Lee, S. W.; Kim, G. H.; Seok, J. Y.; Yoon, K. J.; Yoon, J. H.; Hwang, C. S.; Gatineau, J.; Ko, C. Substrate Dependent Growth Behaviors of Plasma-Enhanced Atomic Layer Deposited Nickel Oxide Films for Resistive Switching Application. *Chem. Mater.* **2012**, *24* (24), 4675–4685.

(21) Kum, H.; Lee, D.; Kong, W.; Kim, H.; Park, Y.; Kim, Y.; Baek, Y.; Bae, S.-H.; Lee, K.; Kim, J. Epitaxial Growth and Layer-Transfer Techniques for Heterogeneous Integration of Materials for Electronic and Photonic Devices. *Nat. Electron.* **2019**, *2* (10), 439–450.

(22) Leskelä, M.; Ritala, M. Atomic Layer Deposition (ALD): From Precursors to Thin Film Structures. *Thin Solid Films* **2002**, *409* (1), 138–146.

(23) Holden, K. E. K.; Dezelah, C. L.; Conley, J. F. Atomic Layer Deposition of Transparent P-Type Semiconducting Nickel Oxide Using $Ni(tBu_2DAD)_2$ and Ozone. *ACS Appl. Mater. Interfaces* **2019**, *11* (33), 30437–30445.

(24) Zhang, Y.; Du, L.; Liu, X.; Ding, Y. A High Growth Rate Atomic Layer Deposition Process for Nickel Oxide Film Preparation Using a Combination of Nickel(II) Diketonate–Diamine and Ozone. *Appl. Surf. Sci.* **2019**, *481* (July), 138–143.

(25) Lindahl, E.; Ottosson, M.; Carlsson, J. O. Atomic Layer Deposition of NiO by the $Ni(thd)_2/H_2O$ Precursor Combination. *Chem. Vap. Depos.* **2009**, *15* (7–9), 186–191.

(26) Heil, S. B. S.; van Hemmen, J. L.; van de Sanden, M. C. M.; Kessels, W. M. M. Reaction Mechanisms during Plasma-Assisted Atomic Layer Deposition of Metal Oxides: A Case Study for Al_2O_3. *J. Appl. Phys.* **2008**, *103* (10), 103302.

(27) Kang, J.-K.; Rhee, S.-W. Chemical Vapor Deposition of Nickel Oxide Films from $Ni(C_5H_5)_2/O_2$. *Thin Solid Films* **2001**, *391* (1), 57–61.

(28) Ehrentraut, D.; Meissner, E.; Bockowski, M. *Technology of Gallium Nitride Crystal Growth*; Springer Series in Materials Science; Springer Berlin, Heidelberg, 2010; Vol. 133.

(29) Moram, M. A.; Vickers, M. E. X-Ray Diffraction of III-Nitrides. *Reports Prog. Phys.* **2009**, *72* (3), 036502.

(30) Gowthami, V.; Perumal, P.; Sivakumar, R.; Sanjeeviraja, C. Structural and Optical Studies on Nickel Oxide Thin Film Prepared by Nebulizer Spray Technique. *Phys. B Condens. Matter* **2014**, *452*, 1–6.

(31) Cordobo-Torresi, S. I.; Goff, A. H. Le; Joiret, S. Electrochromic Behavior of Nickel Oxide Electrodes II. Identification of the Bleached State by Raman Spectroscopy and Nuclear Reactions. *J. Electrochem. Soc.* **1991**, *138* (6), 1554–1559.

(32) Mironova-Ulmane, N.; Kuzmin, A.; Steins, I.; Grabis, J.; Sildos, I.; Pärs, M. Raman Scattering in Nanosized Nickel Oxide NiO. *J. Phys. Conf. Ser.* **2007**, *93* (1), 012039.

(33) Seo, S.; Park, I. J.; Kim, M.; Lee, S.; Bae, C.; Jung, H. S.; Park, N. G.; Kim, J. Y.; Shin, H. An Ultra-Thin, Un-Doped NiO Hole Transporting Layer of Highly Efficient (16.4%) Organic-Inorganic Hybrid Perovskite Solar Cells. *Nanoscale* **2016**, *8* (22), 11403–11412.

(34) Soriano, L.; Preda, I.; Gutiérrez, A.; Palacín, S.; Abbate, M.; Vollmer, A. Surface Effects in the Ni 2p X-Ray Photoemission Spectra of NiO. *Phys. Rev. B - Condens. Matter Mater. Phys.* **2007**, *75* (23), 1–4.

(35) Grosvenor, A. P.; Biesinger, M. C.; Smart, R. S. C.; McIntyre, N. S. New Interpretations of XPS Spectra of Nickel Metal and Oxides. *Surf. Sci.* **2006**, *600* (9), 1771–1779.

(36) Mossanek, R. J. O.; Preda, I.; Abbate, M.; Rubio-Zuazo, J.; Castro, G. R.; Vollmer, A.; Gutiérrez, A.; Soriano, L. Investigation of Surface and Non-Local Screening Effects in the Ni 2p Core Level Photoemission Spectra of NiO. *Chem. Phys. Lett.* **2011**, *501* (4–6), 437–441.

(37) Peck, M. A.; Langell, M. A. Comparison of Nanoscaled and Bulk NiO Structural and Environmental Characteristics by XRD, XAFS, and XPS. *Chem. Mater.* **2012**, *24* (23), 4483–4490.

(38) Hsu, C.C.; Su, H.W.; Hou, C.H.; Shyue, J.J.; Tsai, F.Y. Atomic Layer Deposition of NiO Hole-Transporting Layers for Polymer Solar Cells. *Nanotechnology* **2015**, *26* (38), 385201.

(39) Ratcliff, E. L.; Meyer, J.; Steirer, K. X.; Garcia, A.; Berry, J. J.; Ginley, D. S.;

Olson, D. C.; Kahn, A.; Armstrong, N. R. Evidence for Near-Surface NiOOH Species in Solution-Processed NiO_x Selective Interlayer Materials: Impact on Energetics and the Performance of Polymer Bulk Heterojunction Photovoltaics. *Chem. Mater.* **2011**, *23* (22), 4988–5000.

(40) Tauc, J.; Grigorovici, R.; Vancu, A. Optical Properties and Electronic Structure of Amorphous Germanium. *Phys. status solidi* **1966**, *15* (2), 627–637.

(41) Lu, H. L.; Scarel, G.; Alia, M.; Fanciulli, M.; Ding, S. J.; Zhang, D. W. Spectroscopic Ellipsometry Study of Thin NiO Films Grown on Si (100) by Atomic Layer Deposition. *Appl. Phys. Lett.* **2008**, *92* (22), 2006–2009.

(42) Wood, D. L.; Tauc, J. Weak Absorption Tails in Amorphous Semiconductors. *Phys. Rev. B* **1972**, *5* (8), 3144–3151.

Summary of the Thesis

With the increasing demand of ultrathin films of materials for compact nanoscale devices, there is need to explore the fundamental properties of materials at atomic scale thickness. Materials when reduced in one spatial dimension, typically 1 – 100 nm, exhibit unique properties compared to their bulk counterparts because of quantum confinement and other factors. Ultrathin films of layered and non- layered materials possess properties which could be of use in opto- /nanoelectronics, thermal management and energy devices related applications. This thesis deals entirely with the deposition (or synthesis), characterization of thin films (nanosheets) of layered $(BN)_{1-x}(C)_x$ and of a non-layered metal oxide, nickel oxide. Solid state synthesis, pulsed laser deposition and atomic layer deposition techniques have been employed and certain important properties of these materials examined.

Graphene and h-BN are the two most well known two-dimensional layered materials. Graphene is a gapless material while h-BN is a large bandgap (~ 6eV) material. There have been efforts to tune their electronic properties, but the bandgap could only be changed by a few meV. Borocarbonitrides, $B_xC_yN_z$ (BCN for short), with a similar honeycomb lattice, constitute a new class of 2D layered materials containing both graphene and BN domains along with the BCN rings in the network. BCN materials possess unique electrical and physical properties which are distinct from graphene and h-BN. These materials are of particular interest because they allow one to tune the electronic properties from those of gapless graphene to those of high bandgap h-BN.

Thin films of borocarbonitrides, $(BN)_{1-x}(C)_x$, of various compositions have been deposited by pulsed laser deposition (PLD). $(BN)_{1-x}(C)_x$ films deposited from varied target compositions have been characterized by spectroscopic (Raman spectroscopy, XPS) and microscopic (FESEM, AFM, TEM) techniques. It has been possible to vary the composition to obtain different bandgaps. BCN films deposited on insulating transparent substrates allow us to probe their optical and electrical properties, which change systematically with the composition. The optical band gap of these films shows a nearly linear relationship with the composition in the range of 0 to 6 eV. Even though there are a few literature reports on BCN films, the tuning of electronic structure from graphene to BN has been achieved for the first time. BCN films show semiconducting

properties, and the electrical resistivity of the films varies with the composition, following the ES-VRH behaviour in the low temperature regime.

Few-layer BCN nanosheets of different compositions have been synthesized by solid state reaction employing urea, boric acid and activated charcoal. The synthesized BCN have been characterized by Raman spectroscopy, X-ray photoelectron spectroscopy, transmission electron microscopy and others. Although there have been theoretical studies, experimental studies of the thermal transport and thermoelectric properties of BCN materials have not yet been explored. Temperature variation of electrical conductivity and the Seebeck coefficient confirms *p*-type semiconducting thermoelectric transport properties in 300-573 K range. More interestingly, the BCN exhibit low thermal conductivity (0.58 to 1.86 W/mK) unlike hexagonal boron nitride and graphene over the temperature range of 300-573 K. The low thermal conductivity of BCN materials arises due to significant phonon scattering by the different length scale hierarchical nano/meso architectures such as bonding heterogeneity (e.g. C–B, C–N and B–N), point defects related C/B/N disorder, nanodomains of BN/carbon and grain boundaries. The low thermal conductivity of BCN materials could be of value in thermal energy management.

With the increasing demand for atomic level thickness control and conformal films, atomic layer deposition (ALD) turns out to be the most effective technique for the purpose. ALD processes have been developed for a wide variety of materials, and the growth of pristine single phase materials with preferred orientation with the underlying substrate has practical utility. Most of ALD deposited materials are however polycrystalline or amorphous. In this work, crystalline epitaxial thin films of NiO have been deposited on c-sapphire by PEALD and characterized by X-Ray diffraction as well as various microscopic and spectroscopic techniques. Interestingly, the deposited NiO thin films show epitaxial growth of (111) plane along the (0006) plane of c-sapphire at all growth temperatures (200 – 260 ^{O}C). The FESEM and AFM based microscopic study confirms the evolution of small grains to form big grains with columnar morphology with reduced surface defects and roughness of NiO films as the deposition temperature increases. Spectroscopic analysis confirms the films to nearly stoichiometric with a 3.8 eV bandgap with the presence hydroxyl groups at the surface.

The authors hope that the results presented in this thesis will make significant contribution for the understanding of materials at the nanoscale.

****